1-1-2014

Non-Linear Robust Observers For Systems With Non-Collocated Sensors And Actuators

Constantine Mastory
Wayne State University,

Recommended Citation

Mastory, Constantine, "Non-Linear Robust Observers For Systems With Non-Collocated Sensors And Actuators" (2014). *Wayne State University Dissertations.* Paper 991.

NON-LINEAR ROBUST OBSERVERS FOR SYSTEMS WITH NON-COLLOCATED SENSORS AND ACTUATORS

by

CONSTANTINE GEORGES MASTORY

DISSERTATION

Submitted to the Graduate School

of Wayne State University,

Detroit, Michigan

in partial fulfillment of the requirements

for the degree of

DOCTOR OF PHILOSOPHY

2014

MAJOR: MECHANICAL ENGINEERING

Approved by:

Advisor Date

DEDICATION

At the end of this long trip, I would like to dedicate this work first and foremost to the greatest parents any person could wish for and to the love of my life and my copilot along this ride.

ACKNOWLEDGMENTS

I would like to thank my amazing parents and my sister, Georges, Claire and Helena Mastory, for every effort they did whether it be a prayer or long working hours to get me to where I am, the way I am. Thank you for your support and love, without them, I would not have made it through. Alloun, your craziness has always been an inspiration!

Another endless thanks is due to the one that kept me standing on my feet when everything was going against me. Thank you Stephanie, life just started!

To my greatest mentor and father away from home, Prof. Nabil Chalhoub, you taught me the fine art of being a true engineer; it is truly nothing but a way of thinking. Thank you for your devotion and care. I wish you the best of luck in your new venture, Chair!

To all my friends, locally and internationally, cheers for the support.

Finally, I would like to acknowledge the partial financial support of the Office of Naval Research (ONR), award number N00014-11-1-0803, through the program director Ms. Kelly B. Cooper.

TABLE OF CONTENTS

LIST OF TABLES

LIST OF FIGURES

NOMENCLATURE

$(\ )'$	A prime superscript indicates differentiation with respect to x
$\dot{(\ )}$	A dot overscript indicates differentiation with respect to time
$(\ )_p, (\ )_f$	Subscripts “ p ” and “ f ” refer to a payload and flexible link variables, respectively
$(\ )_{,z_2}$	A “$,z_2$” subscript indicates partial differentiation with respect to z_2
$(\ )^*$	A “*” superscript refers to a mass center variable
A	Cross sectional area of the beam
A_3	Cross sectional area and flexural rigidity of the third link, respectively
E_{pe}	Young’s modulus of elasticity for the piezoelectric patch
EI	Flexural rigidity of the pinned-free and clamped-free beams
$EI_{z_2 z_2}$	Flexural rigidity of the third link of the spherical manipulator
F	Control force of the prismatic joint
$\underset{\sim}{I}, \underset{\sim}{J}, \underset{\sim}{K}$	Unit vectors corresponding to the inertial frame
I	Area moment of inertia of the beam

$I_{z_1 z_1}^{link\ 1}, I_{z_1 z_1}^{link\ 2}$	Mass moment of inertia of the first and second links around the axis that passes through $\underset{\sim}{k}_1$, respectively
I_{3_r}	Inertia tensor of the rigid portion of the third link
I_p	Inertia tensor of the payload
L	Beam length
L_{pe}	Piezoelectric patch length
L_i	Length of the i^{th} link of the spherical manipulator
$T(x=0,t)$	Pinned-free beam control torque applied at its pinned end
T_1	Control torque of the first link of the spherical manipulator
$T_{\{j\}}^{\{i\}}$	A 4×4 D-H transformation matrix representing the location and orientation of the i^{th} frame with respect to the j^{th} frame
(X, Y)	Current location of the boat
(X_i, Y_i)	Location of the i^{th} waypoint
c_i	Damping coefficient for the i^{th} elastic mode
d_{31}	Piezoelectric patch strain constant
h	Thickness of the beam

h_{pe}	Thickness of the piezoelectric patch
g	Gravitational acceleration
m	Mass of the beam
m_p	Payload mass
q_{PF_i}, q_{CF_i}	Time-dependent generalized coordinates corresponding to the i^{th} elastic modes of the pinned-free and clamped-free beams, respectively
q_i	Time-dependent generalized coordinates corresponding to the i^{th} elastic modes of the flexible portion of link three
$q_{i_e}(t)$	Estimated value of $q_i(t)$
$q_{i_m}(t)$	Value of $q_i(t)$ computed from measured strain gauge signals
r	Translational displacement of the third link of the spherical robotic arm
r_i^j	i^{th} fuzzy rule corresponding to the j^{th} state variable
u, v	Out-of-plane and in-plane transverse deformations of the flexible portion of the third link, respectively
v_c	Piezoelectric patch input voltage

w_{PF}, w_{CF}	In-plane transverse deformations of the pinned-free and clamped-free beams, respectively
w_i^j	Weight of the i^{th} fuzzy rule corresponding to the j^{th} state variable
x	Constant distance from the pinned- or clamped-end to an arbitrary point on the beam
x_{pe}	Location of the center of the piezoelectric patch from the clamped-end
$\{x_0, y_0, z_0\}$	Inertial reference frame of the spherical robotic arm
$\{x_i, y_i, z_i\}$	i^{th} body-fixed coordinate system on the spherical robotic arm
$\dot{\bar{x}}_i$	Boat’s surge speed along the $(i+1)^{th}$ path
Φ_{PF_i}, Φ_{CF_i}	Eigenfunctions of the i^{th} elastic modes of the pinned-free and clamped-free beams, respectively
$\alpha_{PF_i}, \beta_{PF_i}, \alpha_{CF_i}, \beta_{CF_i}$	Eigenfunction parameters of the i^{th} elastic modes of the pinned-free and clamped-free beams, respectively
γ_i	Fuzzy tuning parameter corresponding to the i^{th} state variable
$\eta_i, \eta_{PF}, \lambda_{PF}, g_{PF}$	Control parameters

θ_1	Angular displacement of the first link of the spherical robotic arm
ρ	Density of the beams and links
ρ_{pe}	Density of the piezoelectric patch
ϕ_{PF}	Thickness of the boundary layer surrounding the sliding surface in the structural controller of the pinned-free beam
ϕ_i	Thickness of the boundary layer surrounding the sliding surface of the i^{th} state variable
ψ	Boat’s heading angle
$\omega_{n_i}^{PF}, \omega_{n_i}^{CF}$	i^{th} elastic modes natural frequencies of the pinned-free and clamped-free beams, respectively
$\underset{\sim}{\omega}_j^{\{i\}}$	Angular velocity vector of the j^{th} link with respect to the i^{th} body-fixed coordinate system

CHAPTER 1 INTRODUCTION

Advanced control applications generally involve complex and highly nonlinear systems. The models of such systems suffer from structured and unstructured uncertainties, which make it very hard to successfully implement model-based controllers and observers. The current work addresses this issue by focusing on robust algorithms that do not necessarily require full knowledge of the system's dynamics.

In the next Section, the motivation and objectives of the current work are presented. A review of the literature, pertaining to the impact of non-collocated sensors and actuators, state observers, and the control of marine surface vessels, is included in Section 2. Finally, an overview of the dissertation is given in Section 3.

1.1 Motivation and Objectives

Challenges in controlling highly nonlinear systems are not limited to the development of sophisticated algorithms that are tolerant to modeling imprecision. There are additional challenges pertaining to the implementation of the control algorithms such as the availability of the state variables needed for the computation of the control signals, and the adverse effects of non-collocated sensors and actuators.

The current work aims at addressing these challenges by examining the detrimental effects of non-collocated sensors and actuators on the performance of structural controllers and by suggesting remedial steps that can be taken to make such controllers immune to these adverse effects. Furthermore, many novel robust observers have recently been presented in the literature as reliable schemes for providing accurate estimates of the unavailable state variables. However, most of these observers have been assessed in theoretical studies and very few have been experimentally validated. Therefore, the intention of the current study is to focus on the experimental validation of two observers, namely, a self-tuning observer and a sliding mode observer. The validation is based on the capability of these observers to accurately estimate the required state variables in the presence of significant modeling imprecision and considerable external disturbances. Moreover, the experimental work was conducted in both controlled and uncontrolled experimental settings. The challenges of the controlled setting stem from the fact that the natural frequencies of the structure are configuration-dependent. However, the uncontrolled setting involves a boat operating in open-water with external disturbances induced by waves, sea currents, and winds. Additionally, the boat’s dynamics have been totally ignored in the formulations of both observers and controllers. It should be pointed out that the experimental tests, conducted in the uncontrolled settings, have relied on the estimated rather than the measured state variables in the computation of the control signals of the boat’s robust controllers.

1.2 Literature Survey

The current work deals with the implementation of nonlinear robust controllers and observers in two different, yet equally challenging, applications such as flexible structures and marine surface vessels. The following is an overview of what has been reported in the literature regarding the impact of non-collocated sensors and actuators, state observers, and the control of marine vessels.

1.2.1 Impact of Non Collocated Sensors and Actuators

Numerous studies have considered the control problem of lightweight flexible structures (Book et al, 1975; Cannon and Schmitz, 1984; Chalhoub and Zhang, 1993; Choi et al, 1995; Chodavarapu and Spong, 1996; Chen and Chalhoub, 1997; Kim and Inman, 2001; Bazzi and Chalhoub, 2005; Song and Gu, 2007; Li and Wang, 2011; Preumont, 2011; Vakil et al, 2011; Mamani et al, 2012; Forbes and Damaren, 2012; Rahman et al, 2013; Zhang et al, 2013; Shao and Chen, 2013). The objective of the controllers has primarily been to yield a desired rigid body response of the system while actively damping out the undesired vibrations. This goal is rendered more difficult by the fact that the sensors and actuators of flexible structures are generally non-collocated. As a result, the system will have a non-minimum phase angle for certain locations of sensors and actuators whereby the phase lag of the system will surpass -180° and half of the real zeros will be located in the right half of the complex plane (Gevarter, 1970; Cannon and Rosenthal, 1984; Park and Asada, 1990a and 1990b; Spector and Flashner, 1990; Chodavarapu and Spong, 1996). Such systems will have restricted bandwidths for disturbance rejection and their feedback control designs will be severely limited (Cannon and Rosenthal, 1984;

Freudenberg and Looze, 1985; Park and Asada, 1990b; Fleming and Crawley, 1991).

Fleming and Crawley (1991) investigated the effects on the open-loop zeros of the system due to variations in the sensor and actuator locations. An infinite dimensional model was considered in order to eliminate errors induced by model truncation. For flexible structures with collocated sensors and actuators, the transfer function of the system will always have alternating poles and zeros (Cannon and Rosenthal, 1984; Fleming and Crawley 1991). That is the location of each zero is bounded on the imaginary axis by two poles. This pole-zero pattern will not change even in the presence of significant variations in system parameters. As the location of the collocated sensor-actuator pair sweeps the entire length of the beam, each zero will fluctuate between its adjacent poles and will only coincide with its respective upper bound pole at the modal node. At the intersection point, a pole-zero cancellation will occur and the system becomes simultaneously uncontrollable and unobservable due to the fact that both the sensor and the actuator are located at the modal node. On the other hand, non-collocated systems tend to lose the nice feature of alternating poles and zeros. Cannon and Rosenthal (1984) have demonstrated that non-collocated systems can exhibit the non-desirable feature of “pole-zero” flipping due to variations in the system parameters. Moreover, systems with slightly non-collocated sensors and actuators will have their zeros exceeding their upper bounds defined in the collocated sensors and actuators case, particularly, in the vicinity of the modal nodes. The violations, which are more pronounced for higher elastic modes, occur whenever the sensor and actuator are located on opposite sides of the modal node, which causes the actuator action and the measured signal to be out-of-phase for that particular elastic mode. In non-collocated systems, pole-zero cancellations are induced by the system being either uncontrollable, due to the mounting of an actuator at a modal node, or unobservable, due to the placement of a sensor at a modal node (Fleming and Crawley, 1991).

Systems with considerable non-collocation of their sensors and actuators will have some of their open-loop zeros in the right half of the complex plane, which lead them to have non-minimum phase characteristics (Gevarter, 1970; Spector and Flashner, 1990; Fleming and Crawley, 1991).

For an effective structural controller of a lightly non-collocated system, both the sensor and the actuator must be placed on the same side and away from the modal nodes of the controlled elastic modes. This will enable the system to retain its minimum phase characteristic. It should be pointed out that such placement configuration of the sensor and actuator may not be achievable for higher elastic modes whose wavelengths are comparable or shorter than the distance between the sensor and the actuator; thus, restricting the number of elastic modes that can be controlled. Such a limitation is not debilitating because many applications only requires the first few elastic modes to be controlled.

The placement of the sensors and the actuators on the same side of the modal nodes necessitates an accurate knowledge of the locations of the system's zeros. Since the dynamics of these infinite-dimensional distributed parameter structures are usually approximated by finite dimensional models then the truncation of the higher elastic modes tends to introduce errors in the predicted zeros of the system. Williams (1990) studied the effect of the model order on the transmission zeros of flexible structures with collocated sensors and actuators. His numerical analysis showed that the transmission zeros of a finite-dimensional model converge monotonically to their exact values as the model order is increased.

The design of structural controllers for systems with a considerable degree of non-collocation is very challenging. Many studies have focused on achieving minimum phase characteristics for non-collocated beams. Wang and Vidyasagar (1989) and Pota and Vidyasagar (1991) showed that the relative degree of the transfer function for a single flexible beam with non-collocated sensor and actuator is not well-defined as more elastic modes are included in the model. To alleviate the problem, an alternative output signal "the reflected tip position" was suggested to yield a well-defined relative degree of two for the transfer function of the beam. Using the reflected tip position measurement, the transfer function of the system will have the desirable property of being passive; thus, facilitating the design of the structural controller.

Another approach has been proposed by Park and Asada (1990b), which integrates the structural design of a single flexible link with the controller design in order to change the phase characteristic of the system from non-minimum to minimum phase. This was done by developing a special transmission mechanism that allows the relocation of the point of torque actuation from the base to a point near the endpoint. As a result, the zeros, located in the right half of the complex plane, are moved onto the imaginary axis; thus, yielding a minimum phase system.

The purpose of the present study is to investigate the adverse effects induced by non-collocated sensors and actuators on the performance of structural controllers. It builds on the work done by Spector and Flashner (1990) and explores remedial schemes, based on the phase angle contour of the system, to enhance the capabilities of structural controllers in order to ensure a desirable and robust performance of the closed-loop system irrespective of the sensor location with respect to the actuator.

1.2.2 State Estimators

In general, the number of state variables tends to be greater than the number of measured variables. This can be due to many factors. For instance, the required state variable may not have a physical meaning, the system set-up may be very tight on space to mount the required transducer, or the sensor may not be able to withstand the harsh operating conditions of the system. Furthermore, the use of large number of transducers entails higher overall system cost, which can be problematic in meeting budgetary concerns. It should be noted that in some situations, estimated rather than measured state variables were used either to improve the controller performance (Yanada and Shimahara,

1997) or to reduce the observation spillover effect on structural controllers (Kim and Inman, 2001).

To address the above stated constraints and the fact that modern control schemes require most if not all state variables of the system to be available for the computation of the control signals, state observers are relied on to provide accurate estimates of the required variables based on accessible information such as the input and output vectors along with a nominal model of the plant. Many types of observers have been reported in the literature and only a representative set of these state estimators will be discussed herein.

The Luenberger observer is a state estimator suitable for linear time-invariant systems whose dynamics are fully known. By defining the error vector to be the difference between the outputs of the plant and the observer, the error vector equation can be written as a linear time-invariant homogeneous first order ordinary differential equation. Based on the pole placement technique, the error vector can be exponentially driven to zero (Luenberger, 1964, 1966 & 1979; Chen, 1970; Kailath, 1980; Friedland, 1986; Ogata, 2002; Lin, 2007). The main setback of such observers is their reliance on exact knowledge of the plant's dynamics.

In order to reduce the computational requirement of the full-order Luenberger observer, reduced-order state estimators have been proposed to solely estimate the unmeasured state variables. In other words, reduced order observers provide estimates for only the state variables that are not accessible through the system's output vector (Chen, 1970; Kailath, 1980; Friedland, 1986; Ogata, 2002; Lin, 2007). It is important to note that even though reduced order observers do not introduce estimation errors in the measured states variables, the noise, inherent in these measured signals, will be amplified by the controller gains; thus, negatively impacting the response of the closed-loop system.

Some researchers tried extending the application of these linear observers to linear time-variant or nonlinear systems (Baumann and Rugh, 1986). Yanada and Shimahara (1997) applied the gain scheduling scheme to enable Luenberger observers to cope with variations in the plant parameters. However, the performance of these linear observers have been shown to strongly rely on the exact knowledge of the system's dynamics and found to be susceptible to external disturbances. The same can be said about Kalman filters, despite the fact that they were designed to estimate the state variables for stochastic linear systems with noise contamination (Sorenson, 1985; Lewis, 1986; Anderson and Moore, 1990; Sorensen et al., 1996; Sandler et al. 1996; Jwo and Cho, 2007).

A comparative study, between the performances of a Luenberger observer and an adaptive state observer (ASO) has been performed by Nandam and Sen (1990). As expected, the performance of the ASO was superior to that of the Luenberger observer and produced good estimates in spite of variations in the system parameters. However, the ASO is a computationally intensive scheme that estimates both the state variables and the system parameters (Rajamani and Hedrick, 1993; Cho, Rajamani, 1997). Other researchers have introduced the “output rejection” term as an attempt to cancel nonlinearities that are dependent on the measured system’s output (Krener and Isidori, 1983; Besancon, 1999).

Nonlinear asymptotic and exponential observers have been developed for nonlinear systems satisfying the Lipschitz conditions (Thau, 1973; Kou et al, 1975; Banks, 1981; Xia and Gao, 1988; Tsinias, 1989; Yaz, 1993; Boyd et al., 1994; Raghavan and Hedrick, 1994; Sundarapandian, 2002). The drawback of these estimators stems from the fact that they require exact knowledge of the plant, which renders them susceptible to both parametric uncertainties and external disturbances.

To alleviate this problem, observers based on the variable structure systems (VSS) theory have been designed for nonlinear systems with bounded nonlinearities and uncertainties (Utkin, 1981; Drakunov, 1983; Walcott and Zak, 1986; Slotine et al, 1987; Wagner and Shoureshi, 1988; Misawa and Hedrick, 1989; Canudas De Wit and Slotine, 1991; Drakunov and Utkin, 1995; Rundell et al, 1996; Ahmed-Ali and Lamnabhi-Lagarrigue, 1999; Jiang and Wu, 2002; Kfoury et al, 2006; Mastory and Chalhoub, 2014). These state estimators, which are designed based on the sliding mode methodology, have yielded robust performances in the presence of structured and unstructured uncertainties as long as the upper bounds on modeling imprecision and external disturbances are known. Kfoury and Chalhoub (2011) extended the capability of sliding mode observers to constrained systems that are represented by nonlinear differentialalgebraic (D-A) equations. They introduced three different types of robust observers for constrained systems. The accuracy with which the state variables can be estimated depends on how well the constrained equations are approximated.

The sliding mode observers have been implemented to estimate the joint angular velocities of a robot arm (Canudas De Wit and Slotine, 1991), the cylinder gas pressure for a single-cylinder Diesel engine (Kao and Moskwa, 1995), and the flux in an induction motor (Benchaib and Rachid, 1999).

Chalhoub and Kfoury (2005) proposed a novel sliding mode observer design that reduces the required number of measured outputs, hence optimizing the use of sensors. The digital simulation results have demonstrated the capability of the observer in accurately estimating all the system’s state variables. The drawback of this approach stems from the need for a benchmark state vector based on which the observer can be tuned, which makes its robustness to be system specific.

Khaled and Chalhoub (2014) developed a self-tuning fuzzy sliding mode observer in an effort to combine the advantages of the sliding mode methodology with those of the self-tuning fuzzy logic algorithm. Such a nonlinear observer does not require a precise knowledge of the plant dynamics or the intensive tuning of a rule-based expert fuzzy inference system (FIS). It only requires that the upper bounds on modeling imprecision and external disturbances to be known. The convergence of the tuning process is guaranteed by forcing the tuning parameters to satisfy inequality conditions brought about by imposing the time derivatives of Lyapunov functions to be negative definite.

Both the self-tuning fuzzy sliding mode observer and the sliding mode observer have been applied and experimentally validated in this study. They were used to estimate the state variables of two challenging physical systems. The first one is placed in a fully controlled environment and consists of a flexible spherical robotic manipulator with configuration-dependent natural frequencies. While the second system represents a sixteen feet boat with unknown dynamics operating in the fully uncontrolled environment of the open-water. The main goal of this work is to provide experimental validation for the robust performances and accurate estimation capabilities of the self-tuning and sliding mode observers.

1.2.3 Control of Marine Surface Vessels

In this phase of the present study, the experimental set-up consists of an under-actuated marine surface vessel that relies on the propeller thrust and orientation to control the surge speed, the sway motion, and the vessel's heading. Therefore, only two control signals are available for controlling three degrees of freedom of the vessel. Traditionally, this problem is handled by coupling the guidance system with the controller. Such an integrated system allows the steering variable to simultaneously control the sway and heading of the ship while dedicating the propeller thrust for the control of the surge speed (Healey and Marco, 1992; Jiang and Nijmeijer, 1999; Pettersen and Lefeber, 2001; Jiang, 2002; Fossen, 2002; Fossen et al., 2003; Do et al., 2003 and 2005;

Lefeber et al., 2003; Brevik, 2003; Moreira et al., 2007; Khaled and Chalhoub, 2010).

In the present work, the desired heading angle is determined by a guidance scheme that was developed based on the variable radius line-of-sight (LOS) and acceptance circles around the waypoints (Healey and Marco, 1992; Fossen, 2002; Breivik, 2003; Moreira et al, 2007). Furthermore, the surge speed profile along the desired trajectory is specified by a path planning algorithm. Once the desired heading angle and surge speed profile are automatically specified by the guidance system, the controller has to ensure that the actual heading angle and surge speed adhere to these values with minimum tracking errors.

In general, a ship may undergo a heading, a dynamic positioning, or a trajectory tracking maneuver. For the heading task, the steering mechanism, be it a rudder or a revolving propeller, is controlled to yield the desired ship orientation (Minorsky, 1922; Kallstrom et al., 1979; Van Amerongen, 1984; Lopez and Rubio, 1992; Vahedipour and Bobis, 1992; Vukic and Milinovic, 1996; Fossen, 1999; Moreira et al., 2007; Francisco et al., 2008; Minghui, 2008). Early attempts to automate ship steering involved the use of proportional-integral-derivative (PID) controllers due to their ease of design and implementation. Originally conducted by Minorsky (1922) as a project for the US Navy, crews were observed as they maneuvered their ships. Their actions and reactions were incorporated into the tuning benchmark for the PID controllers. This strategy has been widely used for ship heading control and proven to be successful under mild environmental conditions (Kallstrom et al., 1979; Vahedipour and Bobis, 1992; Vukic and Milinovic, 1996; Fossen, 1999; Moreira et al., 2007; Francisco et al., 2008; Minghui, 2008). However, these controllers failed to yield satisfactory performances under severe sea states where the effects of external environmental disturbances and system's inherent nonlinearities become significant (Kallstrom et al, 1979). Many studies have since attempted to improve the robustness of PID controllers but none were able to render them insensitive to modeling imprecision. For instance, linear controllers with a gain scheduling scheme have been implemented based on the ship's speed (Kallstrom et al., 1979). Moreover, model-based steering adaptive controller (Van Amerongen and Udink Ten Cate, 1975; Van Amerongen, 1984), linear quadratic regulator (LQR), and linear quadratic tracking (LQT) controllers have also been implemented to automatically steer the ship (Lopez and Rubio, 1992). However, the use of linear controllers has been proven to be limited in practical applications whereby the plant dynamics are not fully known and the operating conditions are unpredictable and constantly changing. This necessitates the use of nonlinear controllers that are robust to structured and unstructured uncertainties along with external disturbances.

In a dynamic positioning (DP) maneuver, the ship position and heading are maintained at set values by employing a control system that relies on propellers and thrusters for its control actions (Pettersen and Fossen, 2000; Loria et al., 2000; Torsetnes et al., 2004). Such a task is usually needed whenever anchoring at deep water is not possible and a specific ship orientation is desired to lessen the effects of wind, waves, and sea currents.

A trajectory tracking task requires the ship to follow a prescribed path, defined by a set of waypoints, while maintaining a desired surge speed profile along the desired trajectory (Balchen et al., 1980; Sorensen et al., 1996; Aamo and Fossen, 1999; Lindegaard, 2003; Breivik et al., 2006; Khaled and Chalhoub, 2011; Khaled and Chalhoub, 2013; Chalhoub and Khaled, 2014). As stated earlier, the tracking task by a fully autonomous and under-actuated marine surface vessel requires the integration of a guidance system with the control algorithm. The controller design is not a trivial task given the unpredictable and constantly varying operating conditions in open seas and oceans, the inherent nonlinearities of the ship, and the significant structured and unstructured uncertainties associated with the modeling imprecision of the marine vessel (Pettersen and Nijmeijer, 2001; Morel, 2009). Structured uncertainties refer to inaccuracies in the plant parameters; while unstructured uncertainties pertain to neglected higher order dynamics of the system. This problem can be compounded by severely cold weather conditions, which can induce ice accretion along the ship hull and result in significant weight shift on the vessel; thus, drastically affecting the ship performance (Derrett and Barrass, 1999; Laranjinha et al., 2002; International Maritime Organization, 2007; Falzarano and Lakhotia, 2008). Moreover, the tracking controller is often designed based on a reduced-order model of the ship that usually accounts for the surge, sway, and yaw degrees of freedom while ignoring those pertaining to roll, pitch, and heave motions; thus, exacerbating the modeling imprecision problem.

During a single trip, a marine vessel can be subjected to various sea states ranging from mild to extreme ones. Thus, the controller of the vessel should have a good disturbance rejection characteristic while being insensitive to significant modeling imprecision (Godhavn et al.,1998; Lauvdal and Fossen, 1998; Fossen and Strand, 1999a; Pettersen and Nijmeijer, 2001; Do et al, 2003; Yang et al, 2003; Cimen and Banks, 2004; Yang and Jiang, 2004; Li et al, 2009).

Many model-based controllers have been devised for marine applications (Fossen, 1993; Godhavn, 1996; Berge et al., 1998; Fossen and Grovlen, 1998; Strand et al., 1998; Fossen and Strand, 1999a; Fossen, 2000; Pettersen and Nijmeijer, 2001; Moreira et al., 2007; Pivano et al., 2007). Given the complexity and the considerable modeling imprecision of marine vessels along with the constantly varying operating conditions, one would expect the performance of these controllers to deteriorate as the modeling and environmental uncertainties become significant. Therefore only controllers, exhibiting strong robustness characteristics to modeling imprecision and external disturbances or capable of adapting to varying environmental conditions, have been considered in the current work (Godhavn et al., 1998; Lauvdal and Fossen, 1998; Fossen and Strand, 1999a and 1999b; Pettersen and Nijmeijer, 2001; Aranda et al., 2002; Do et al., 2003; Yang et al., 2003; Cimen and Banks, 2004; Li et al., 2009).

To deal with system’s nonlinearities, nonlinear controllers, based on the state feedback linearization scheme (Fossen, 1993; Berge et al, 1998; Fossen, 2000; Moreira et al, 2007), the output feedback compensation and the back-stepping algorithm (Fossen and Grovlen, 1998; Strand et al, 1998; Godhavn et al, 1998; Fossen and Strand, 1999; Pettersen and Nijmeijer, 2001) have been implemented in maritime applications. However, the reliance of these controllers on exact knowledge of the plant’s dynamics has made them susceptible to both structured and unstructured uncertainties (Pivano et al, 2007). Thus, these model-based controllers are not suitable for the trajectory tracking problem of marine surface vessel.

Fuzzy logic controllers present a very attractive and plausible approach for dealing with the unknown dynamics of marine vessels (Sugeno, 1985; Maeda and Murakami, 1992; Layne and Passino, 1993; Yeh, 1994; Polkinghorne et al, 1995; Zadeh, 1997; Choi and Kim, 1997; Ha et al., 1999; Yansheng and Jiang, 2004; Minghui et al, 2008). However, the tuning process of an expert knowledge, fixed rule-based fuzzy inference system is very time consuming. In addition, the sole reliance of these controllers on human experience does not allow them to exploit useful information that can be obtained from physics-based models. In an attempt to reduce the required time for tuning such controllers, self-organized fuzzy logic controllers have been devised with a built-in tuning technique to adapt the controller gains to varying operating conditions of the plant (Procyk and Mamdani, 1979; Chih-Hsun and Hung-Ching, 1994; Tönshoff and Walter, 1994;

Jie et al., 2007; Yu, 2009; Chaoui and Sicard, 2012). Such fuzzy controllers have been applied in track-keeping (Velagic et al, 2003) and heading control (Sutton and Towill, 1987; Sutton and Jess, 1991) of marine vessels. The drawbacks of these controllers stems from the fact that they have been presented without a proof of stability for the closed-loop system.

A class of nonlinear controllers, based on the variable structure systems theory, has been introduced in the literature and proven to offer robustness against both external disturbances and modeling imprecision (Utkin, 1981; Drakunov, 1983; Slotine and Sastry, 1983; Slotine and Li, 1991; Qian and Ma, 1992; Hung et al, 1993; Choi and Park, 1994; Choi et al, 1995; Khalil, 1996; Rundell et al., 1996; Young et al, 1996; Gokasan et al, 1998; Kim and Inman, 2004; Le et al, 2004; Bazzi and Chalhoub, 2005; Chalhoub et al., 2006; Lian and Wang, 2010; Khaled and Chalhoub, 2010; Wang and Yau, 2011; Khaled and Chalhoub, 2011; Pisano and Usai, 2011; Chalhoub and Khaled, 2014). They are designed based on nominal models of the plant, which may suffer from substantial structured and unstructured uncertainties. The robust performances of these sliding mode controllers (SMC) necessitate the knowledge of the upper bound on both system’s uncertainties and disturbances. This type of controllers is very attractive for maritime applications since the dynamic models of a marine vessel involve a tremendous level of uncertainties, particularly, when the system operates in environmental conditions that are conducive to ice accretion on the ship hull.

It should be noted that the SMC methodology has a drawback stemming from the chattering that occurs when the system is in the vicinity of the sliding surface. A great deal of work has been done to rectify this problem (Slotine and Sastry, 1983; Park and Kim, 1991; Healey and Lienard, 1993; Kachroo and Tomizuka, 1996). Some substituted the discontinuous switching term by a predefined interpolation scheme within a specified boundary layer (Slotine and Sastry, 1983; Healey and Lienard, 1993). Others used low pass and variable bandwidth filters to smoothen all discontinuities in the vicinity of the sliding surface (Park and Kim, 1991; Kachroo and Tomizuka, 1996). These proposed schemes for handling the switching term have considerably reduced the chattering problem; thus, rendering the sliding mode methodology to be a feasible robust approach and facilitated its implementation in many fields.

Recent control schemes have been proposed to combine the advantages of both sliding mode methodology and the self-tuning fuzzy logic algorithm (Bazzi and Chalhoub, 2005; Chalhoub et al, 2006; Chalhoub and Khaled, 2009; Khaled and Chalhoub, 2009). Khaled and Chalhoub presented a self-tuning fuzzy-logic sliding mode controller for an under-actuated marine surface vessel. Using the guaranteed system stability through the sliding condition, this controller updates its fuzzy rules accordingly. The authors have successfully implemented this scheme, in digital simulations, on the heading control problem (Khaled and Chalhoub, 2010) and as a part of an integrated guidance and control system on a trajectory tracking problem (Khaled and Chalhoub, 2013). This scheme does not require accurate plant model or cumbersome construction of an adequate set of rules as long as the upper bounds on the uncertainties and external disturbances are known. The purpose of the current work is to experimentally validate the robustness of a sliding mode controller in tracking desired trajectories under different sea states.

1.3 Dissertation Overview

The focus of this work is to assess the adverse effects of non-collocated sensors and actuators on the performance of structural controllers, to propose remedial actions for minimizing such detrimental effect on the performance of structural controllers, to experimentally validate the capabilities of self-tuning and sliding mode observers in accurately estimating the state variables of a complex system in spite of significant modeling imprecision and external disturbances, and to experimentally prove the viability of using the estimated state variables in the computation of the control signals.

In Chapter 2, the adverse effects of non-collocated sensors and actuators on the phase characteristics of flexible structures and the ensuing implications on the performance of structural controllers are discussed. The formulation builds on the work done by Spector and Flashner (1990) and explores remedial schemes, based on the phase angle contour of the system, to enhance the capabilities of structural controllers in order to ensure a desirable and robust performance of the closed-loop system irrespective of the sensor location with respect to the actuator.

Chapter 3 focuses on providing experimental validation for the robust performances of a self-tuning observer (Khaled and Chalhoub, 2012; Khaled and Chalhoub, 2014) and a sliding mode observer (Chalhoub and Kfoury, 2005). In this Chapter, the experimental results were generated in a completely controlled environment on a flexible robotic manipulator. The challenges of this system emanate from the fact that the natural frequencies of the system are configuration-dependent. The observers are designed based on both the variable structure systems theory and the self-tuning fuzzy logic scheme. Their robustness and self-tuning characteristics allow one to use an imprecise model of the system and eliminate the need for the extensive tuning associated with a fixed rule-based expert fuzzy inference system.

In Chapter 4, the observers were tested under a completely uncontrolled environment consisting of a 16-ft boat operating in open-water under different sea states. Such experimental work necessitates the development of a supervisory control algorithm, which encompasses a guidance system, two types of nonlinear observers along with different control schemes to perform PTP tasks, prescribed throttle arm and steering tasks, surge speed and heading tracking tasks, or recovery maneuvers. This system has been implemented herein to perform prescribed throttle arm and steering control tasks based on estimated rather than measured state variables. These experiments served to validate the observers in a completely uncontrolled environment and proved their viability as reliable techniques for providing accurate estimates for the required state variables.

Chapter 5 summarizes the present work, highlights the main contributions, and suggests future research topics.

CHAPTER 2 IMPACT OF NON-COLLOCATED SENSORS AND ACTUATORS ON THE PERFORMANCES OF STRUCTURAL CONTROLLERS

The aim of this chapter is to investigate and analyze the adverse effects of non-collocated sensors and actuators on the phase characteristic of flexible structures and the ensuing implications on the performance of structural controllers. Moreover, remedial actions have been suggested to enhance the capabilities of common structural controllers in dealing with flexible structures whose sensors and actuators are considerably non-collocated.

For this purpose, two closed-loop systems, involving a pinned-free and clamped-free deformable beam, are considered. Their closed-loop transfer functions are derived from which the corresponding phase angle contours are generated as functions of the normalized sensor location and the excitation frequency. Furthermore, two structural controllers are designed for these systems based on the sliding mode methodology and the active damping control strategy to damp out the unwanted in-plane transverse deformations of the beams. These controllers are then modified, based on phase angle contours information, to yield good closed-loop performances irrespective of the location of the sensor with respect to the actuator.

2.1 Dynamic Modeling of Selected Flexible Structures

Two systems have been considered in the current work. The first one consists of a pinned-free beam with the control torque applied at its pinned-end (see Fig. 2-1). The second system is a clamped-free beam with the control moment generated by two piezoelectric actuators that are bonded to the top and bottom surfaces of the beam at a distance ranging from x_1 to x_2 from the fixed-end of the beam (see Fig. 2-2). In both systems, the in-plane transverse deformation is assumed to be measured by a sensor located at an arbitrary distance, x^*, from either the pinned-end or the fixed-end of the flexible beams. The geometric and material properties for both systems are listed in Table 2-1.

These two systems have been selected because of their greatly differing phase angle contours. For instance, the elastic modes of a pinned-free beam have one or more elastic nodes, signaling the presence of two or more separate phase regions. However, the first elastic mode of a clamped-free beam has no nodes, which is indicative of a uniform phased region.

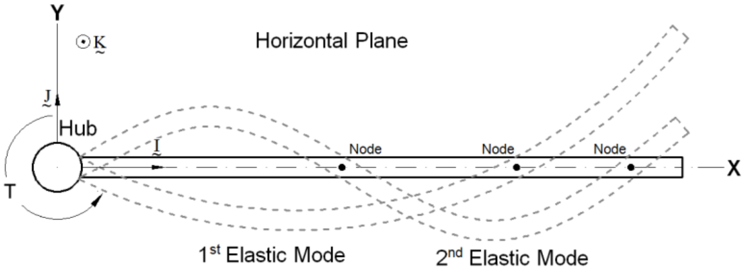

Fig. 2-1. Schematic of the pinned-free beam

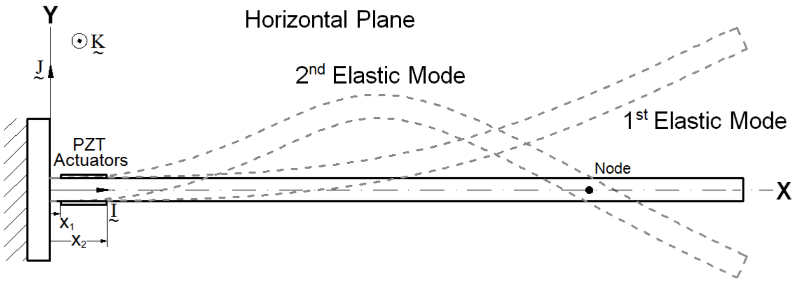

Fig. 2-2. Schematic of the clamped-free beam

Pinned-Free Beam Geometric Properties	
Beam Length, L	1 m
Diameter, D	0.00635 m
Cross-sectional Area, A	0.0000316692 m^2
Area Moment of Inertia, I	7.9811×10^{-11}m^4
Clamped-Free Beam Geometric Properties	
Beam Length, L	1 m
Beam Width, b	0.0254 m
Beam Thickness, h	0.003175m
Cross-sectional Area, A	0.000080645 m^2
Area Moment of Inertia, I	6.7746×10^{-11}m^4
PZT Geometric Properties	
PZT Length, L_{pe}	0.05 m
PZT Thickness, h_{pe}	0.001 m
Strain Constant, d_{31}	-166×10^{-12} m/V
Material Properties	
Aluminum Modulus of Elasticity, E	70 GPa
Density of Aluminum, ρ	2700 Kg/m^3
PZT Modulus of Elasticity, E_{pe}	63 GPa
PZT Density, ρ_{pe}	7650 Kg/m^3
Damping Coefficients, $c_i\,(c_1 = c_2)$	0.001 N.s/m

Table 2-1. Geometric and Material Properties of the pinned-free and clamped-free systems

2.1.1 Pinned-Free Beam Formulation

The position vector of an arbitrary point on the beam can be expressed as

$$\underset{\sim}{r} = x\,\underset{\sim}{i} + w_{PF}\,(\,x\,,t\,)\,\underset{\sim}{j} \tag{2-1}$$

The in-plane transverse deformation, $w_{PF}\,(\,x\,,t\,)$, is approximated by implementing the assumed modes method as follows (Meirovitch, 1967).

$$w_{PF}\,(\,x\,,t\,) = \sum_{i=1}^{n} \Phi_{PF_i}(x)\,q_{PF_i}(t) \tag{2-2}$$

Based on the Euler-Bernoulli beam theory, the i^{th} eigenfunction, Φ_{PF_i}, for a pinned-free beam can be written as (Young and Felgar, 1949)

$$\begin{aligned}\Phi_{PF_i}(x) = \cosh\left[\beta_{PF_i}(L-x)\right] + \cos\left[\beta_{PF_i}(L-x)\right] \\ - \alpha_{PF_i}\left(\sinh\left[\beta_{PF_i}(L-x)\right] + \sin\left[\beta_{PF_i}(L-x)\right]\right)\end{aligned} \tag{2-3}$$

Note that the effects of rotary inertia and shear deformation are negligible in the current work because the length of the beam is greater than ten times its width. The kinetic energy is expressed as

$$KE_{PF} = \frac{1}{2}\int_m \left(\dot{\underset{\sim}{r}} \cdot \dot{\underset{\sim}{r}}\right) dm \tag{2-4}$$

Whereas the strain energy stored in the beam is given by

$$SE_{PF} = \frac{1}{2}\int_0^L EI\left(\frac{\partial^2 w_{PF}(x,t)}{\partial x^2}\right)^2 dx \tag{2-5}$$

The structural damping of the deformable beam is accounted for by using the Rayleigh's dissipation function, which can be written as (Meirovitch, 1975)

$$D = \frac{1}{2}\sum_{i=1}^{n} c_i \dot{q}_{PF_i}^2 \tag{2-6}$$

The virtual work performed by the non-conservative control torque, $T(x=0,t)$, is determined from

$$\delta W_{NC} = T\left(0,t\right)\sum_{i=1}^{n}\left[\left.\frac{d\,\Phi_{PF_i}\left(x\right)}{dx}\right|_{x=0}\delta q_{PF_i}\left(t\right)\right] \tag{2-7}$$

The Lagrange principle was then implemented to derive the equations of motion, which can be written in the following compact state equation form:

$$\dot{\underset{\sim}{x}}_{PF} = A_{PF}\,\underset{\sim}{x}_{PF} + B_{PF}\,T(0,t) \tag{2-8}$$

where the state vector is defined to be $\underset{\sim}{x}_{PF} = \left[q_{PF_1} \cdots q_{PF_n} \mid \dot{q}_{PF_1} \cdots \dot{q}_{PF_n}\right]^T$. The expressions for A_{PF} and B_{PF} matrices are given in Appendix A for the special case where $w_{PF}\left(x,t\right)$ is considered to be dominated by the first two elastic modes (i.e., $n = 2$). Note that the B_{PF} matrix is constant because the actuator is fixed at the pinned-end of the beam. The measured signal is assumed to be the in-plane transverse deformation at the sensor location, $w_{PF}\left(x^*,t\right)$, which results in the following output equation

$$y_{PF} = C_{PF}\,\underset{\sim}{x}_{PF} = \left[\Phi_{PF_1}\left(x^*\right) \;\cdots\; \Phi_{PF_n}\left(x^*\right) \mid \underset{\sim}{0}_{1\times n}\right]\underset{\sim}{x}_{PF} \tag{2-9}$$

As can be seen, C_{PF} matrix solely depends on the sensor's location, x^*. The corresponding transfer function of the system can then be generated from

$$\frac{W_{PF}\left(x^*,s\right)}{T\left(0,s\right)} = G_{PF}\left(x^*,s\right) = \frac{N_{PF}\left(x^*,s\right)}{D_{PF}\left(s\right)} = \frac{\bar{a}_1\left(x^*\right)s^{2n-2} + \cdots + \bar{a}_{2n-1}\left(x^*\right)}{\bar{b}_1 s^{2n} + \cdots + \bar{b}_{2n+1}} \tag{2-10}$$

The coefficients of the above transfer function are listed in Appendix A for the special case of $n = 2$. Since A_{PF} in Eq. (2-8) is constant then the poles of the system, governed by $\left| sI - A_{PF} \right| = 0$, will be fixed in the complex plane. On the other hand, the C_{PF} matrix in Eq. (2-9) renders the $\bar{a}_i$ coefficients of Eq. (2-10) to be functions of x^*. This will hence result in the zeros of the system being dependent on the sensor location.

2.1.2 Clamped-Free Beam Formulation

The procedure for deriving the transfer function of the clamped-free beam is similar to the one described in Subsection 2.1.1. The in-plane transverse deformation, $w_{CF}(x,t)$, is approximated as follows (Meirovitch, 1967)

$$w_{CF}(x,t) = \sum_{i=1}^{n} \Phi_{CF_i}(x) q_{CF_i}(t) \tag{2-11}$$

where the eigenfunction $\Phi_{CF_i}(x)$ is expressed as (Young and Felgar, 1949)

$$\Phi_{CF_i}(x) = \cosh\left[\beta_{CF_i} x\right] - \cos\left[\beta_{CF_i} x\right] - \alpha_{CF_i}\left(\sinh\left[\beta_{CF_i} x\right] - \sin\left[\beta_{CF_i} x\right]\right) \tag{2-12}$$

The formulations for the kinetic energy, strain energy, and Rayleigh's dissipation function follow directly from Eqs. (2-4) to (2-6). The virtual work done by the two piezoelectric patches is determined from (Crawley and De Luis, 1987; Fuller et al, 1996; Yang and Lee, 1994)

$$\delta W_{NC} = -v_c\left(x_{pe},t\right)\frac{E\,I\,d_{31}K_f}{h_{pe}}\sum_{i=1}^{n}\left[\left.\frac{d\,\Phi_{CF_i}\left(x\right)}{dx}\right|_{x_1}^{x_2}\right]\delta q_{CF_i} \tag{2-13}$$

Where $x_{pe} = \frac{x_2 + x_1}{2}$ and $K_f = \frac{3E_{pe}\left[\left(h+h_{pe}\right)^2 - h^2\right]}{2\left[E_{pe}\left[\left(h+h_{pe}\right)^3 - h^3\right] + Eh^3\right]}$

Note that x_1 and x_2 are defined in Fig. 2-2. The Lagrange principle was then used to derive the governing equations of motion, which can be written with respect to the state variables as follows

$$\dot{\underset{\sim}{x}}_{CF} = A_{CF}\ \underset{\sim}{x}_{CF} + B_{CF}\ v_c\left(x_{pe},t\right) \tag{2-14}$$

where $\underset{\sim}{x}_{CF} = \left[q_{CF_1} \cdots q_{CF_n} \mid \dot{q}_{CF_1} \cdots \dot{q}_{CF_n}\right]^T$. The expressions for A_{CF} and B_{CF} matrices are given in Appendix B for the special case of $n = 2$. Similarly, since the actuator is fixed at x_{pe}, B_{CF} becomes a constant matrix. The measured signal is also selected to be the in-plane transverse deformation at the sensor location, $w_{CF}\left(x^*,t\right)$, which leads to the following output equation

$$y_{CF} = C_{CF}\ \underset{\sim}{x}_{CF} = \left[\Phi_{CF_1}\left(x^*\right) \quad \cdots \quad \Phi_{CF_n}\left(x^*\right) \quad \mid \quad \underset{\sim}{0}_{1\times n}\right]\underset{\sim}{x}_{CF} \tag{2-15}$$

It can be seen that C_{CF} solely depends on the sensor location, x^*. The corresponding transfer function of the system can hence be written as

$$\frac{W_{CF}\left(x^{*},s\right)}{V_{c}\left(x_{pe},s\right)}=G_{CF}\left(x^{*},s\right)=\frac{N_{CF}\left(x^{*},s\right)}{D_{CF}\left(s\right)}=\frac{\bar{\bar{a}}_{1}\left(x^{*}\right)s^{2n-2}+\cdots+\bar{\bar{a}}_{2n-1}\left(x^{*}\right)}{\bar{\bar{b}}_{1}s^{2n}+\cdots+\bar{\bar{b}}_{2n+1}} \qquad (2\text{-}16)$$

The coefficients in the above equation are provided in Appendix B for the special case of $n=2$. Since A_{CF} is a constant matrix then the poles of the system will be fixed in the complex plane. On the other hand, the dependency of $\bar{\bar{a}}_{i}$ terms on x^{*} causes the system's zeros to be affected by the sensor location.

2.2 Phase Angle Contours Analysis

As a way to visualize the impact of non-collocated sensor and actuator on the dynamic characteristics of flexible beams, the phase angle contours for both systems were generated, based on the derived transfer functions in Section 2.1, as functions of the normalized sensor location ($0\le\frac{x^{*}}{L}\le 1$) and the excitation frequency. These contours reveal the loci of the imaginary open-loop zeros along with the resulting minimum and non-minimum phase regions of the systems as the sensor sweep the entire span of the beam. Note that this work was conducted by assuming that both beams are governed by their first two elastic modes (i.e., $n=2$).

Figure 2-3 represents the contours of the phase angle of $G_{PF}\left(x^{*},j\omega\right)$. Curves PF-1 and PF-2 reveal the loci of the imaginary zeros of the system as the sensor location sweeps the entire beam length. The points of intercept of these curves with the natural frequency lines at $\omega_{n_1}^{PF}$ and $\omega_{n_2}^{PF}$ are the nodes of the elastic modes. As shown in Fig. 2-3, the contour space of $G_{PF}\left(x^*, j\omega\right)$ is partitioned into minimum and non-minimum phase regions. The development of such a map will aid in designing structural controllers that can be stable and effective irrespective of the relative location of the sensor with respect to the actuator.

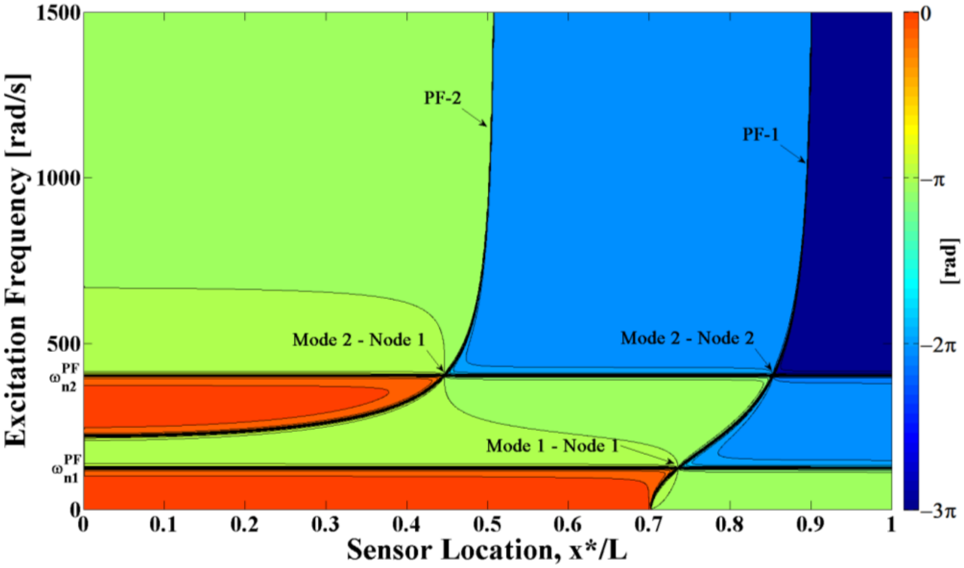

Fig. 2-3. Phase angle contour for a pinned-free beam modeled by considering two elastic modes with structural damping

The fine lines, appearing in Fig. 2-3 near the nodal and natural frequency lines, are induced by the gradual transition in the phase angle due to the structural damping terms. Such a transition will be abrupt in the case of zero damping; thus, resulting in the disappearance of the fine lines from the $G_{PF}\left(x^*, j\omega\right)$ phase contour. This is shown in Fig. 2-4, which was constructed under the same conditions of Fig. 2-3 while setting the damping terms to zero.

Figure 2-3 is validated by Fig. 2-5, which illustrates magnitude plots for $G\left(x^{*}, j\omega\right)$ corresponding to $\frac{x^{*}}{L}=0.2, 0.6, 0.72,$ and 0.88. For $\frac{x^{*}}{L}=0.2$, Fig. 2-5a shows a pole-zero-pole pattern, which agrees with the order in which a vertical line drawn at $\frac{x^{*}}{L}=0.2$ in Fig. 2-3 would intersect the $\omega_{n_1}^{PF}$, PF-2, and $\omega_{n_2}^{PF}$ curves.

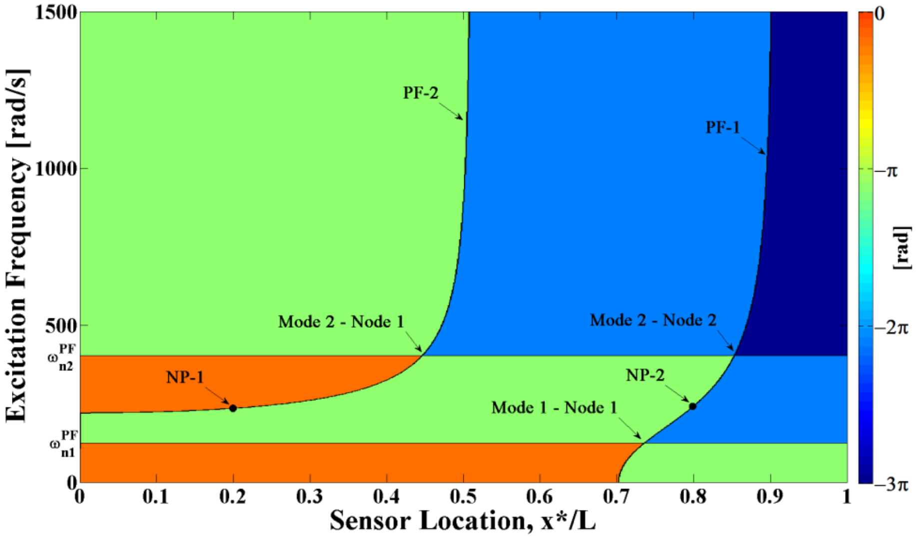

Fig. 2-4. Phase angle contour for a pinned-free beam modeled by considering two elastic modes without structural damping

It should be pointed out that for $0 \le \frac{x^{*}}{L} \le 0.507$, the system exhibits a "pole-zero" flipping phenomenon (Cannon and Rosenthal, 1984). Moreover, a vertical line at $\frac{x^{*}}{L}=0.6$ in Fig. 2-3 does not intersect either PF-1 or PF-2 curves, which is consistent with the pole-pole configuration of Fig. 2-5b. This indicates the migration of the system zeros from the imaginary to the real axis, which causes the system to become a non-minimum phase one. Such a characteristic change can have a destabilizing effect on the closed-loop system. A comparison between Figs. 2-5b and 2-5c reveals a change of pattern from a pole-pole configuration to a zero-pole-pole configuration, which is induced by the re-appearance of the imaginary zeros through the origin of the s-plane. This also demonstrates a characteristic change from a non-minimum to a minimum phase system. Similarly, Fig. 2-5d illustrates a pole-pole-zero pattern at $\frac{x^*}{L} = 0.88$. Further increase in the value of $\frac{x^*}{L}$, will ultimately cause the imaginary zero to migrate to the real axis as evidenced by the disappearance of the nodal lines in Fig. 2-3 for $\frac{x^*}{L} \geq 0.9$.

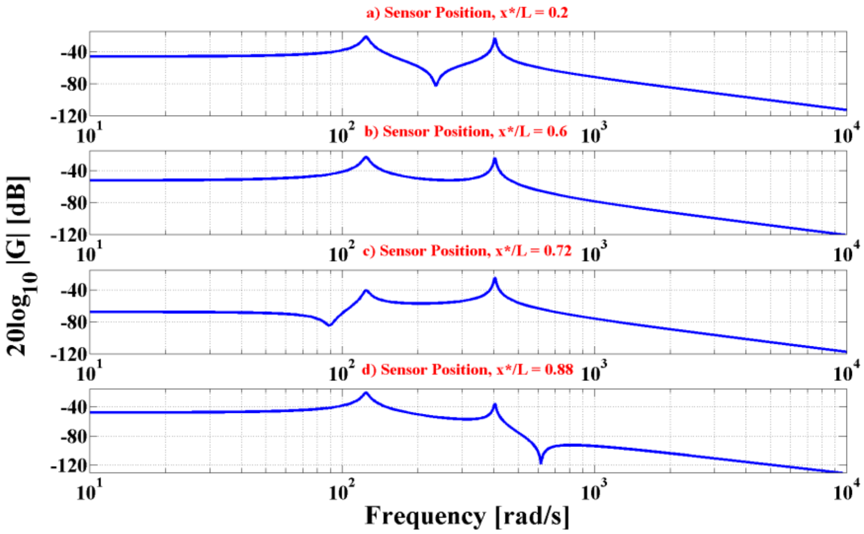

Fig. 2-5. Magnitude plots for the pinned-free beam corresponding to different sensor locations

The procedure described above can be easily expanded to include higher elastic modes of the beam. Figure 2-6 demonstrates the $G_{PF}\left(x^{*}, j\omega\right)$ phase angle contour for a system with three elastic modes. A comparison of Figs. 2-3 and 2-6 reveals similar partitioning pattern at low frequencies.

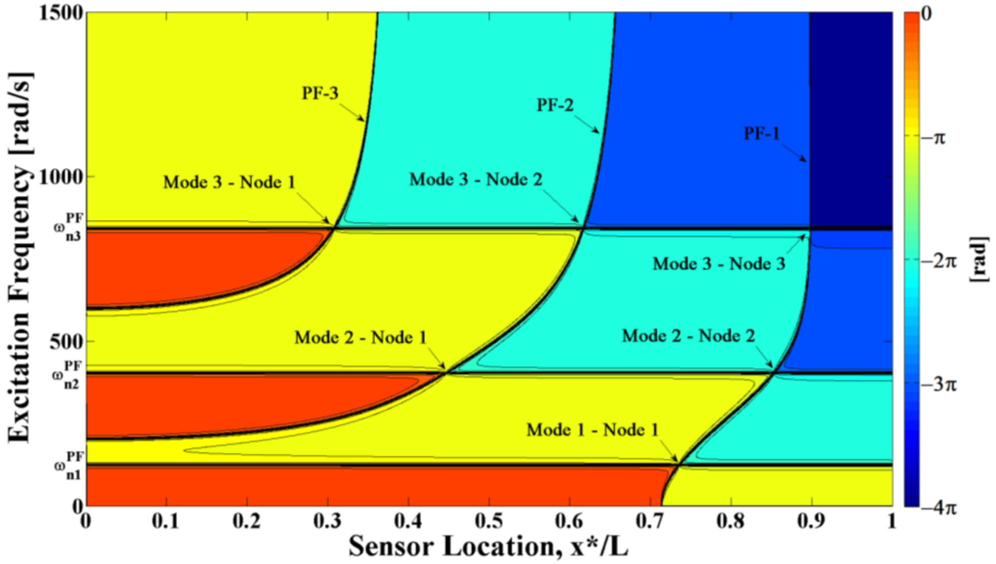

Fig. 2-6. Phase angle contour for a pinned-free beam modeled by considering three elastic modes with structural damping

The same has been done for the clamped-free beam. Figures 2-7 and 2-8 illustrate the contours of the phase angle of $G_{CF}\left(x^{*}, j\omega\right)$ as a function of the normalized sensor location ($0 \le \frac{x^{*}}{L} \le 1$) and the excitation frequency for the cases of $n = 2$ and $n = 3$, respectively. The terms CF-1 and CF-2 refer to nodal lines whose points of intercept with the natural frequency lines at $\omega_{n_1}^{CF}$, $\omega_{n_2}^{CF}$, and $\omega_{n_3}^{CF}$, are the modal nodes. Similar to the pinned-free case, the contour space of $G_{CF}\left(x^{*}, j\omega\right)$ is partitioned into minimum and non-minimum phase regions. Note that the fine lines in Figs. 2-7 and 2-8 in the vicinity of nodal and natural frequency lines are induced by the gradual transition in the phase angle due to the structural damping terms.

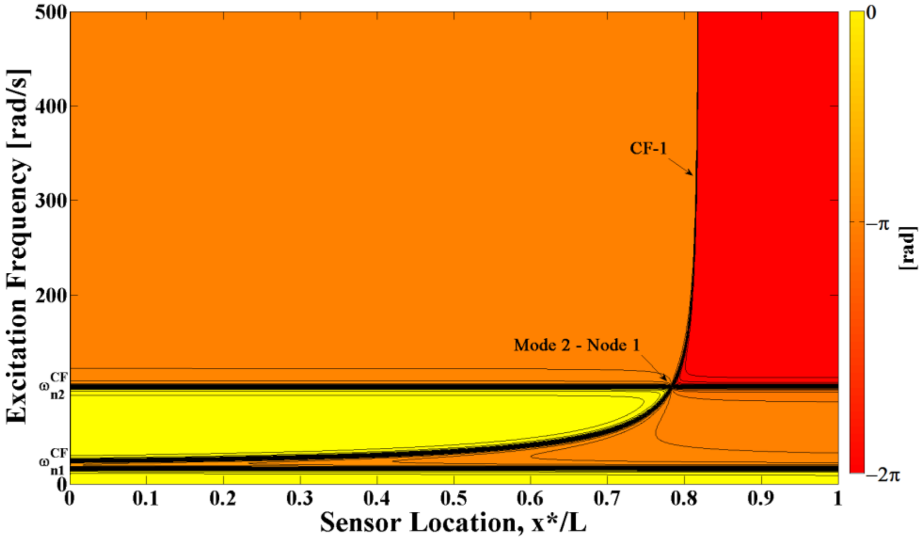

Fig. 2-7. Phase angle contour for a clamped-free beam modeled by considering two elastic modes with structural damping

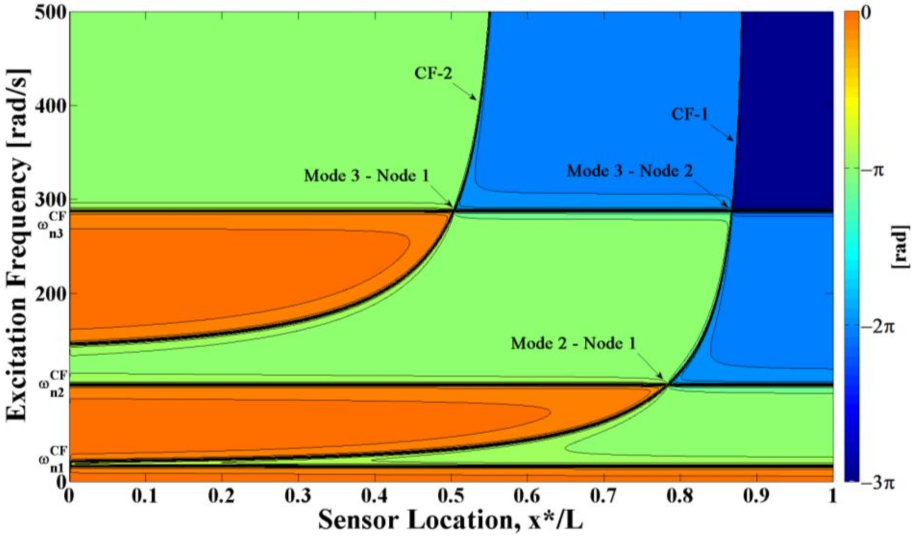

Fig. 2-8. Phase angle contour for a clamped-free beam modeled by considering three elastic modes with structural damping

2.3 Structural Controllers

The main concepts of the current work can similarly be illustrated on either the pinned-free or the clamped-free beam. Therefore, the current effort has focused on the pinned-free beam whose in-plane transverse deformation is assumed to be dominated by the first two elastic modes. Two structural controllers were devised to actively damp out the unwanted vibrations of the pinned-free beam. The first controller is based on the sliding mode methodology (Slotine and Li, 1991; Khalil, 1996), while the second one is an active damping controller (Yang and Mote, 1991; Yang, 1997).

2.3.1 Sliding Mode Controller

In designing the sliding mode controller for the pinned-free beam, the vector state equation of the nominal model of the plant can be written in the following form:

$$\dot{\hat{\underset{\sim}{x}}}_{PF} = \hat{\underset{\sim}{f}}_{PF}\left(\hat{\underset{\sim}{x}}_{PF}\right) + \hat{B}_{PF}\, T\left(0,t\right) \tag{2-17}$$

where $\hat{\underset{\sim}{x}}_{PF} = \left[w_{PF}\ \ \dot{w}_{PF}\right]^T$, $\hat{\underset{\sim}{f}}_{PF} = [\dot{w}_{PF}\ \ \hat{f}_2^{PF}]^T$, and $\hat{B}_{PF} = [0\ \hat{B}_2^{PF}]^T$. $\hat{f}_2^{PF}$ and $\hat{B}_2^{PF}$ can be reduced from Eq.(2-8) based on the fact that $\ddot{w}_{PF}\left(x,t\right) = \Phi_{PF_1}(x)\ddot{q}_{PF_1}(t) + \Phi_{PF_2}(x)\ddot{q}_{PF_2}(t)$. Their structured uncertainties are considered to be bounded as follows (Slotine and Li, 1991)

$$\left|f_2^{PF} - \hat{f}_2^{PF}\right|_{\sup} \le F_2^{PF} \tag{2-18a}$$

$$\hat{B}_2^{PF} = \sqrt{B_{2_{\min}}^{PF} B_{2_{\max}}^{PF}} \quad \text{and} \quad \bar{\beta}_{PF} = \sqrt{\frac{B_{2_{\max}}^{PF}}{B_{2_{\min}}^{PF}}} \tag{2-18b}$$

Select the following sliding surface:

$$s_{PF}\left(\dot{w}_{PF}, w_{PF}\right) = \dot{w}_{PF} + \lambda_{PF} w_{PF} \tag{2-19}$$

The structure of the control torque, $T(0,t)$, is given by

$$T(0,t) = T_{eq}(0,t) - \frac{k_{PF}}{\hat{B}_2^{PF}} \operatorname{sgn}\left(s_{PF}\right) \tag{2-20}$$

By setting $\dot{s}_{PF}$ to 0, one can determine $T_{eq}(0,t)$ to be

$$T_{eq}(0,t) = -\left(\hat{B}_2^{PF}\right)^{-1}\left[\hat{f}_2^{PF} + \lambda_{PF}\dot{w}_{PF}\right] \tag{2-21}$$

By satisfying the sliding condition, k_{PF} can be determined from

$$k_{PF} \geq \bar{\beta}_{PF}\left[F_2^{PF} + \eta_{PF}\right] + \left|\bar{\beta}_{PF} - 1\right|\left|\hat{f}_2^{PF} + \lambda_{PF}\dot{w}_{PF}\right| \tag{2-22}$$

The chattering problem has been alleviated by substituting $\operatorname{sgn}\left(s_{PF}\right)$ with the saturation $\operatorname{sat}\left(\frac{s_{PF}}{\phi_{PF}}\right)$ term. In order to cope with situations where the non-collocated sensor and actuator are located on opposite sides of the nodal line, the expression for $T(0,t)$ in Eq. (2-20) has been modified to yield

$$T\,(0,t) = \left[T_{eq}\,(0,t) - \frac{k_{PF}}{\hat{B}_{PF_2}} \operatorname{sgn}\left(s_{PF}\right) \right] g_{PF} \tag{2-23}$$

For $0 \le \frac{x^*}{L} \le 0.507$, both sensor and actuator are located on the same side of the PF-2 nodal line. In this region, the sensor and actuator signals are in phase and g_{PF} is assigned a $+1$ value. However for $0.702 \le \frac{x^*}{L} \le 0.9$, the sensor and the actuator are now located on opposite sides of the PF-1 nodal line. Thus, g_{PF} is assigned a -1 value to reflect the fact that the sensor and actuator signals are out-of-phase. In any case, the numerical value of g_{PF} is locked once the sensor location is fixed on the beam.

It should be pointed out that the inclusion of higher elastic modes in the truncated model has a tendency to modify existing nodal lines as well as creating new ones in the phase angle contour maps (see Figs. 2-3 and 2-6). In spite of this fact, the introduction of the g_{PF} term in the control action of Eq. (2-23) remains a viable approach for practical applications as long as all elastic modes, up to and including those that are likely to be excited, are considered in the truncated model.

2.3.2 Active Damping Control

The control action of the active damping compensator for the pinned-free beam is expressed as

$$\begin{aligned} T(0,t) &= -K_{PF_1}\dot{w}_{PF_1}\left(x^*,t\right) - K_{PF_2}\dot{w}_{PF_2}\left(x^*,t\right) \\ &= -\sum_{i=1}^{2} K_{PF_i}\Phi_{PF_i}\left(x^*\right)\dot{q}_i(t) = -\sum_{i=1}^{2} \bar{K}_{PF_i}\dot{q}_i(t) \end{aligned} \tag{2-24}$$

Using Eq. (2-24) into (2-8), one gets

$$\dot{\underset{\sim}{x}}_{PF} = \left(A_{PF} - B_{PF}\bar{K}_{PF}\right)\underset{\sim}{x}_{PF} \tag{2-25}$$

where $\bar{K}_{PF} = \begin{bmatrix} 0 & 0 & \bar{K}_{PF_1} & \bar{K}_{PF_2} \end{bmatrix}$. The ranges for $\bar{K}_{PF_1}$ and $\bar{K}_{PF_2}$ for which the closed-loop system of the pinned-free beam is asymptotically stable have been determined by satisfying the Routh-Hurwitz stability criterion, which leads to $\bar{K}_{PF_1} < 0$ and $\bar{K}_{PF_2} > 0$. Thus, the gains of the active damping controller in Eq. (2-24) become

$$K_{PF_i} = \frac{\bar{K}_{PF_i}}{\left|\Phi_{PF_i}\left(x^*\right)\right|}\operatorname{sgn}\left(\Phi_{PF_i}\left(x^*\right)\right) \qquad i = 1 \text{ and } 2 \tag{2-26}$$

Note that the controller gains are now explicit functions of the sensor's location.

2.4 Simulation Results

The control parameters for the sliding mode controller and the active damping controller are listed in Table 2-2. All simulations have been carried out based on the assumption that the in-plane transverse deformation of the pinned-free beam is dominated by the first two elastic modes. The undesired vibrations are induced by selecting the initial conditions of $\underset{\sim}{x}_{PF}$ to be $\left[0.01\ 0\ 0\ 0\right]^T$.

Sliding Mode Controller Parameters	
$\hat{f}_2^{PF}$	0
F_2^{PF}	10^4
$B_{2_{\min}}^{PF}$	10
$B_{2_{\max}}^{PF}$	500
λ_{PF}	5
η_{PF}	100
ϕ_{PF}	0.001
Active Damping Controller Parameters	
$\bar{K}_{PF_1}$	-96
$\bar{K}_{PF_2}$	140

Table 2-2. Controllers' parameters

2.4.1 Sliding Mode Controller Results

Initially, the sensor was assumed to be located at $\frac{x^*}{L} = 0.2$ and the sliding mode control (SMC) torque, $T(0,t)$, is computed based on Eq. (2-20). Figure 2-9 demonstrates the capability of the controller in driving the in-plane transverse deformation, $w_{PF}\left(x^*,t\right)$, to zero with no residual vibrations. Figure 2-10 reveals that the desired performance at x^* was achieved by having the sustained oscillation of the first elastic mode of the beam to be equal in magnitude and opposite in sign to that of the second elastic mode. As a consequence, the SMC control torque remained active and did not die out with time. This agrees with the frequency spectrum of $T(0,t)$, which also reveals that the controller drives the system at $\omega_{0.2}^* = 235.8$ rad/s (see Fig. 2-11). At this specific frequency, the bode plots for $G_{PF_1}(j\omega) = \dfrac{W_{PF_1}\left(x^*, j\omega\right)}{T\left(0, j\omega\right)}$ and $G_{PF_2}(j\omega) = \dfrac{W_{PF_2}\left(x^*, j\omega\right)}{T\left(0, j\omega\right)}$ have equal magnitudes and π phase angle difference. This is illustrated by point A in Fig. 2-12. In addition, one can easily prove that the numerator $N_{PF}\left(x^* = 0.2, j\omega^*_{0.2}\right)$ in Eq. (2-10) becomes 0 by setting ω to $\omega^*_{0.2}$, which explains the reason for the point NP-1 whose coordinates are $\left(x^* = 0.2, \omega^*_{0.2}\right)$ to be located on the nodal line PF-2 (see Fig. 2-4).

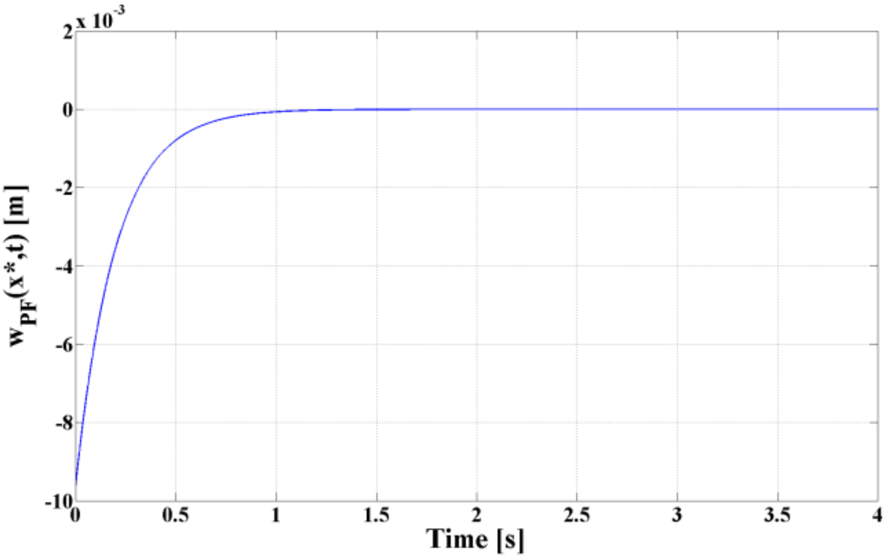

Fig. 2-9. In-plane transverse deformation of the pinned- free beam

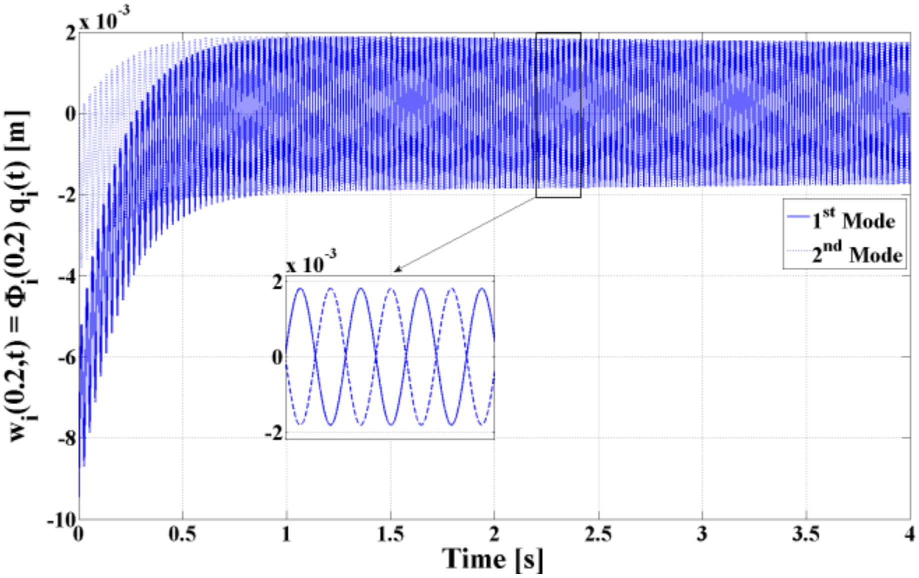

Fig. 2-10. Sustained oscillations of the first and second elastic modes of the pinned-free beam

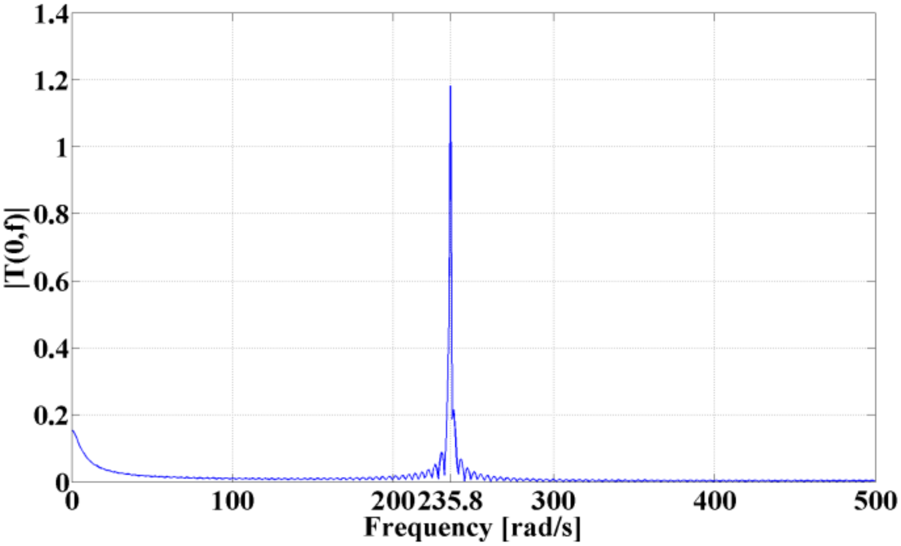

Fig. 2-11. Frequency spectrum of the control torque

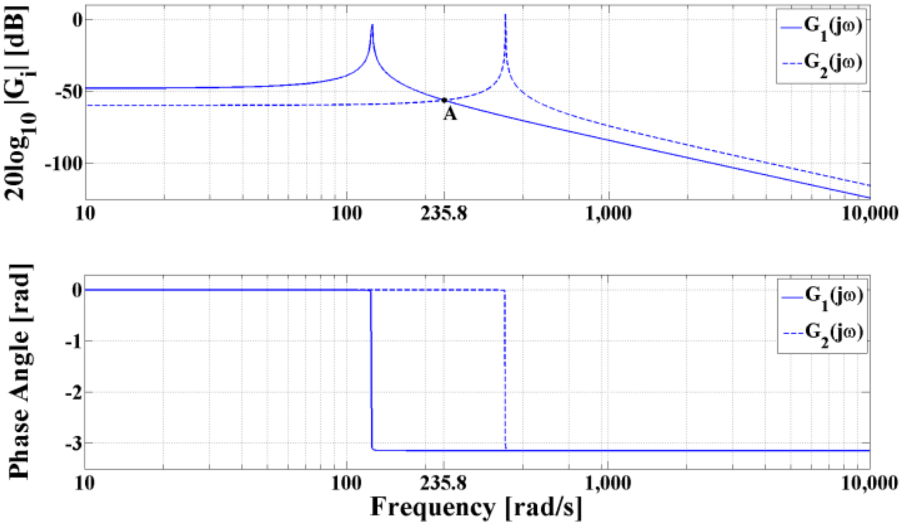

Fig. 2-12. Bode plots for $G_{PF_1}(j\omega)$ and $G_{PF_2}(j\omega)$

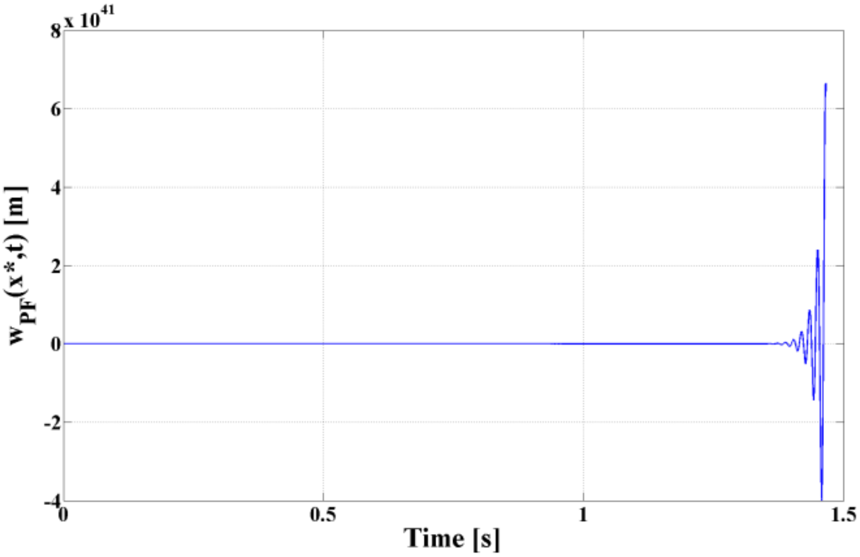

Fig. 2-13. Unstable response of the beam due to the relocation of the sensor to $\frac{x^*}{L} = 0.6$

In essence, the objective of the SMC is to drive the system toward the sliding surface of Eq. (2-19) and to quell any excursion of the system from s_{PF}. Physically, this translates to only setting $w_{PF}\left(x^*, t\right)$ to zero, which apparently has been realized by the SMC through equating $\Phi_{PF_1}(x^*)\,q_{PF_1}(t)$ to $-\Phi_{PF_2}(x^*)\,q_{PF_2}(t)$. It should be emphasized that the success of such a control strategy in driving $w_{PF}\left(x^*,t\right)$ to zero hinges upon the existence of imaginary zeros for the $\dfrac{W_{PF}\left(x^*,s\right)}{T\left(0,s\right)}=G_{PF}\left(x^*,s\right)$ transfer function. Otherwise, such a control strategy will fail. This can be easily illustrated by relocating the sensor to $\dfrac{x^*}{L}=0.6$, which corresponds to the case of no imaginary zero for $G_{PF}\left(x^*,s\right)$ since a vertical line drawn at $\dfrac{x^*}{L}=0.6$ in Fig. 2-3 would not intersect any nodal line. Figure 2-13 shows the unstable response of the in-plane transverse deformation of the beam when the SMC control torque is computed based on Eq. (2-20) while the sensor is located at $\dfrac{x^*}{L}=0.6$. A comment is in order at this stage. The absence of imaginary zeros in $G_{PF}\left(x^*,s\right)$ at $\dfrac{x^*}{L}=0.6$ is due to the fact that the dynamic model, used in the simulation, considers only two elastic modes. It should be emphasized that $G_{PF}\left(x^*,s\right)$ at $\dfrac{x^*}{L}=0.6$ will have imaginary zeros if higher elastic modes are included in the formulation. This is illustrated in the phase angle contour of Fig. 2-6, which was generated by considering three elastic modes. Therefore, the SMC should theoretically be able to stabilize the system by driving it at a much higher frequency than $\omega^*_{0.2}$. The feasibility and the success of such a controller will solely be determined by the bandwidth of the actuator.

On the other hand, if the sensor is relocated to $\frac{x^*}{L} = 0.8$ then the control torque of Eq. (2-20) will yield an unstable response (see Fig. 2-14). To address the instability issue induced by the out-of-phase sensor and actuator signals, the control torque is now computed based on Eq. (2-23). The in-plane transverse deformation of the beam, shown in Fig. 2-15, reveals a stable response similar to the one obtained when the sensor was located at $\frac{x^*}{L} = 0.2$. Once again, the desired $w_{PF}\left(x^*, t\right)$ response was achieved by the controller through equating $\Phi_{PF_1}(x^*)\,q_{PF_1}(t)$ to $-\Phi_{PF_2}(x^*)\,q_{PF_2}(t)$.

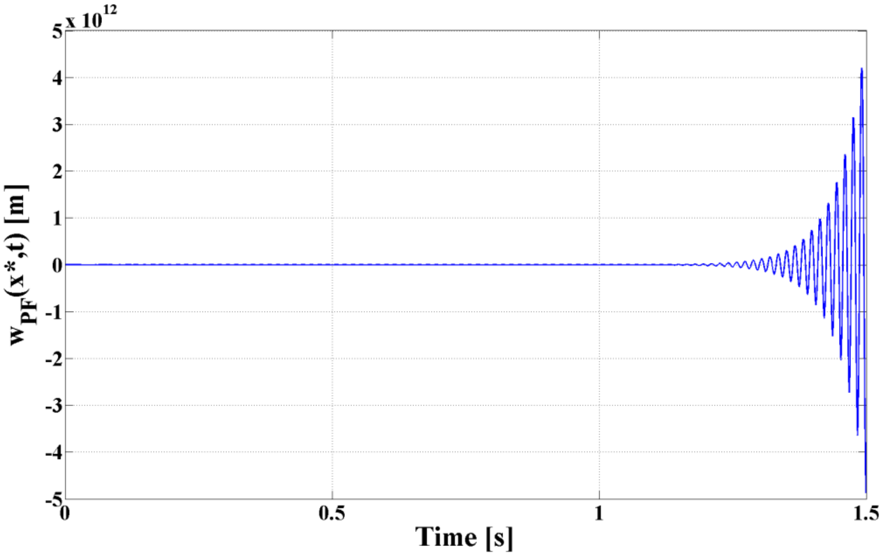

Fig. 2-14. Unstable response of the beam for $\frac{x^*}{L} = 0.8$

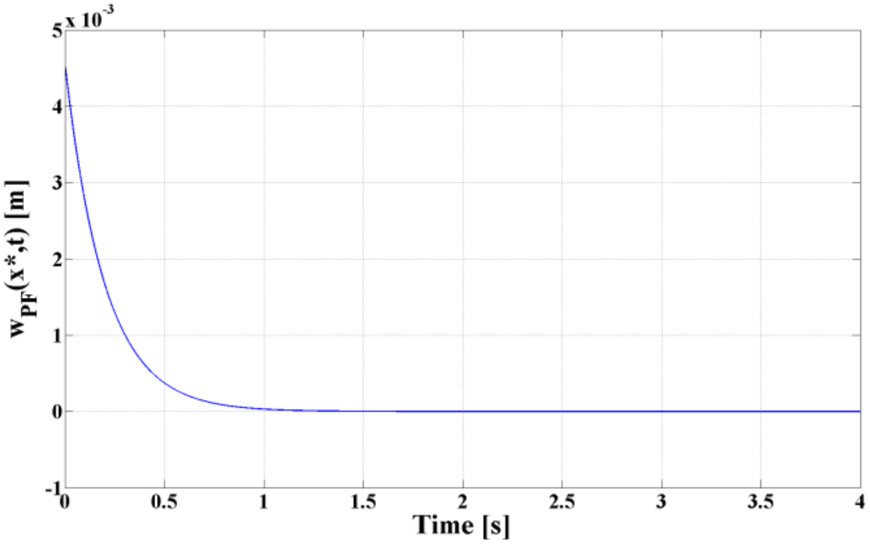

Fig. 2-15. Stable response of the beam for $\frac{x^*}{L} = 0.8$

2.4.2 Active Damping Controller Results

As a first step in assessing the performance of the active damping controller, the sensor was placed at $\frac{x^*}{L} = 0.2$ and the control action was determined based on Eq. (2-24). The result in Fig. 2-16 shows a similar pattern of response for $w_{PF}\left(x^*, t\right)$ as the one obtained by implementing the SMC (see Fig. 2-9). However, Fig. 2-17 reveals that the desired performance of $w_{PF}\left(x^*, t\right)$ was realized by both active damping and having the elastic modes equal in magnitude and opposite in sign. This is verified by the decaying, equal in magnitude, and opposite in sign oscillatory responses of the first and second elastic modes of the beam (see Fig. 2-17). It should be pointed out that both the active damping controller and the SMC strive to yield closed-loop responses of the first and second elastic modes that are equal in magnitude and opposite in sign at x^*.

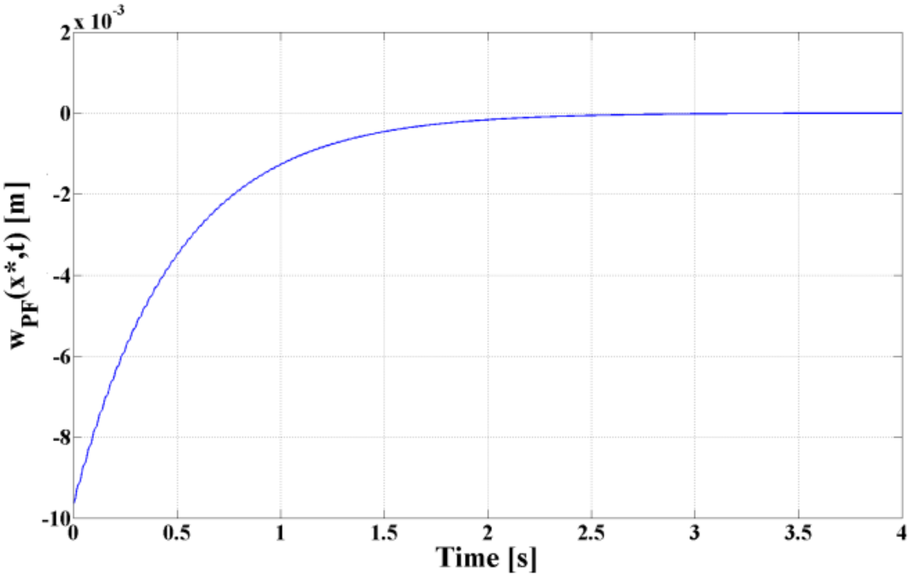

Fig. 2-16. In-plane transverse deformation of the pinned-free beam

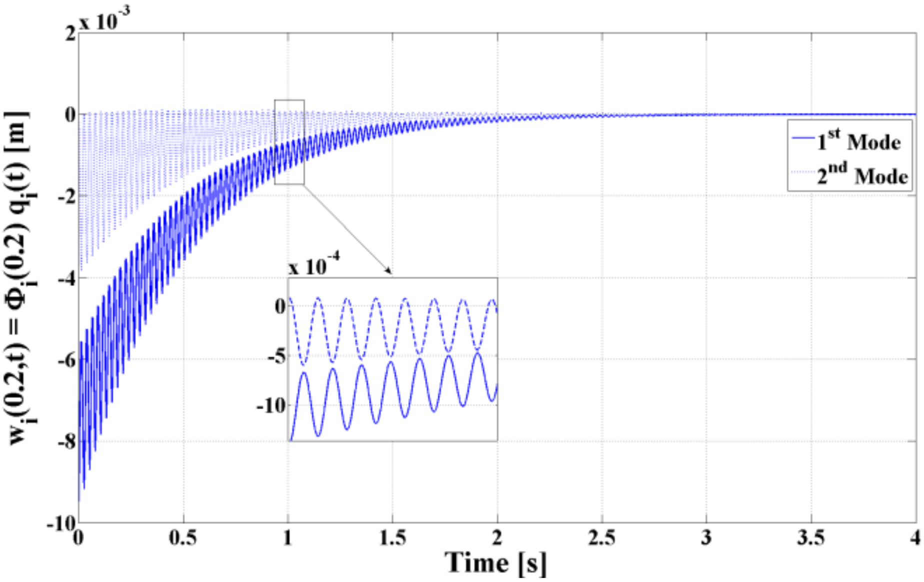

Fig. 2-17. Decaying oscillations of the first and second elastic modes of the pinned-free beam at $\frac{x^*}{L} = 0.2$

However, the active damping controller has an added dissipative feature that prevents the beam from indefinitely storing its strain energy, which causes the oscillations to decay down to zero with time. As a result, the in-plane transverse deformation at an arbitrary point on the beam, $w_{PF}(x,t)$, decays down to zero. This serves to highlight the performance differences between the active damping controller and the above SMC. Note that the latter only ensures that the in-plane transverse deformation at the sensor location, $w_{PF}\left(x^*,t\right)$, is zero.

Moreover, the control torque of the active damping controller decayed with time, which explains the large DC component and the smearing of its frequency spectrum around $\omega^*_{0.2} = 235.8$ rad/s (see Fig. 2-18). The latter is the same excitation frequency as the one appearing in the frequency spectrum of the SMC control torque (see Fig. 2-11). The explanation for obtaining the same value for the excitation frequency follows the reasoning given in subsection 2.4.1 for the SMC.

Furthermore, the dissipative nature of the active damping controller causes the unwanted vibrations of the beam to be eliminated in spite of the absence of zeros in the $G_{PF}\left(x^*,s\right)$ transfer function. This is illustrated in Fig. 2-19, which shows the system response corresponding to $\frac{x^*}{L} = 0.6$.

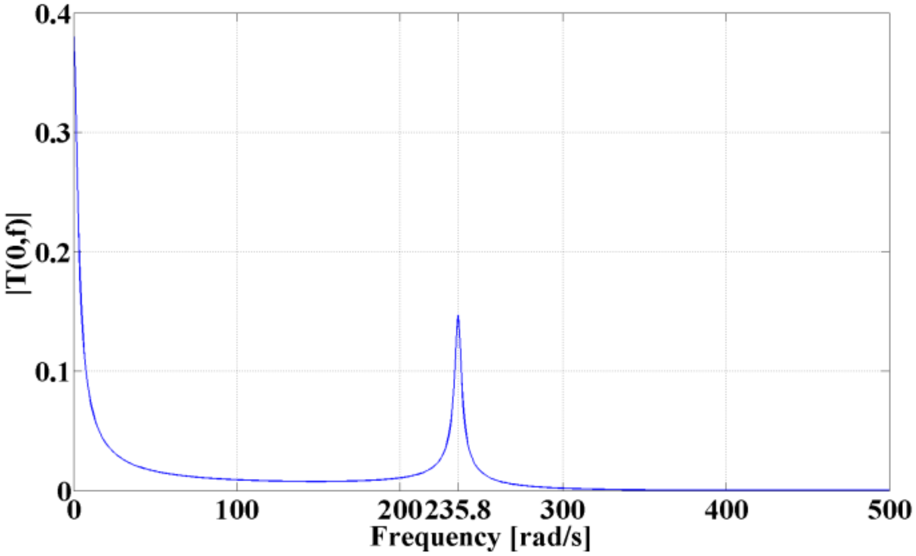

Fig. 2-18. Frequency spectrum of the control torque

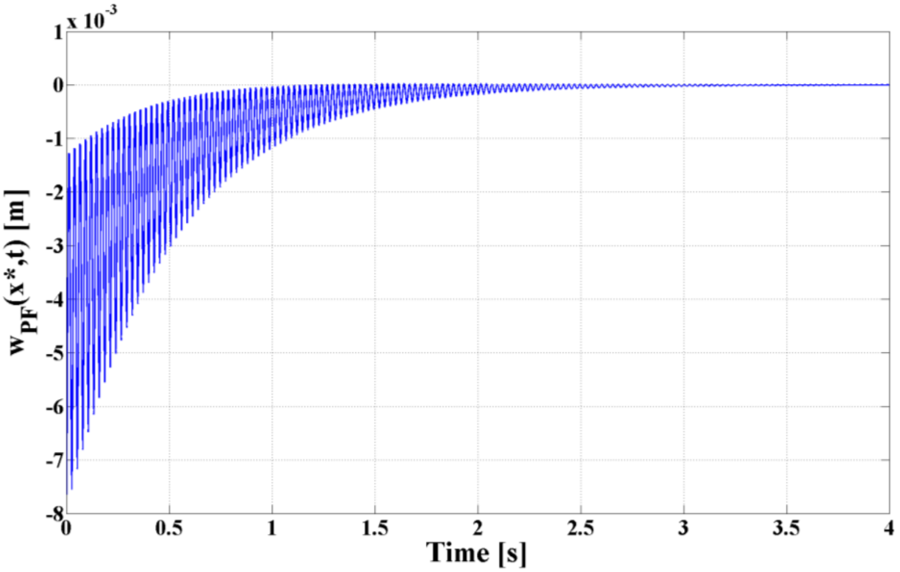

Fig. 2-19. Stable response of the beam for $\frac{x^*}{L} = 0.6$

The results of Figs. 2-20 and 2-21 were generated based on a sensor location at $\frac{x^*}{L} = 0.8$ while computing the control action according to Eqs. (2-24) and (2-26). Figure 2-20 demonstrates a desirable stable response for $w_{PF}\left(x^*, t\right)$, which reflects the robustness of the proposed active damping controller to the adverse effects induced by the non-collocated sensor and actuator. Figure 2-21 shows the ability of the controller in damping out the unwanted vibrations of the first two elastic modes.

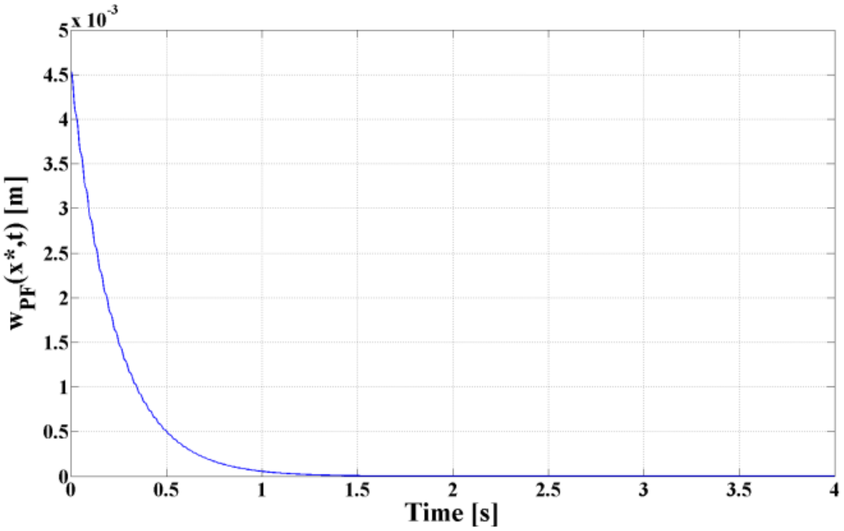

Fig. 2-20. Stable response of the beam for $\frac{x^*}{L} = 0.8$

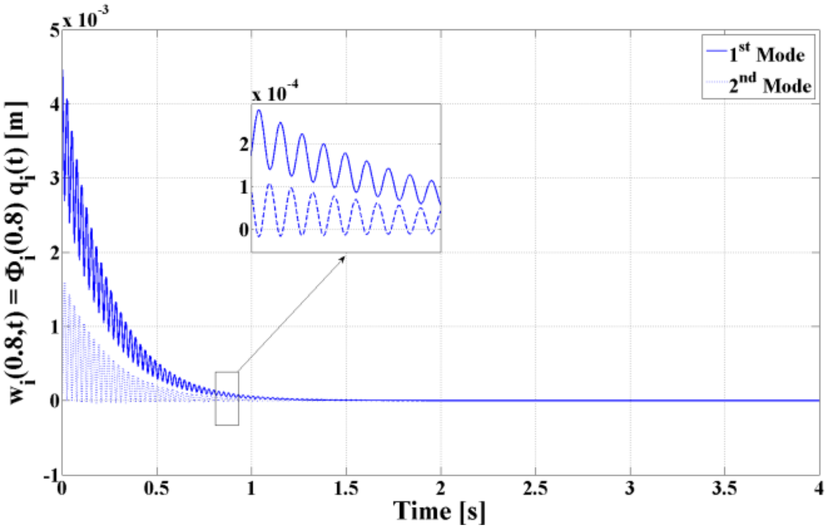

Fig. 2-21. Decaying oscillations of the first and second elastic modes of the pinned-free beam at $\frac{x^*}{L} = 0.8$

2.5 Summary and Conclusions

The present study investigates the adverse effects of non-collocated sensors and actuators on the performance of structural controllers. Two systems have been considered. The first one consists of a pinned-free beam with the control torque applied at the pinned-end. The second system is a clamped-free deformable beam with the control moment generated by two piezoelectric actuators that are bonded to the top and bottom surfaces near the clamped-end of the beam. The assumed modes method was implemented to approximate the in-plane transverse deformation of the pinned-free and clamped-free beams.

The phase angle contours for both systems have been generated as functions of the normalized sensor location and the excitation frequency. They clearly indicate the nodal lines and define the minimum and non-minimum phase regions pertaining to each system. Moreover, they reveal the changes in the pole-zero patterns of the systems as the sensor location is varied along the entire span of the beam.

Two structural controllers were designed to actively damp out the unwanted vibrations of the pinned-free beam. The first controller is based on the sliding mode methodology while the second one is an active damping controller. The simulation results have identified three distinct regions for the sensor's location whereby the performance of the sliding mode controller can be stable, unstable, or stable with a remedial action devised based on information provided by maps of the phase angle contour.

The simulation results revealed that the SMC tends to eliminate the overall in-plane transverse deformation at the sensor location by having the sustained oscillation of the first elastic mode to be equal in magnitude and opposite in sign to that of the second elastic mode.

Moreover, the results show that the proposed active damping controller eliminates the overall in-plane transverse deformation by both active damping and having the elastic modes equal in magnitude and opposite in sign. The dissipative nature of this controller prevents the beam from preserving its strain energy, which causes the unwanted vibrations to decay down to zero with time. In addition, the dependence of the controller gains on the mode shapes has enabled the proposed active damping controller to yield a stable response of the beam irrespective of the sensor location.

CHAPTER 3 THEORETICAL AND EXPERIMENTAL VALIDATION OF NONLINEAR ROBUST OBSERVERS ON A SPHERICAL ROBOTIC MANIPULATOR

Observers are essential for the implementation of controllers. Quite often the dynamics of the plant are highly nonlinear and not known exactly. Therefore, the observer should be able to handle significant modeling imprecision and be insensitive to unknown external disturbances. In this study, the self-tuning robust observer (Khaled and Chalhoub, 2012) along with a conventional sliding mode observer (Chalhoub and Kfoury, 2005) will be theoretically and experimentally validated on a challenging structure whose natural frequencies are configuration-dependent. The physical system is selected to be a spherical robotic manipulator with one flexible link. The prismatic joint induces significant variations in the natural frequencies of the deformable member. The observers are required to provide accurate estimates of the generalized coordinates of the flexible motion in the presence of significant modeling uncertainties. Two different modes of excitation of the flexible link were used. The first one involves disturbances in the initial conditions or the use of initial impulsive forces. While in the second mode, the structural deformations are induced by the rigid body motion of the arm during a tracking maneuver.

This Chapter covers the modeling aspect of the robotic manipulator along with the observers and controllers designs. Moreover, a detailed description of the experimental set-up is presented. The motivation behind carrying out such a study is to provide a much needed experimental results that are required for the experimental validation of numerous advanced nonlinear observers that have recently appeared in the literature.

3.1 Dynamic Model of the Robotic Manipulator

A spherical robotic manipulator is considered in this work primarily because of its two revolute and one prismatic joint. The schematic of the physical system, shown in Fig. 3-1, reveals the compactness and rigidity of the first two links. Therefore, these links are modeled as rigid bodies. In addition, both the payload and the segment of the third link located inside the second link are assumed to be rigid bodies. However, the portion of the third link protruding from the second link is considered to be flexible and undergoing both in-plane and out-of-plane transverse deformations. Since the deformable link is much stiffer in the axial direction than in flexure then its longitudinal deformation has been ignored.

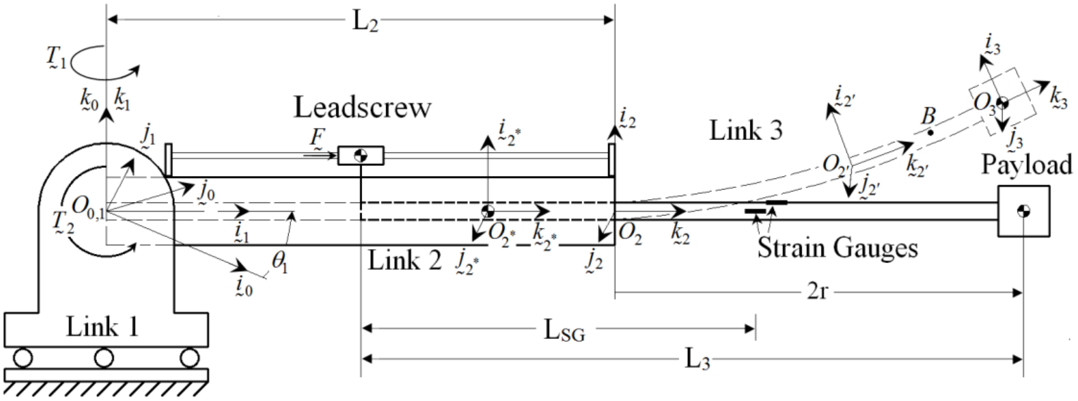

Fig. 3-1. Schematic of the spherical robot arm

The spherical robotic manipulator serves as an ideal and a very challenging test bed for assessing the performance of nonlinear observers in accurately estimating the state variables of a structure whose natural frequencies vary with its geometrical configuration. Since the third link is connected to a prismatic joint, its length can significantly vary during a single maneuver of the arm. A decrease in length will stiffen the deformable beam and cause its natural frequencies to increase. Conversely, an increase in length will soften the flexible link and cause its natural frequencies to decrease. As a consequence, a flexible beam connected to a prismatic joint will generally undergo significant parametric variations; thus, requiring the implementation of a nonlinear observer that is robust to structured uncertainties for the accurate estimation of the state variables of the system.

For the purpose of the current study, only the first and third links are considered in the derivation of the dynamic model of the robot. The current formulation represents a slight modification of the detailed model given in Refs. (Chen and Chalhoub, 1997; Chalhoub and Chen, 1998), which provides the rigid and flexible motion equations for a spherical robotic manipulator. The modified equations of motion are described herein in great detail.

An inertial coordinate system, $\{x_0, y_0, z_0\}$, is defined at O_0, which coincides with the pivot point of the second link and located on the axis of rotation of the first link. A body-fixed coordinate systems, $\{x_1, y_1, z_1\}$, is attached to the first link at point O_1, which coincides with O_0. Since the second joint is assumed to be inactive in this study then the second link is considered to be a pure inertia loading on the first joint. A second body-fixed coordinate systems, $\{x_2, y_2, z_2\}$, is attached to the end of the second link in order to systematically handle the kinematics of a compliant link with a prismatic joint. Note that the $z_2 -$ axis is defined to be tangential to the neutral axis of the deformable portion of the third link. Furthermore, a floating coordinate system, $\{x_{2'}, y_{2'}, z_{2'}\}$, is introduced to reflect the structural flexibility at an arbitrary point on the neutral axis of the protruding part of the third link (see Fig. 3-1). Moreover, the location and orientation of the payload are defined by the $\{x_3, y_3, z_3\}$ coordinate system whose origin coincides with the payload mass center.

The first link and the inactive second link rotate around an axis along $\underset{\sim}{k}_1$. Their combined kinetic energies can be written as

$$KE_1 = \frac{1}{2}\underset{\sim}{\omega}_1^{\{1\}^T} I_1 \underset{\sim}{\omega}_1^{\{1\}} = \frac{1}{2}\left(I_{z_1 z_1}^{link\ 1} + I_{z_1 z_1}^{link\ 2}\right)\dot{\theta}_1^2 \qquad (3\text{-}1)$$

where $\underset{\sim}{\omega}_1^{\{1\}} = \dot{\theta}_1 \underset{\sim}{k}_1$. The portion of the third link located inside the second link and the payload are treated as rigid bodies undergoing both translational and rotational motions. The extended position vectors of their mass centers are given by

$$\begin{Bmatrix} \underset{\sim}{r}_{2_r}^{*\{0\}} \\ 1 \end{Bmatrix} = T_{\{0\}}^{\{1\}} T_{\{1\}}^{\{2\}} \left[0 \quad 0 \quad -0.5\left(L_3 - 2r\right) \,\middle|\, 1\right]^T \qquad (3\text{-}2)$$

$$\begin{Bmatrix} \underset{\sim}{r}^{*\{0\}}_{p} \\ 1 \end{Bmatrix} = T^{\{1\}}_{\{0\}} T^{\{2\}}_{\{1\}} T^{\{2'_e\}}_{\{2\}} T^{\{3\}}_{\{2'_e\}} \left[0_{1\times 3} \;\middle|\; 1 \right]^{T} \tag{3-3}$$

where the $T^{\{i\}}_{\{j\}}$ transformation matrices can easily be generated from the D-H rules (Denavit and Hartenberg, 1955; Wolovich, 1987). $T^{\{3\}}_{\{2'_e\}}$ is a constant matrix defined such that the $\{x_3, y_3, z_3\}$ frame has the same orientation as the $\left\{x_{2'_e}, y_{2'_e}, z_{2'_e}\right\}$ coordinate system but its origin is located at the mass center of the payload. The kinetic energies of the rigid segment of the third link and the payload can be expressed as

$$KE_2 = \frac{1}{2} m_{3_r} \dot{\underset{\sim}{r}}^{*\{0\}}_{2_r} \cdot \dot{\underset{\sim}{r}}^{*\{0\}}_{2_r} + \frac{1}{2} \underset{\sim}{\omega}^{\{2\}^T}_{2_r} I_{3_r} \underset{\sim}{\omega}^{\{2\}}_{2_r} \tag{3-4}$$

$$KE_3 = \frac{1}{2} m_{p} \dot{\underset{\sim}{r}}^{*\{0\}}_{p} \cdot \dot{\underset{\sim}{r}}^{*\{0\}}_{p} + \frac{1}{2} \underset{\sim}{\omega}^{\{3\}^T}_{p} I_{p} \underset{\sim}{\omega}^{\{3\}}_{p} \tag{3-5}$$

where $\underset{\sim}{\omega}^{\{2\}^T}_{2_r} = \dot{\theta}_1 \underset{\sim}{i}_2$ and $\underset{\sim}{\omega}^{\{3\}}_{p} = \left(\dot{\theta}_1 + \dot{v}_{,z_2}\right) \underset{\sim}{i}_3 + \dot{u}_{,z_2} \underset{\sim}{j}_3 + \dot{\theta}_1 u_{,z_2} \underset{\sim}{k}_3$. Now, the extended position vector of an arbitrary point B on the flexible portion of the third link can be determined from

$$\begin{Bmatrix} \underset{\sim}{r}^{\{0\}}_{2'_B} \\ 1 \end{Bmatrix} = T^{\{1\}}_{\{0\}} T^{\{2\}}_{\{1\}} T^{\{2'\}}_{\{2\}} \left[x_{2'_B} \quad y_{2'_B} \quad 0 \;\middle|\; 1 \right]^{T} \tag{3-6}$$

where $\left(x_{2'_B}, y_{2'_B}, 0\right)$ are the coordinates of the point B with respect to the $\{x_{2'}, y_{2'}, z_{2'}\}$ frame. The structural transformation matrix $T^{\{2'\}}_{\{2\}}$ is defined as (Chen and Chalhoub, 1997; Chalhoub and Chen, 1998)

$$T_{\{2\}}^{\{2'\}} = \begin{bmatrix} 1 & 0 & u_{,z_2}\left(z_{2_B},t\right) & u\left(z_{2_B},t\right) \\ 0 & 1 & -v_{,z_2}\left(z_{2_B},t\right) & v\left(z_{2_B},t\right) \\ -u_{,z_2}\left(z_{2_B},t\right) & v_{,z_2}\left(z_{2_B},t\right) & 1 & z_{2_B} \\ 0 & 0 & 0 & 1 \end{bmatrix} \tag{3-7}$$

The term $T_{\{2\}}^{\{2'_e\}}$ in Eq. (3-3) can now be determined by evaluating the matrix $T_{\{2\}}^{\{2'\}}$ at $z_{2_B} = 2r$. The kinetic energy of the flexible portion of the third link is computed from

$$KE_4 = \frac{1}{2} \int_{m_{3_f}} \dot{\underset{\sim}{r}}_{2'_B}^{\{0\}} \cdot \dot{\underset{\sim}{r}}_{2'_B}^{\{0\}} dm_{3_f} \tag{3-8}$$

The total kinetic energy of the system is obtained by summing the KE_i terms from Eqs. (3-1, 3-4, 3-5 and 3-8). Next, the strain and potential energies of the system are given by

$$\begin{aligned} PE = \frac{1}{2}\int_0^{2r} EI_{z_2 z_2}\left[u_{,z_2 z_2}^2\left(z_2,t\right)+v_{,z_2 z_2}^2\left(z_2,t\right)\right]dz_2 + \int_0^{2r} \rho A_3 g\left(\underset{\sim}{r}_{2'_B}^{\{0\}} \cdot \underset{\sim}{k}_0^{\{0\}}\right)dz_2 \\ + m_p g\left(\underset{\sim}{r}_p^{*\{0\}} \cdot \underset{\sim}{k}_0^{\{0\}}\right) \end{aligned} \tag{3-9}$$

where the datum line is assumed to coincide with the x_0 –axis. Both out-of-plane and in-plane transverse deformations are approximated by the assumed modes method (Meirovitch, 1967). They are considered to be dominated by their first two elastic modes as follows

$$u(z_2,t) = \sum_{i=1}^{2} \Phi_{CF_i}(z_2) q_i(t) \tag{3-10}$$

$$v(z_2, t) = \sum_{i=1}^{2} \Phi_{CF_i}(z_2) q_{i+2}(t) \tag{3-11}$$

where Φ_{CF_i} is considered to be the i^{th} eigenfunction of a clamped-free beam derived based on the Euler Bernoulli beam theory (Young and Felgar, 1949). Note that the effects of rotary inertia and shear deformation are negligible in the current work because the length of the flexible portion of the third link is kept greater than ten times the width of the beam. The virtual work done by the non-conservative force and torque is determined from

$$\delta W_{NC} = T_1\, \delta\theta_1 + 2F\, \delta r + \delta W_{damp} \tag{3-12}$$

The δW_{damp} term captures the effects of viscous damping at the joints and the structural damping of the flexible portion of the third link. It is defined based on the Rayleigh's dissipation function, which yields

$$\delta W_{damp} = -\dot{\underset{\sim}{\alpha}}^T C\, \delta\underset{\sim}{\alpha} \tag{3-13}$$

where $\underset{\sim}{\alpha}^T = [\theta_1 \quad r \quad q_1 \quad q_2 \quad q_3 \quad q_4]$ and C is a diagonal matrix whose c_{11} and c_{22} entries reflect the viscous damping at the joints. They have been set to zero in the present study. However, c_{33} to c_{66} entries represent the structural damping coefficients for the flexible portion of the third link.

The six second order nonlinear ordinary differential equations of motion of the arm are then derived by implementing the Lagrange principle. The resulting equations are converted to twelve scalar state equations that can be written in the following compact form:

$$\dot{\underset{\sim}{x}} = \underset{\sim}{f}\left(\underset{\sim}{x}, \underset{\sim}{u}_c\right) \tag{3-14}$$

where $\underset{\sim}{x} = \left[\underset{\sim}{\alpha}^T \quad \dot{\underset{\sim}{\alpha}}^T\right]^T$ and $\underset{\sim}{u}_c^T = \left[T_1 \quad F\right]$.

3.2 Design of the Self Tuning Nonlinear Observer (STO)

The self-tuning observer is designed herein to estimate the variables pertaining to the in-plane and out-of-plane transverse deformations of the protruding part of the third link (i.e., q_1 to q_4 and their time derivatives). The measured signals are limited to the normal strains induced by flexure of the third link in the horizontal and vertical planes. These two measurements, which are generated by strain gauges (see Fig. 3-2), are used to determine the horizontal and vertical components of the equivalent concentrated load that is applied at the end of the third link. These force components enable us to determine the overall in-plane and out-of-plane transverse deformations at any point on the link. Since the current study considers two elastic modes only then both $u\left(z_2, t\right)$ and $v\left(z_2, t\right)$ are computed at two points defined by $z_2 = L_{m1}$ and $z_2 = L_{m2}$, respectively. The rationale is to use the values of $u\left(L_{m1}, t\right)$ and $u\left(L_{m2}, t\right)$ to determine the so-called $q_{1_m}\left(t\right)$ and $q_{2_m}\left(t\right)$ as follows

$$\begin{pmatrix} q_{1_m}\left(t\right) \\ q_{2_m}\left(t\right) \end{pmatrix} = \begin{bmatrix} \Phi_{CF_1}(L_{m1}) & \Phi_{CF_2}(L_{m1}) \\ \Phi_{CF_1}(L_{m2}) & \Phi_{CF_2}(L_{m2}) \end{bmatrix}^{-1} \begin{pmatrix} u\left(L_{m1}, t\right) \\ u\left(L_{m2}, t\right) \end{pmatrix} \tag{3-15}$$

Note that the above procedure can easily be generalized to determine the $q_{i_m}(t)$ terms with $i = 1, \cdots, n$ for systems with n elastic modes. Similar procedure has been followed to determine $q_{3_m}(t)$ and $q_{4_m}(t)$ from $v(L_{m1}, t)$ and $v(L_{m2}, t)$.

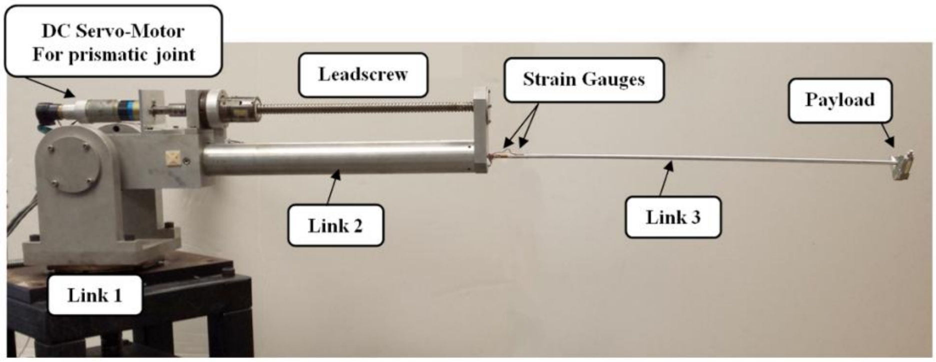

Fig. 3-2 Physical system

A reduced order model focusing on the structural deformations of the protruding part of the third link and excluding any rigid body motion of the arm has been used in the design of the observer. Its vector state equation is written as

$$\dot{\underset{\sim}{x}}_r = \underset{\sim}{f}_r\left(\underset{\sim}{x}_r, \underset{\sim}{u}_c\right) \tag{3-16}$$

where $\underset{\sim}{x}_r^T = [q_1, q_2, q_3, q_4, \dot{q}_1, \dot{q}_2, \dot{q}_3, \dot{q}_4]$ and $\underset{\sim}{f}_r^T = \left[x_{r_5}, x_{r_6}, x_{r_7}, x_{r_8}, f_{r_5}, f_{r_6}, f_{r_7}, f_{r_8}\right]$. Note that the f_{r_i} terms are assumed to be unknown. They are being approximated by their nominal $\hat{f}_{r_i}$ expressions that have been intentionally simplified to increase the effects of structured uncertainties. Let the structure of the observer be defined as (Khaled and Chalhoub, 2012)

$$\dot{\hat{x}}_{r_i} = \hat{x}_{r_{i+4}} - K_i \operatorname{sgn}(s_i) \qquad i = 1, \cdots, 4 \tag{3-17a}$$

$$\dot{\hat{x}}_{r_{j+4}} = \hat{f}_{r_{j+4}}\left(\underset{\sim}{\hat{x}}_r, \underset{\sim}{u}_c\right) + \left[\frac{\sum_{k=1}^{m} w_k^j r_k^j}{\sum_{k=1}^{m} w_k^j} - \gamma_j s_j^2 \frac{\sum_{k=1}^{m} \left(w_k^j\right)^2}{\left(\sum_{k=1}^{m} w_k^j\right)^2} \operatorname{sgn}\left(s_j\right) \right] \qquad j = 1, \cdots, 4 \quad \text{(3-17b)}$$

The following sliding surfaces are considered

$$s_i = \hat{x}_{r_i} - x_{r_{i_m}} = \tilde{x}_{r_i} = q_{i_e}\left(t\right) - q_{i_m}\left(t\right) \qquad i = 1, \cdots, 4 \qquad \text{(3-18)}$$

Consequently, the estimation error equation can be expressed as

$$\dot{\tilde{x}}_{r_i} = \tilde{x}_{r_{i+4}} - K_i \operatorname{sgn}(s_i) \qquad i = 1, \cdots, 4 \qquad \text{(3-19a)}$$

$$\dot{\tilde{x}}_{r_{j+4}} = \Delta f_{r_{j+4}} + \left[\frac{\sum_{k=1}^{m} w_k^j r_k^j}{\sum_{k=1}^{m} w_k^j} - \gamma_j s_j^2 \frac{\sum_{k=1}^{m} \left(w_k^j\right)^2}{\left(\sum_{k=1}^{m} w_k^j\right)^2} \operatorname{sgn}\left(s_j\right) \right] \qquad j = 1, \cdots, 4 \qquad \text{(3-19b)}$$

where the $\Delta f_{r_{j+4}}$ terms represent modeling imprecision. These terms are later on substituted, in the observer design, by their upper bounds $F_{j+4} = \left|\hat{f}_{r_{j+4}} - f_{r_{j+4}}\right|_{\sup}$ for $j = 1, \cdots, 4$, which are assumed to be known a priori. The gains, K_i, in Eq. (3-19a) are selected to satisfy the following sliding conditions

$$\frac{1}{2}\frac{d}{dt}\left(s_i^2\right) \le -\eta_i \left|s_i\right| \qquad i = 1, \cdots, 4 \qquad \text{(3-20)}$$

which yields

$$K_i \ge \eta_i + \left|\tilde{x}_{i+4}\right|_{upper\ bound} \qquad i = 1, \cdots, 4 \qquad \text{(3-21)}$$

In order to guarantee that the self-tuning process does not cause the observer to become unstable, the following additional set of Lyapunov functions are used

$$V_i = \frac{1}{2}\tilde{x}_{r_{i+4}}^2 \qquad i = 1,\cdots,4 \tag{3-22}$$

The γ_i tuning parameters are determined such that the time derivatives of the V_i functions are always negative definite. As a consequence, all $\tilde{x}_{r_{i+4}}$ for $i = 1,\cdots,4$, will continuously decrease with time. This scheme requires the γ_i terms to satisfy the following inequalities

$$\gamma_j > \frac{\left(\sum_{k=1}^{m} w_k^j\right)^2}{s_j^2 \sum_{k=1}^{m}\left(w_k^j\right)^2}\left[F_{j+4} + \frac{\sum_{k=1}^{m} w_k^j r_k^j\left(t-\Delta t\right)}{\sum_{k=1}^{m} w_k^j}\right] \quad \text{for} \quad j = 1,\cdots,4 \tag{3-23}$$

To alleviate the chattering problem, the $\operatorname{sgn}\left(s_j\right)$ term in Eq. (3-17b) has been replaced by the saturation function, $\operatorname{sat}\left(\frac{s_j}{\phi_j}\right)$.

3.3 Design of the Sliding Mode Observer (SMO)

The reduced order model, given in Eq. (3-16) and used in designing the STO, has also been used to design the SMO. The observer equations are given by

$$\dot{\hat{x}}_{r_i} = \hat{x}_{r_{i+4}} - K_i \operatorname{sgn}(s_i) \qquad i = 1,\cdots,4 \tag{3-24a}$$

$$\dot{\hat{x}}_{r_{i+4}} = \hat{f}_{r_{i+4}}\left(\underset{\sim}{\hat{x}}_r, \underset{\sim}{u}_c\right) - K_{i+4} \operatorname{sgn}(s_i) \qquad i = 1,\cdots,4 \tag{3-24b}$$

The sliding surfaces are selected to be the same as those used in the STO design, which are given in Eq. (3-18). Consequently, the error vector equation becomes

$$\dot{\tilde{x}}_{r_i} = \tilde{x}_{r_{i+4}} - K_i \,\mathrm{sgn}(s_i) \qquad i = 1, \cdots, 4 \tag{3-25a}$$

$$\dot{\tilde{x}}_{r_{i+4}} = \Delta f_{r_{i+4}} - K_{i+4} \,\mathrm{sgn}(s_i) \qquad i = 1, \cdots, 4 \tag{3-25b}$$

Again, the $\Delta f_{r_{i+4}}$ terms are eventually replaced $F_{i+4} = \left| \hat{f}_{r_{i+4}} - f_{r_{i+4}} \right|_{\sup}$ for $i = 1, \cdots, 4$, considered to be known a priori. The gains, K_i, in Eq. (3-25a) are selected by satisfying the sliding conditions of Eq. (3-20). They take on the following form:

$$K_i \geq \eta_i + \left| \tilde{x}_{i+4} \right|_{upper\ bound} \qquad i = 1, \cdots, 4 \tag{3-26}$$

The remaining gains of the observer are determined by ensuring that the time derivatives of the Lyapunov functions, defined in Eq. (3-22), are negative definite. As a result, these gains can be expressed as

$$K_{i+4} \geq \frac{F_{i+4} K_i}{\left| \tilde{x}_{i+4} \right|_{desired\_accuracy}} \qquad i = 1, \cdots, 4 \tag{3-27}$$

Once again, the chattering problem, induced by the switching terms, has been alleviated by employing the saturation function, $\mathrm{sat}\left(\dfrac{s_j}{\phi_j} \right)$.

3.4 Sliding Mode Rigid Body Controller

A basic sliding mode controller (SMC), similar in concept to the one presented in Subsection 2.3.1, has been utilized to control the rigid body motions of the first and third joints of the spherical robotic manipulator (see Figs. 3-1 and 3-2). The controller is based on a reduced order model, which only accounts for the rigid body degrees of freedom of the system. The reduced order model is obtained from Eq. (3-14) by ignoring all terms and equations pertaining to the flexible motion of the third link. The resulting equations can be written in the following compact form

$$\dot{\underset{\sim}{x}}_r^R = \underset{\sim}{f}_r^R\left(\underset{\sim}{x}_r^R\right) + B_r^R\left(\underset{\sim}{x}_r^R\right)\underset{\sim}{u}_c \tag{3-28}$$

where $\underset{\sim}{x}_r^R = \left[\theta_1, r, \dot{\theta}_1, \dot{r}\right]^T$, $\underset{\sim}{f}_r^R = \left[x_{r_3}^R, x_{r_4}^R, f_{r_3}^R, f_{r_4}^R\right]^T$, and $B_r^R = \begin{bmatrix} 0 & 0 & b_{r_1}^R & 0 \\ 0 & 0 & 0 & b_{r_2}^R \end{bmatrix}^T$.

Both $\underset{\sim}{f}_r^R$ and B_r^R are not considered to be fully known. Therefore, the controller was designed based on the following nominal model:

$$\dot{\hat{\underset{\sim}{x}}}_r^R = \hat{\underset{\sim}{f}}_r^R\left(\hat{\underset{\sim}{x}}_r^R\right) + \hat{B}_r^R\left(\hat{\underset{\sim}{x}}_r^R\right)\underset{\sim}{u}_c \tag{3-29}$$

where the upper bounds $F_i^R = \left| f_{r_i}^R - \hat{f}_{r_i}^R \right|_{\text{sup}}$ for $i = 3, 4$ are assumed to be known. In addition, the $b_{r_i}^R$ terms for $i = 1, 2$ are considered to satisfy the following constraints (Slotine and Li, 1991)

$$\hat{b}_{r_i}^R = \sqrt{\left(b_{r_i}^R\right)_{\min}\left(b_{r_i}^R\right)_{\max}} \quad \text{and} \quad \beta_i = \sqrt{\frac{\left(b_{r_i}^R\right)_{\max}}{\left(b_{r_i}^R\right)_{\min}}} \quad \text{for} \quad i = 1, 2 \tag{3-30}$$

By defining the error vector to be $\tilde{\underset{\sim}{x}}_r^R = \underset{\sim}{x}_r^R - \underset{\sim}{x}_{r_d}^R$, the sliding surfaces can be selected as follows

$$s_{C_i} = \tilde{x}_{r_{i+2}}^R + \lambda_i \tilde{x}_{r_i}^R \quad \text{for} \quad i = 1, 2 \tag{3-31}$$

The control signals for the revolute and prismatic joints are given by

$$u_{C_i} = u_{C_i}^{eq} - \frac{K_{C_i}}{\hat{b}_{r_i}^R}\operatorname{sgn}\left(s_{C_i}\right) \quad \text{for} \quad i = 1, 2 \tag{3-32}$$

The $u_{C_i}^{eq}$ terms are determined by setting $\dot{s}_{C_i} = 0$ for $i = 1, 2$. The K_{C_i} gains are computed by satisfying the sliding conditions, which yields

$$k_{C_i} \geq \beta_i \left[F_{i+2}^{R} + \eta_{C_i} \right] + \left| \beta_i - 1 \right| \left| \hat{f}_{r_{i+2}}^{R} + \lambda_i \, \tilde{x}_{r_{i+2}}^{R} - \ddot{x}_{r_{i_d}}^{R} \right| \qquad \text{for} \quad i = 1, 2 \tag{3-33}$$

Once again, in order to minimize the chattering effect, the $\operatorname{sgn}\left(s_{C_i}\right)$ terms are replaced by their respective saturation terms $\operatorname{sat}\left(\dfrac{s_{C_i}}{\phi_{C_i}}\right)$.

3.5 Simulation Results

The focus of the digital simulations is to assess the performances of both self-tuning observer and sliding mode observer in estimating the state variables of structures with configuration-dependent natural frequencies. The geometric dimensions and material properties of the arm along with the observer parameters are listed in Tables 3-1 and 3-2, respectively. All simulation results have been generated based on the full-order model of the robot that is given in Eq. (3-14) while keeping a constant payload mass of $0.083 \, \mathrm{Kg}$. Two data sets were generated for each observer. In the first one, the controller was turned off and the third link was fully protruded. The following initial conditions were specified to excite both elastic modes of the out-of-plane transverse deformation of the flexible link:

$$\begin{aligned} \underset{\sim}{x}^{T}(0) &= \left[\theta_1, r, q_1, q_2, q_3, q_4, \dot{\theta}_1, \dot{r}, \dot{q}_1, \dot{q}_2, \dot{q}_3, \dot{q}_4 \right]_{t=0} \\ &= \left[0, 0.45, 0.02, -0.005, 0, 0, 0, 0, 0, 0, 0, 0 \right] \end{aligned} \tag{3-34}$$

The nonzero values specified for $q_1(0)$ and $q_2(0)$ induces the ensuing out-of-plane transverse vibrations of the flexible link for $t > 0$. The initial conditions of the state observers were selected to be:

$$\underset{\sim}{\hat{x}}_r^T(0) = \left[q_{1_e}, q_{2_e}, q_{3_e}, q_{4_e}, \dot{q}_{1_e}, \dot{q}_{2_e}, \dot{q}_{3_e}, \dot{q}_{4_e} \right]_{t=0} = \underset{\sim}{0}_{1\times 8} \tag{3-35}$$

Equation (3-15) was then used to extract $q_{1_m}(t)$ and $q_{2_m}(t)$ from the strain gauge signal. The accuracy of $q_{1_m}(t)$ and $q_{2_m}(t)$ in representing the actual $q_1(t)$ and $q_2(t)$ can easily be performed since all the $q_i(t)$ terms and their time derivatives are readily available from the simulation results. Figure 3-3 and 3-4 prove the viability of Eq. (3-15) through the accurate predictions of $q_1(t)$ and $q_2(t)$ by $q_{1_m}(t)$ and $q_{2_m}(t)$, respectively. Figures 3-5 to 3-8 illustrate $q_{1_m}(t), q_{2_m}(t), \dot{q}_{1_m}(t), \dot{q}_{2_m}(t)$ and their estimated $q_{1_e}(t), q_{2_e}(t), \dot{q}_{1_e}(t), \dot{q}_{2_e}(t)$ plots by the self-tuning observer. The estimated variables are shown to quickly converge to the actual generalized coordinates of the flexible motion of the third link. The plots serve to demonstrate the robust performance of the self-tuning observer in spite of the fact that all $\hat{f}_{r_i}$ for $i = 5, \cdots, 8$ have been set to zero (see Table 3-2).

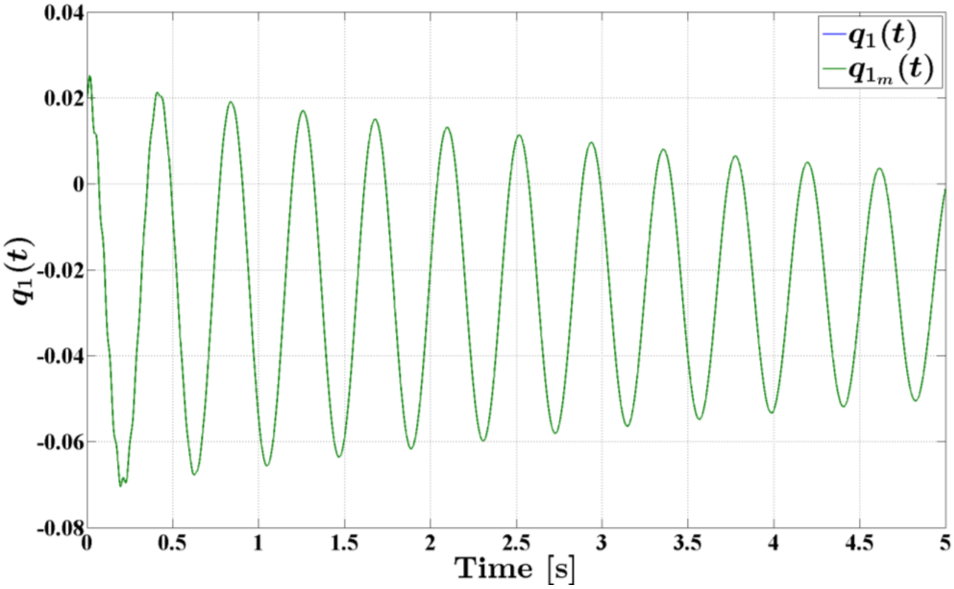

Fig. 3-3. Simulation results for $q_1(t)$ and $q_{1_m}(t)$ induced by disturbances in the initial conditions

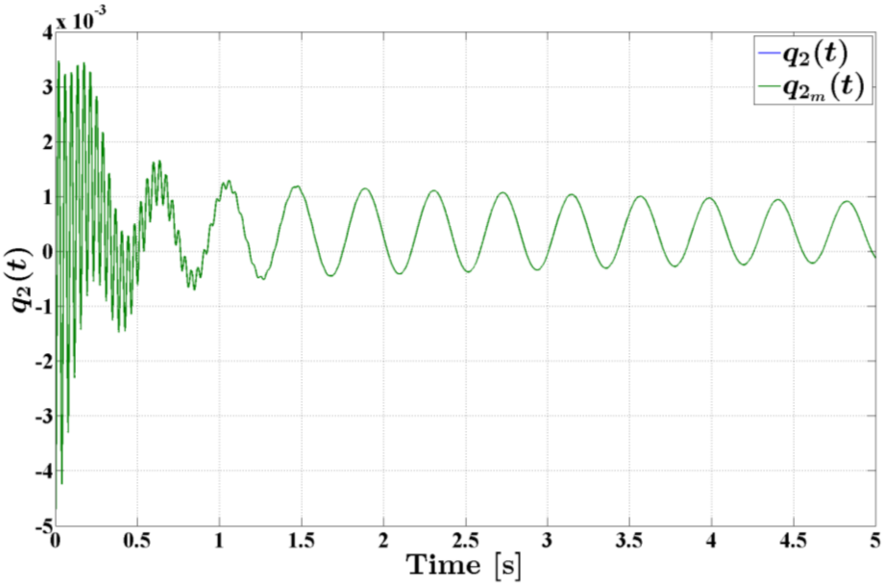

Fig. 3-4. Simulation results for $q_2(t)$ and $q_{2_m}(t)$ induced by disturbances in the initial conditions

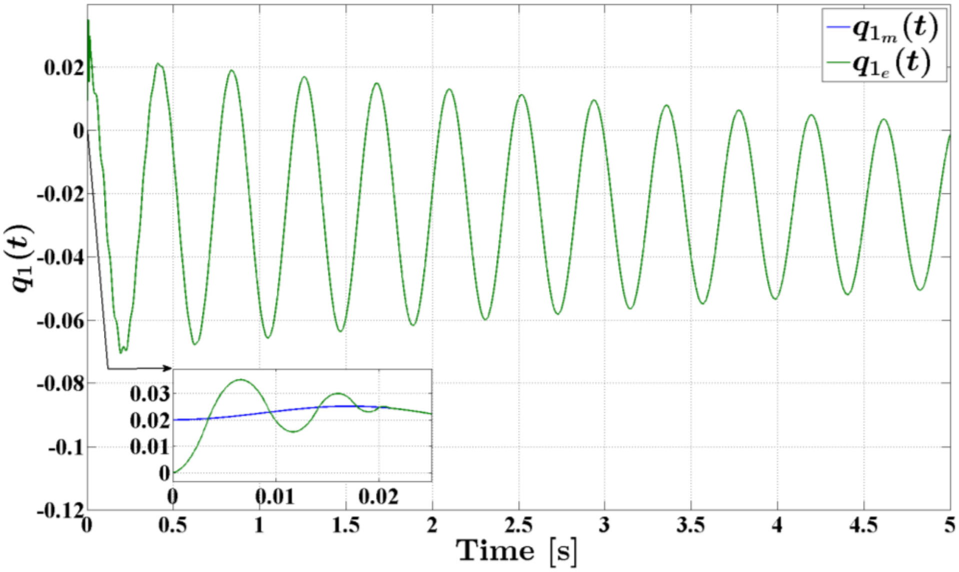

Fig. 3-5. Simulation results for $q_{1_m}(t)$ and $q_{1_e}(t)$ induced by disturbances in the initial conditions

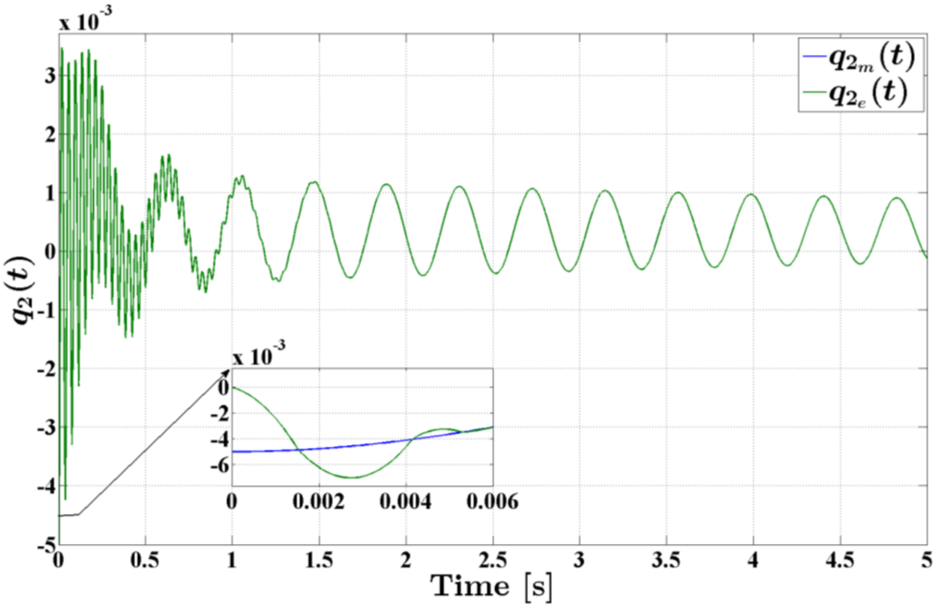

Fig. 3-6. Simulation results for $q_{2_m}(t)$ and $q_{2_e}(t)$ induced by disturbances in the initial conditions

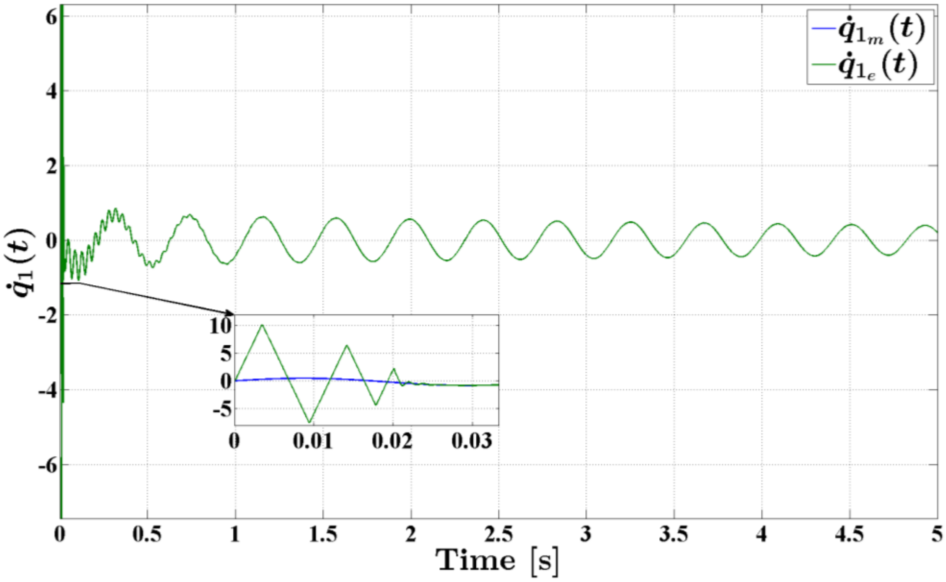

Fig. 3-7. Simulation results for $\dot{q}_{1_m}(t)$ and $\dot{q}_{1_e}(t)$ induced by disturbances in the initial conditions

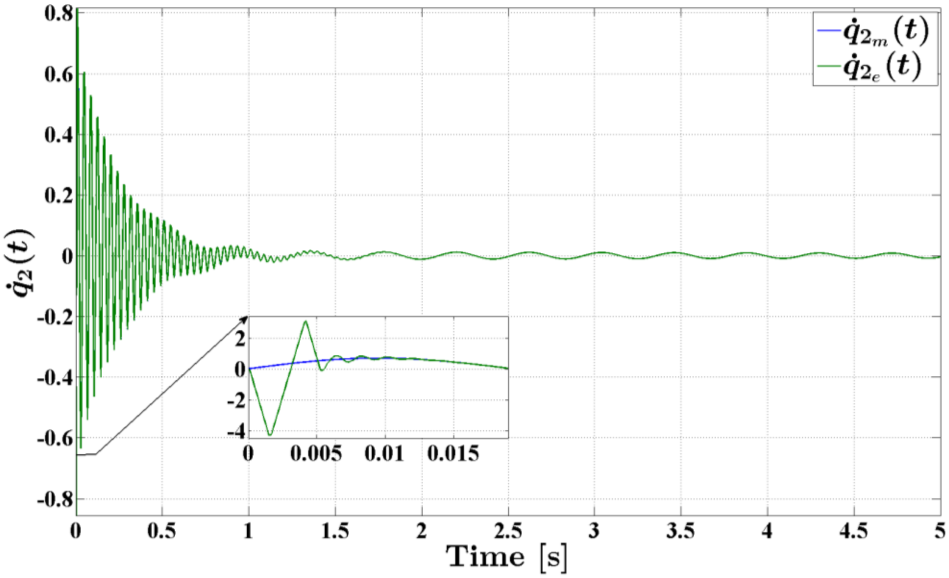

Fig. 3-8. Simulation results for $\dot{q}_{2_m}(t)$ and $\dot{q}_{2_e}(t)$ induced by disturbances in the initial conditions

Robot Arm Data	
Gravitational acceleration, g	$9.81\ \mathrm{m.s}^{-2}$
Length of the 2nd link, L_2	$0.58\ \mathrm{m}$
Length of the 3rd link, L_3	$0.93\ \mathrm{m}$
Radius of the cross sectional area of the 3rd link, R_3	$0.003175\ \mathrm{m}$
Maximum protruded length of the 3rd link, $2r_{\max}$	$0.9\ \mathrm{m}$
Material Properties	
Young's Modulus of elasticity, E	$68.95\ \mathrm{GPa}$
Aluminum density, ρ	$2712.68\ \mathrm{m}^3.\mathrm{Kg}^{-1}$
Mass of the 2nd link, m_2	$9.424\ \mathrm{Kg}$
Payload Mass, m_p	$0.083\ \mathrm{Kg}$
Structural damping coefficient, $c_{33}, c_{44}, c_{55}, c_{66}$	$0.1, 1, 0.1, 1\ \mathrm{N.s}$

Table 3-1. Robotic manipulator data and material properties

STO Parameters	
$\eta_j \quad j = 1, \cdots, 4$	1
$\hat{f}_{r_i} \quad i = 5, \cdots, 8$	0
$\lvert\tilde{x}_i\rvert_{upper\ bound} \quad i = 5, \cdots, 8$	0.001
$F_i \quad i = 5, \cdots, 8$	1000
$\phi_i \quad i = 1, \cdots, 4$	0.0001

Table 3-2. Self tuning observer parameters

SMO Parameters	
$\eta_j \quad j = 1, \cdots, 4$	5
$\hat{f}_{r_i} \quad i = 5, \cdots, 8$	0
$\lvert\tilde{x}_i\rvert_{upper\ bound} \quad i = 5, \cdots, 8$	0.01
$\lvert\tilde{x}_i\rvert_{desired\_accuracy} \quad i = 5, \cdots, 8$	0.01
$F_i \quad i = 5, \cdots, 8$	30
$\phi_i \quad i = 1, \cdots, 4$	0.001

Table 3-3. Sliding mode observer parameters

The SMO results, shown in Figs. 3-9 to 3-12, have been generated under the same conditions as those used to obtain their STO counterparts in Figs. 3-5 to 3-8. The results demonstrate the SMO robustness through the rapid convergence of the estimated variables to the actual ones. This occurred in spite of setting all $\hat{f}_{r_i}$ for $i = 5, \cdots, 8$ to zero as shown in Table 3-3.

The second set of data has been generated by using the SMC to maneuver the end-effector along a straight line in the work envelope of the robot from point $\mathrm{A}\,(1.19, 0, 0)$ to $\mathrm{B}\,(1.19, 0.879, 0)$ then $\mathrm{C}\,(1.19, -0.879, 0)$ and back to A (see Fig. 3-13). Note that all coordinates are given in meters and defined with respect to the inertial coordinate system $\{x_0, y_0, z_0\}$. At points B and C, the third link is fully protruded from the second link causing the length of its flexible portion to be at its maximum value of $0.9\ \mathrm{m}$. This has a softening effect on the flexible link, which causes its first two natural frequencies to decrease to $2.38\ \mathrm{Hz}$ and $25.96\ \mathrm{Hz}$. However, at point A, the third link is fully retracted with the length of the flexible link being $0.61\ \mathrm{m}$. This has a tendency to stiffen the deformable portion of the third link; thus, causing its first two natural frequencies to increase to $4.4\ \mathrm{Hz}$ and $55.78\ \mathrm{Hz}$. Therefore, the prescribed manoeuvre will allow the assessment of the observer performance in the presence of significant variations in the natural frequencies of the system.

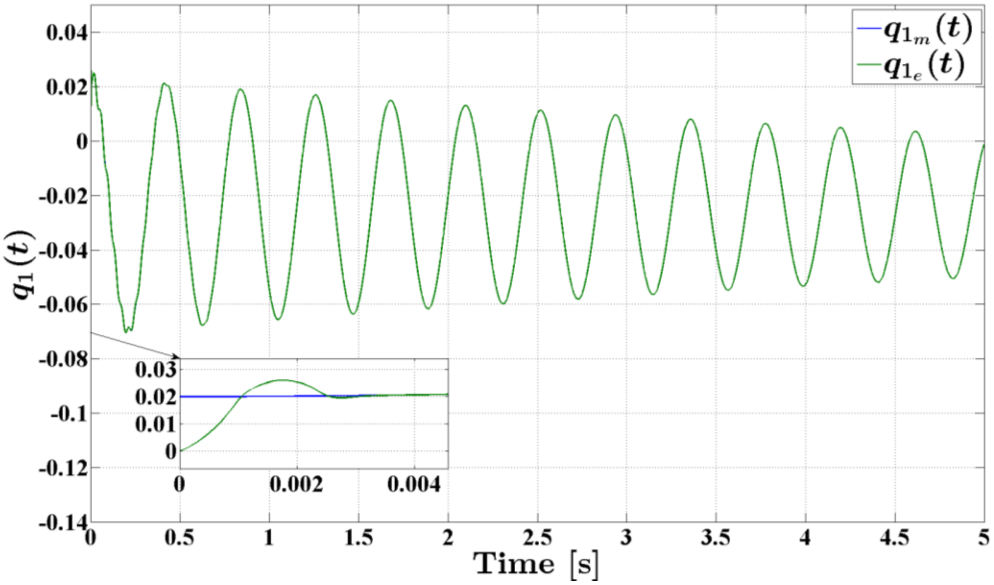

Fig. 3-9. Simulation results for $q_{1_m}(t)$ and $q_{1_e}(t)$ induced by disturbances in the initial conditions

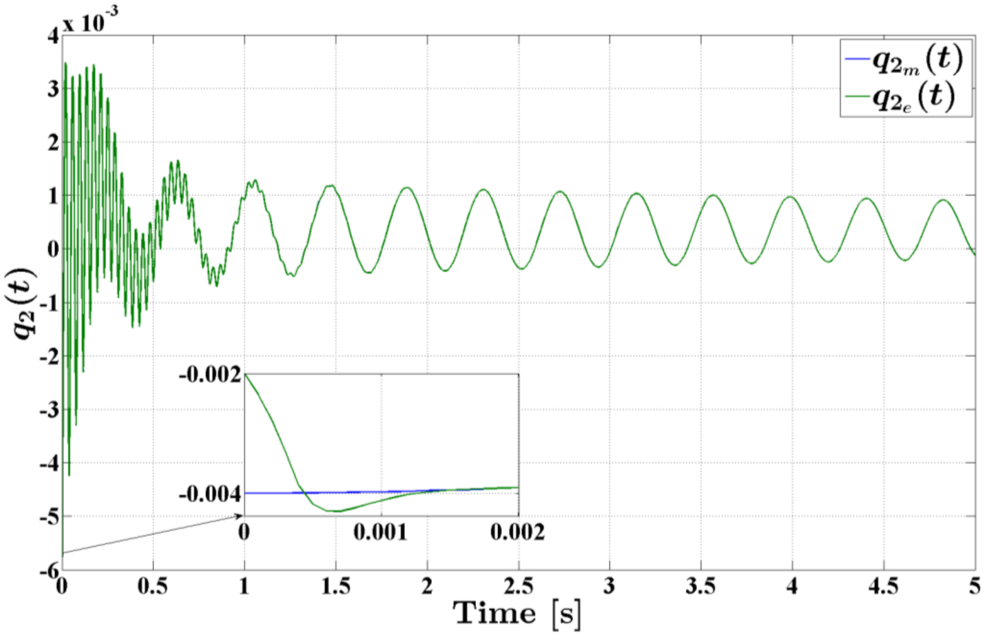

Fig. 3-10. Simulation results for $q_{2_m}(t)$ and $q_{2_e}(t)$ induced by disturbances in the initial conditions

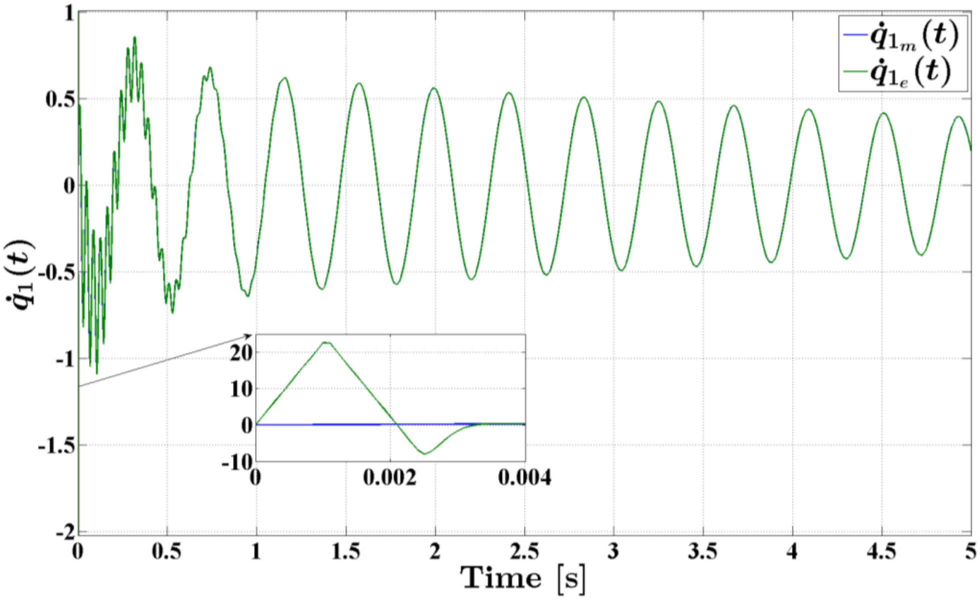

Fig. 3-11. Simulation results for $\dot{q}_{1_m}(t)$ and $\dot{q}_{1_e}(t)$ induced by disturbances in the initial conditions

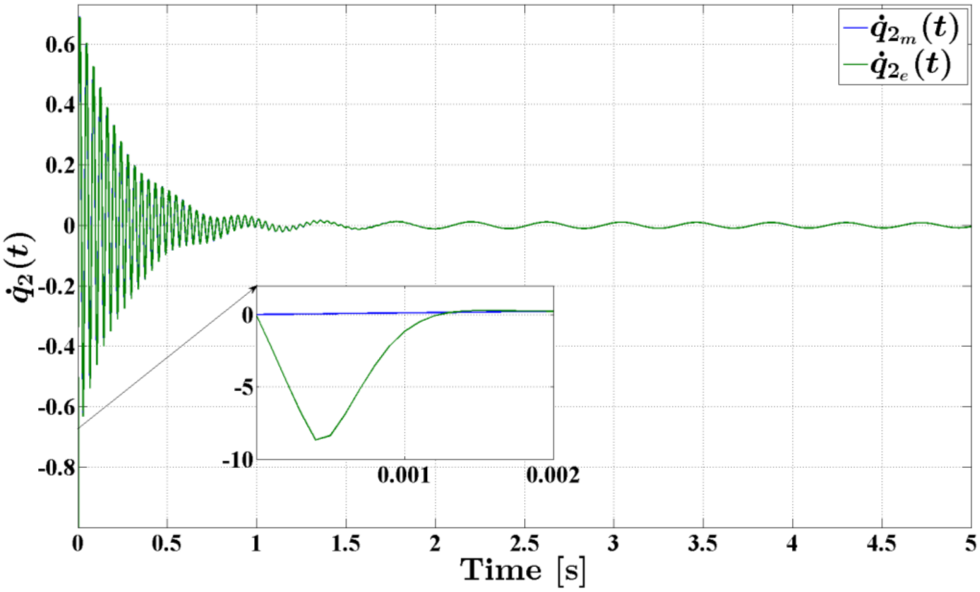

Fig. 3-12. Simulation results for $\dot{q}_{2_m}(t)$ and $\dot{q}_{2_e}(t)$ induced by disturbances in the initial conditions

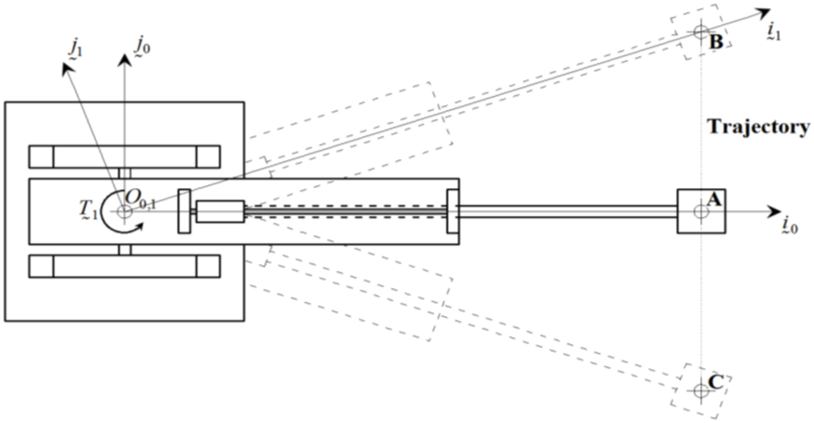

Fig. 3-13. Prescribed maneuver of the end-effector

The inverse kinematic problem of the spherical robot arm (Wolovich, 1987) was implemented to determine the desired joint trajectories $\theta_{1_d}(t)$ and $r_d(t)$ corresponding to the prescribed maneuver of the end-effector (see Figs. 3-14 and 3-15). The rigid body SMC, whose parameters are listed in Table 3-4, was used to ensure that both $\theta_1(t)$ and $r(t)$ accurately track their desired values. The initial conditions of the arm were defined to be:

$$\underset{\sim}{x}^T(0) = \left[9.4^\circ, 0.315, 0.02, 0, 0, 0, 0, 0, 0, 0, 0, 0\right] \tag{3-36}$$

Note that the out-of-plane transverse deformation of the protruding portion of the third link was excited by setting $q_1(0) \neq 0$. The initial conditions of the observers were kept the same as in Eq. (3-35). Figures 3-14 and 3-15 demonstrate the good tracking characteristic of the SMC in controlling the rigid body degrees of freedom of the system. The STO estimates of $q_{1_e}(t), q_{3_e}(t), \dot{q}_{1_e}(t)$, and $\dot{q}_{3_e}(t)$ are shown in Figs. 3-16 to 3-19 to quickly converge and accurately estimate $q_{1_m}(t), q_{3_m}(t), \dot{q}_{1_m}(t)$, and $\dot{q}_{3_m}(t)$; thus, demonstrating the robust capability of the observer in yielding accurate estimation of the state variables in spite of significant modeling imprecision and initial impulsive perturbations. Furthermore, Figs. 3-16 to 3-19 clearly reveal significant fluctuations in the natural frequencies of the flexible portion of the third link as the end-effector goes through the specified maneuver. Moreover, Fig. 3-16 exhibits a significant increase in the sagging of the beam as the end-effector moves from A to B or C. Note that the results of the second elastic modes are not shown here due to the limited bandwidths of the joint actuators, which were not high enough to excite the second and higher elastic modes. The SMO estimates for $q_{1_e}(t), q_{3_e}(t), \dot{q}_{1_e}(t),$ and $\dot{q}_{3_e}(t)$ are shown in Figs. 3-20 to 3-23. They reveal the robustness and rapid convergence of the estimated variables to the actual ones; thus, proving the capability of the SMO in yielding accurate estimation of the state variables despite the presence of significant structured and unstructured uncertainties.

SMC Parameters Used in Simulations	
$\hat{f}_{r_3}^{R},\ \hat{f}_{r_4}^{R}$	$0\ \mathrm{rad.s^{-2}},\ 0\ \mathrm{m.s^{-2}}$
$F_3^{R},\ F_4^{R}$	$200\ \mathrm{rad.s^{-2}},\ 50\ \mathrm{m.s^{-2}}$
$\left(b_{r_1}^{R}\right)_{\min},\left(b_{r_2}^{R}\right)_{\min}$	$1, 1$
$\left(b_{r_1}^{R}\right)_{\max},\left(b_{r_2}^{R}\right)_{\max}$	$10, 10$
λ_1, λ_2	$10, 10$
ϕ_{C_1}, ϕ_{C_2}	$0.001, 0.001$
η_{C_1}, η_{C_2}	$10, 10$

Table 3-4. Simulation sliding mode controller parameters

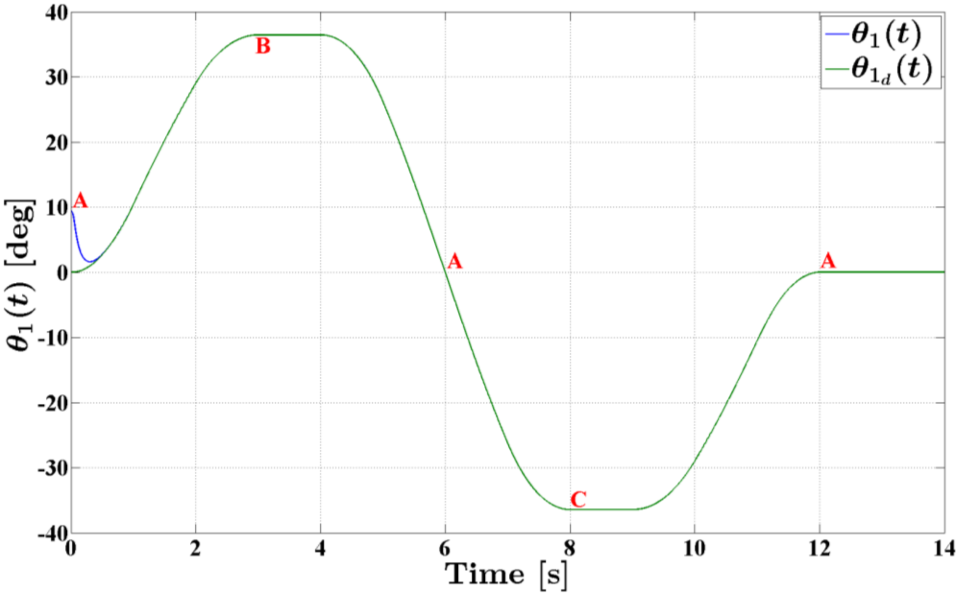

Fig. 3-14. Simulation results for $\theta_{1_d}(t)$ and $\theta_1(t)$ during the tracking maneuver

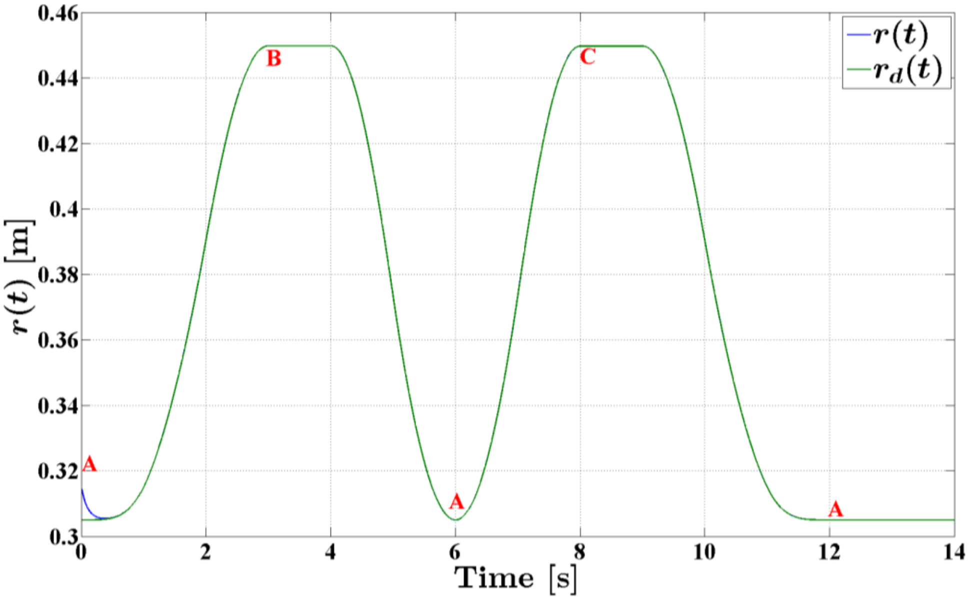

Fig. 3-15. Simulation results for $r_d(t)$ and $r(t)$ during the tracking maneuver

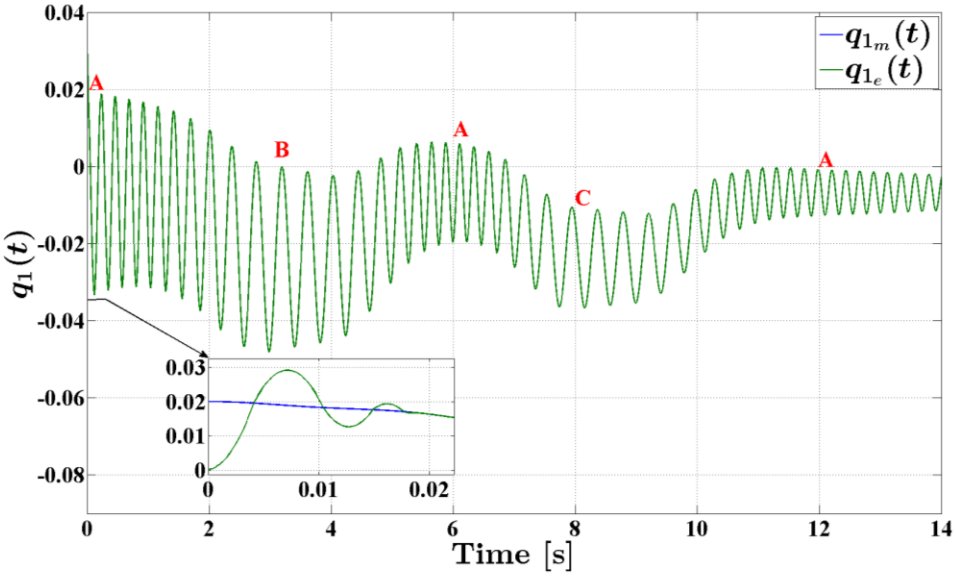

Fig. 3-16. Simulation results for $q_{1_m}(t)$ and $q_{1_e}(t)$ during the tracking maneuver

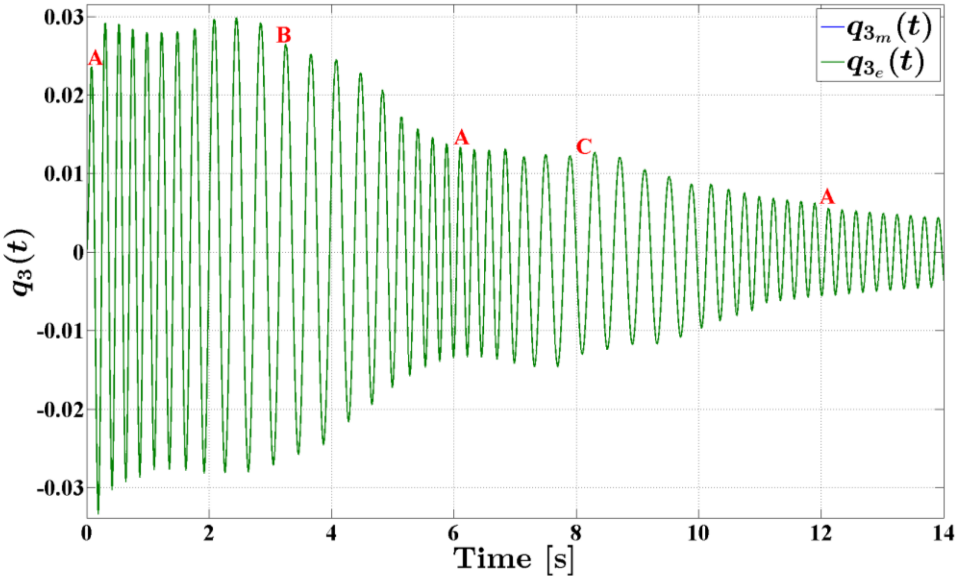

Fig. 3-17. Simulation results for $q_{3_m}(t)$ and $q_{3_e}(t)$ during the tracking maneuver

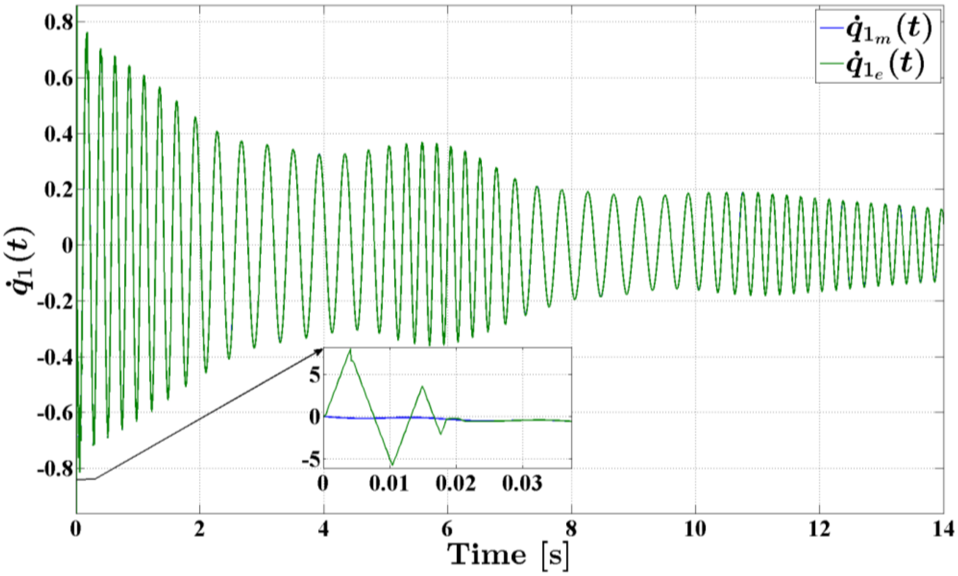

Fig. 3-18. Simulation results for $\dot{q}_{1_m}(t)$ and $\dot{q}_{1_e}(t)$ during the tracking maneuver

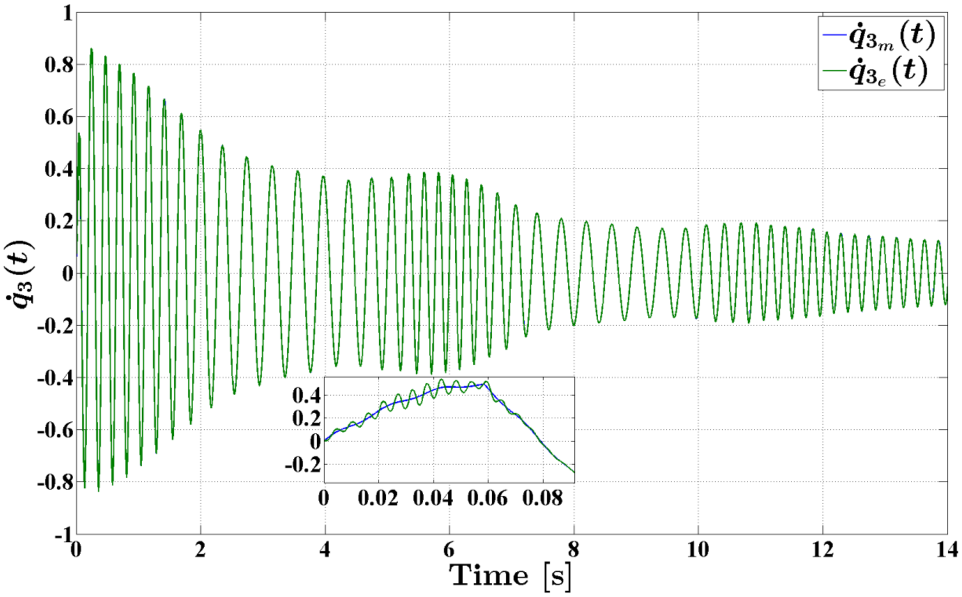

Fig. 3-19. Simulation results for $\dot{q}_{3_m}(t)$ and $\dot{q}_{3_e}(t)$ during the tracking maneuver

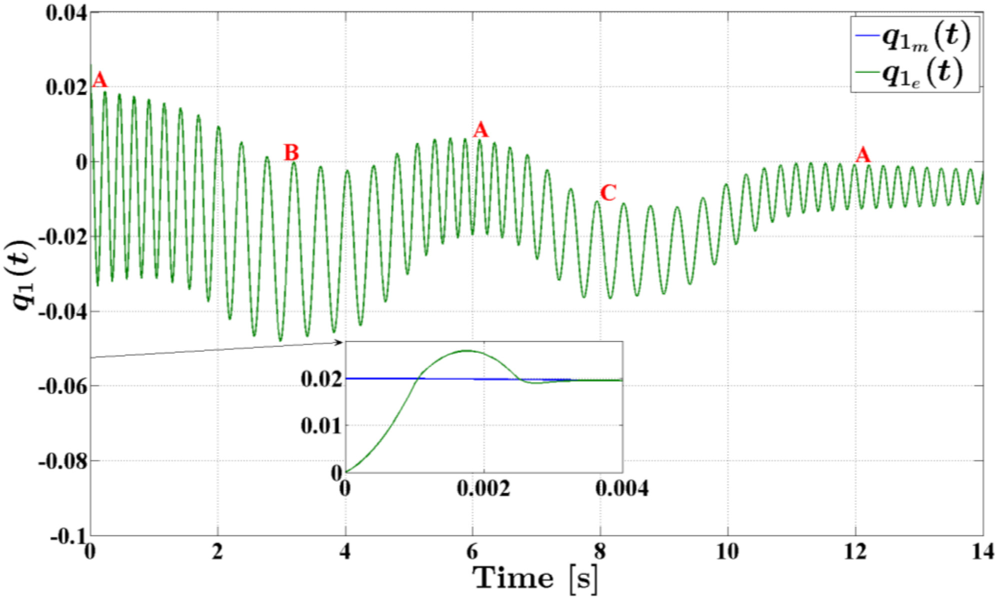

Fig. 3-20 Simulation results for $q_{1_m}(t)$ and $q_{1_e}(t)$ during the tracking maneuver

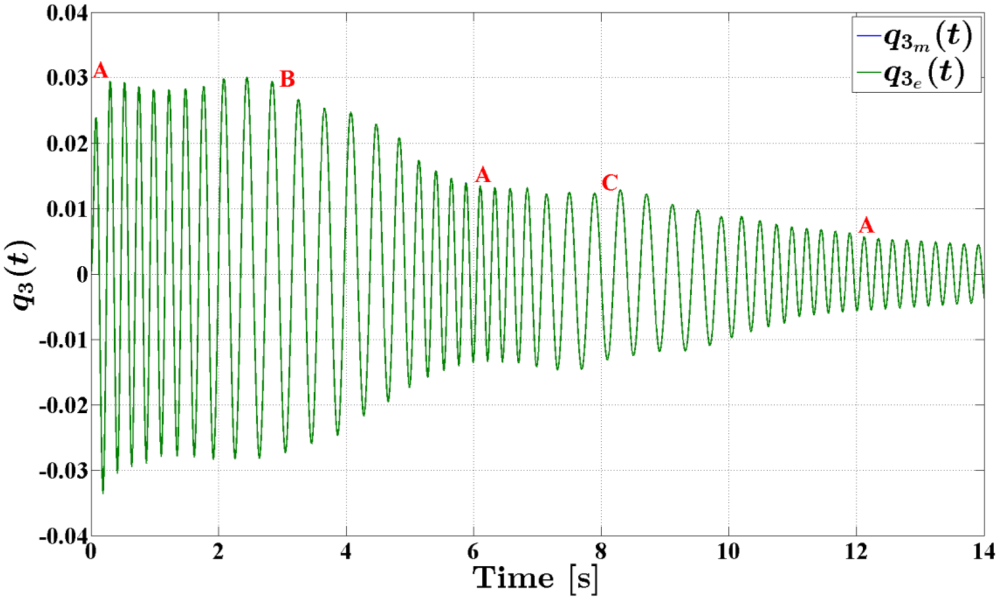

Fig. 3-21. Simulation results for $q_{3_m}(t)$ and $q_{3_e}(t)$ during the tracking maneuver

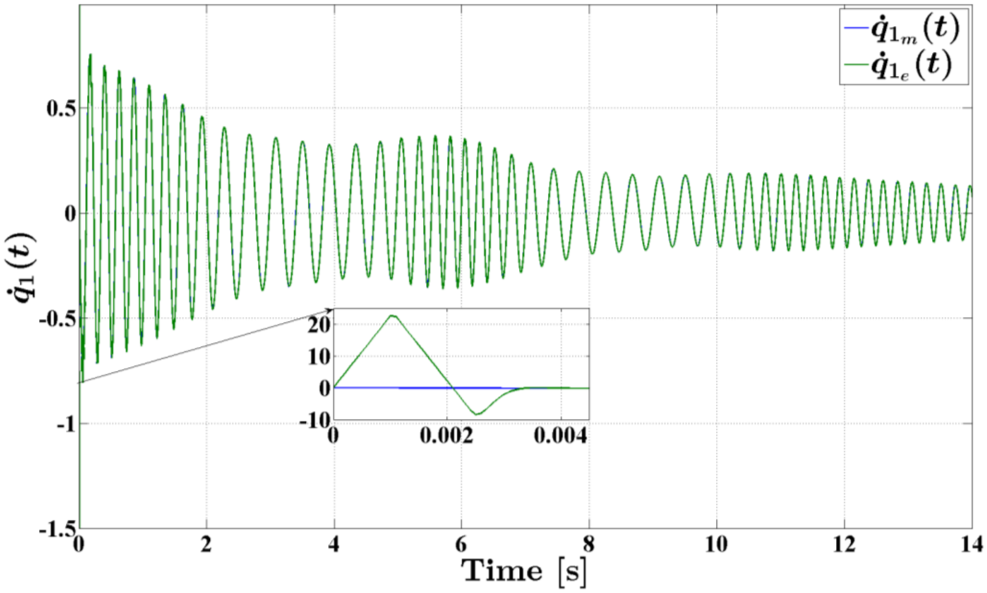

Fig. 3-22. Simulation results for $\dot{q}_{1_m}(t)$ and $\dot{q}_{1_e}(t)$ during the tracking maneuver

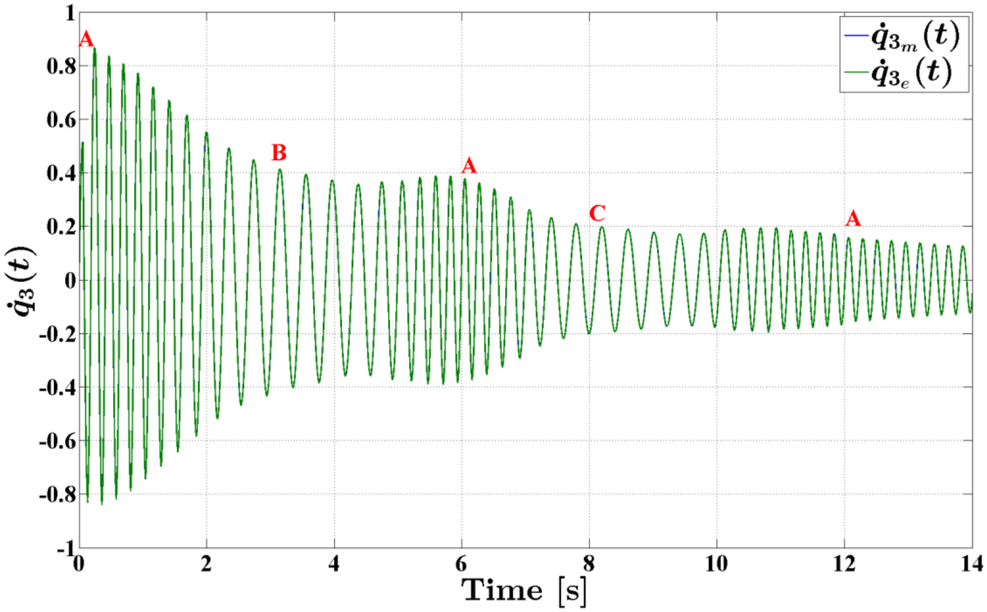

Fig. 3-23. Simulation results for $\dot{q}_{3_m}(t)$ and $\dot{q}_{3_e}(t)$ during the tracking maneuver

3.6 Experimental Setup

The experimental set-up consists of a spherical robot arm as depicted in Figs. 3-1 and 3-2. Its geometric dimensions and material properties are listed in

Table 3-1. The first two links are connected to revolute joints, which are driven by DC servo-motors (PMI S6M4HI) through harmonic drives with a gearhead reduction ratio of 60:1. Note that the second link has been deactivated in the current work and considered to be a pure inertia loading on the first link. The first joint allows the arm to rotate around $\underset{\sim}{k}_1$. Using an incremental optical encoder mounted at the motor's shaft, the angular displacement of the first link is measured. The optical encoder along with the gearhead enables the measurement of θ_1 with a resolution of 0.03 degree/pulse. The third link is connected to a prismatic joint and driven by a DC servo-motor (MicroMo 3557) through a ball bearing screw with a $5\,\mathrm{mm}$ pitch. This arrangement allows axial motion of the third link along the direction of $\underset{\sim}{k}_2$. A second incremental optical encoder, mounted on the MicroMo shaft, along with the ball bearing screw allows a displacement measurement of the axial motion of the third link with a resolution of 7.4074 micron/pulse. The pulses of the optical encoders are counted by two 24-bit Up/Down counters that are housed in the dSPACE DS3001 module.

The in-plane and out-of-plane transverse deformations of the protruding portion of the third link are measured by using two Measurement Group CEA-06-125UR-350 strain gauges that are mounted at a distance L_{SG} from the point where the leadcrew nut is connected to the third link (see Fig. 3-1). The outputs of the strain gauges are passed through a low-pass fourth-order Butterworth filter with a cut-off frequency of $40\,\mathrm{Hz}$ to attenuate the noise and the contributions of the third and higher elastic modes.

The block diagram of the experimental set-up is shown in Fig. 3-24. It reveals that the real-time controller and observer are implemented through the dSPACE DS1005 module. Moreover, the analog feedback signals of the strain gauges and the digital control input signals are handled at the interface between the micro-processor and the robot arm by 16-bit analog-to-digital (ADC) and digital-to-analog (DAC) converters that are housed in dSPACE DS2002 and DS2101 modules, respectively.

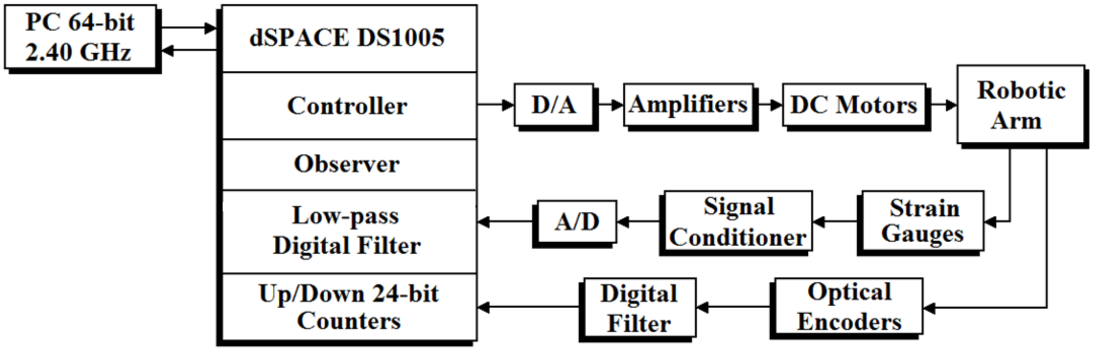

Fig. 3-24. Block diagram of the experimental apparatus

3.7 Experimental Results

To experimentally validate the performance of the self-tuning observer, the same tests that were conducted to generate the simulation results have been repeated using the set-up depicted in Figs. 3-2 and 3-24. Moreover, the observer parameters were assigned the same values as those used in generating the numerical results (see Tables 3-2 and 3-3). The payload mass was also kept constant at $0.083\,\mathrm{Kg}$.

During the first test, the controller was deactivated and the third link was fully protruded from the second link. The initial conditions of both observers are given in Eq. (3-35); whereas, the initial conditions of the arm were defined as

$$\underset{\sim}{x}^T(0) = [0, 0.45, -0.0238, 0.00046, 0, 0, 0, 0, 0, 0, 0, 0] \tag{3-37}$$

Note that the nonzero values of $q_1(0)$ and $q_2(0)$ are determined by computing the static deformation of the flexible link. A vertical impulsive force, which has a wide frequency spectrum, was applied at the end-effector to excite the two elastic modes of the out-of-plane transverse deformation of the protruding portion of the third link. Once again, Eq. (3-15) has been implemented to extract $q_{1_m}(t)$ and $q_{2_m}(t)$ from the strain gauge signal. The STO results for $q_{1_e}(t)$ and $q_{2_e}(t)$ are shown in Figs. 3-25 and 3-26 to quickly converge and accurately estimate $q_{1_m}(t)$ and $q_{2_m}(t)$. The experimental data exhibit the same estimation pattern as the one observed in the numerical results. The plots validate the robustness of the self-tuning observer in producing state variables that quickly converged to the actual ones in spite of setting all $\hat{f}_{r_i}$ for $i = 5, \cdots, 8$ in the nominal model to zero (see Table 3-2).

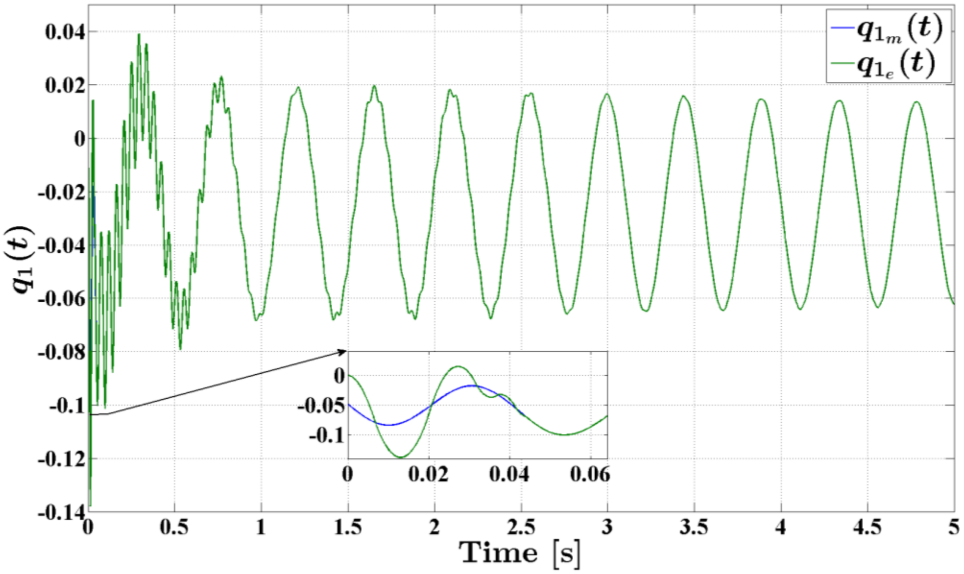

Fig. 3-25. Experimental results for $q_{1_m}(t)$ and $q_{1_e}(t)$ induced by an initial impulsive force

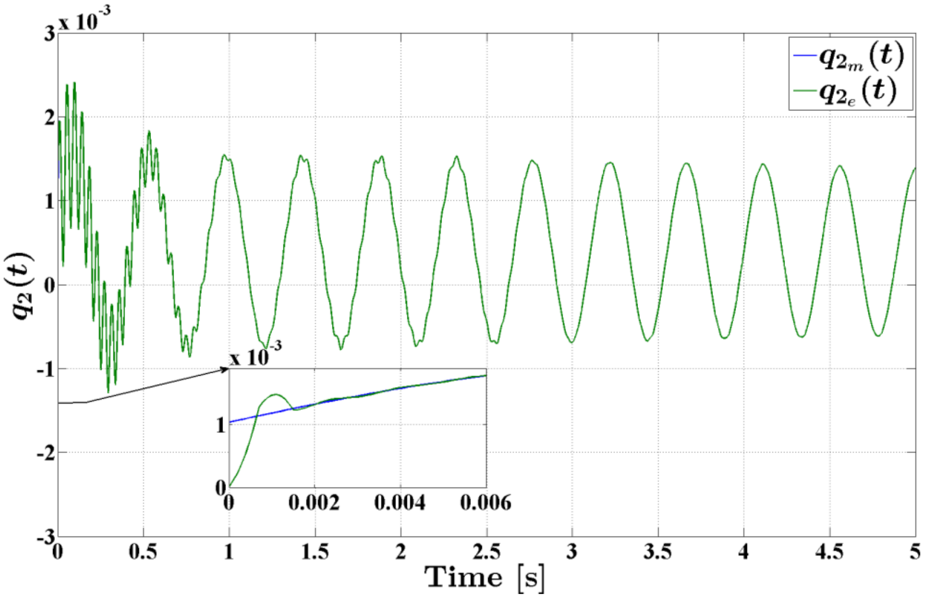

Fig. 3-26. Experimental results for $q_{2_m}(t)$ and $q_{2_e}(t)$ induced by an initial impulsive force

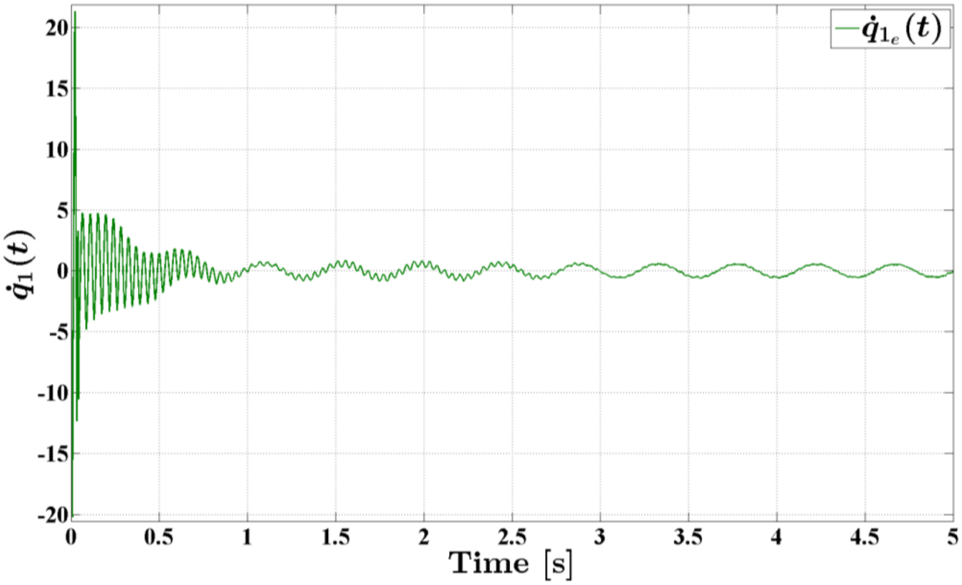

Fig. 3-27. Experimental result for $\dot{q}_{1_e}(t)$ induced by an initial impulsive force

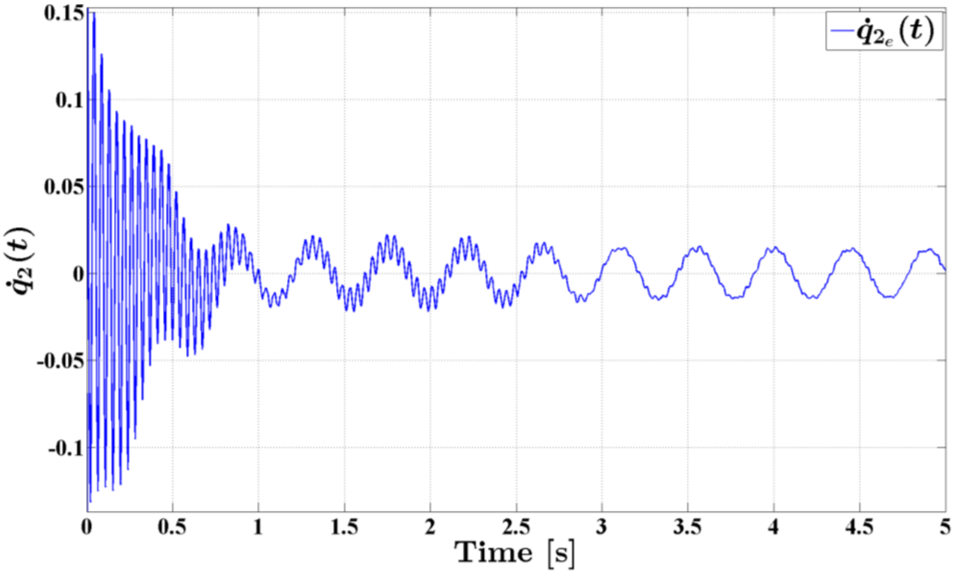

Fig. 3-28. Experimental result for $\dot{q}_{2_e}(t)$ induced by an initial impulsive force

Since no data is available to confirm the accuracy of the experimental results in Figs. 3-27 and 3-28 then both $\dot{q}_{1_e}(t)$ and $\dot{q}_{2_e}(t)$ have been integrated with respect to time and compared to $q_{1_m}(t)$ and $q_{2_m}(t)$. Figures 3-29 and 3-30 confirm that $q_{1_m}(t)$ and $q_{2_m}(t)$ can be reconstructed by integrating the estimated $\dot{q}_{1_e}(t)$ and $\dot{q}_{2_e}(t)$, respectively; thus, validating their accuracy.

The SMO results for $q_{1_e}(t)$ and $q_{2_e}(t)$ are shown in Figs. 3-31 and 3-32. They accurately estimate $q_{1_m}(t)$ and $q_{2_m}(t)$ and exhibit similar pattern to the one observed in the respective numerical results. The plots prove the robustness of the SMO in yielding accurate estimate of the state variables in spite of setting all $\hat{f}_{r_i}$ for $i = 5, \cdots, 8$ to zero (see Table 3-3). Once again, the $\dot{q}_{1_e}(t)$ and $\dot{q}_{2_e}(t)$ results in Figs. 3-33 and 3-34 are integrated with respect to time and compared to $q_{1_m}(t)$ and $q_{2_m}(t)$. Figures 3-35 and 3-36 confirm that $q_{1_m}(t)$ and $q_{2_m}(t)$ can be reconstructed by integrating the estimated $\dot{q}_{1_e}(t)$ and $\dot{q}_{2_e}(t)$, respectively; thus, validating their accuracy.

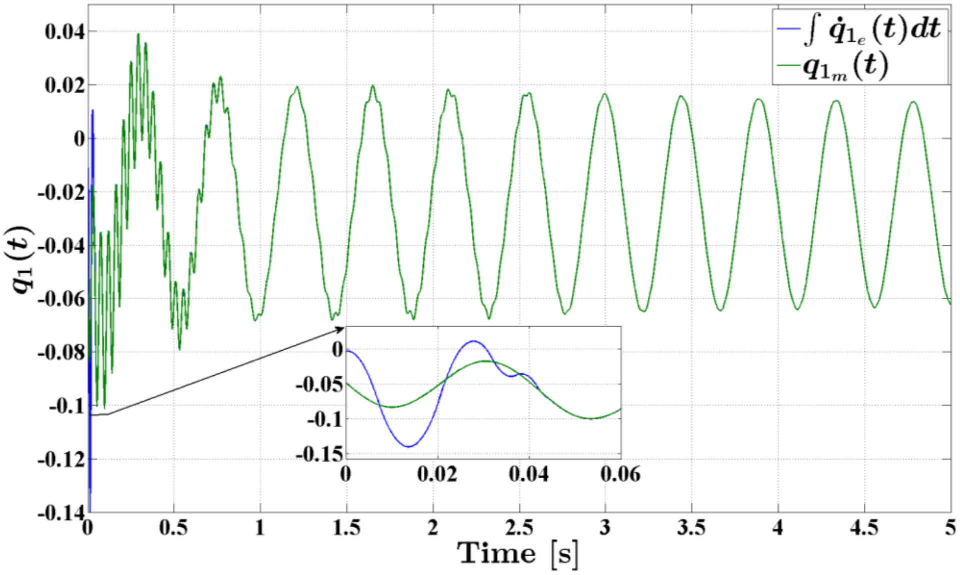

Fig. 3-29. Experimental results comparing $\int \dot{q}_{1_e} dt$ to q_{1_m}

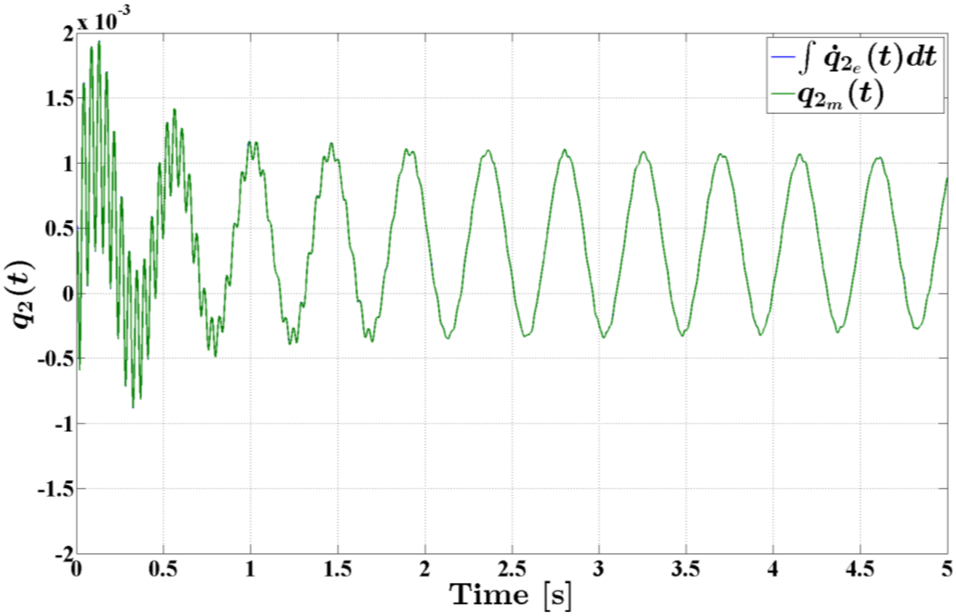

Fig. 3-30. Experimental results comparing $\int \dot{q}_{2_e} dt$ to q_{2_m}

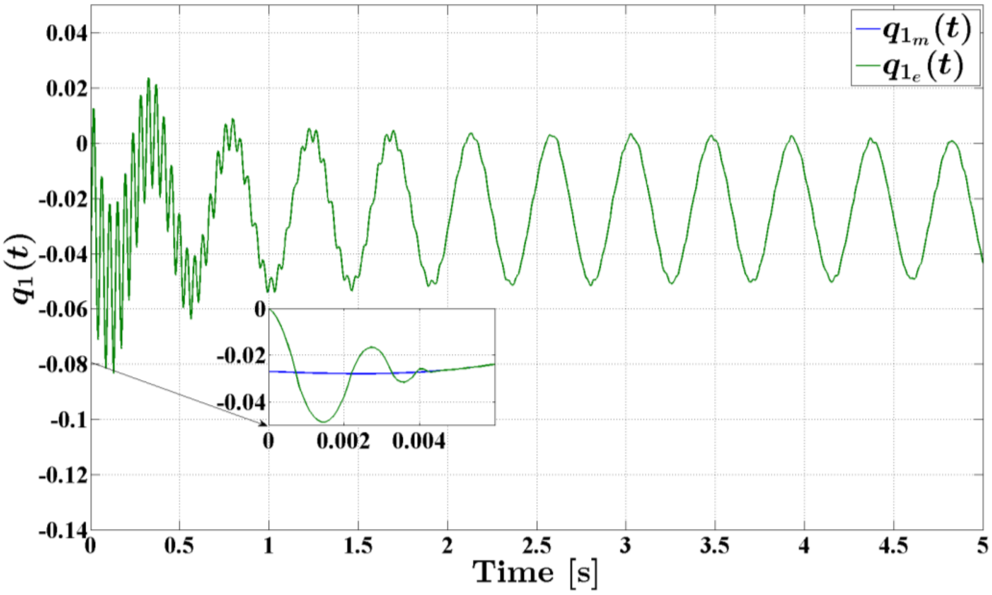

Fig. 3-31. Experimental results for $q_{1_m}(t)$ and $q_{1_e}(t)$ induced by an initial impulsive force

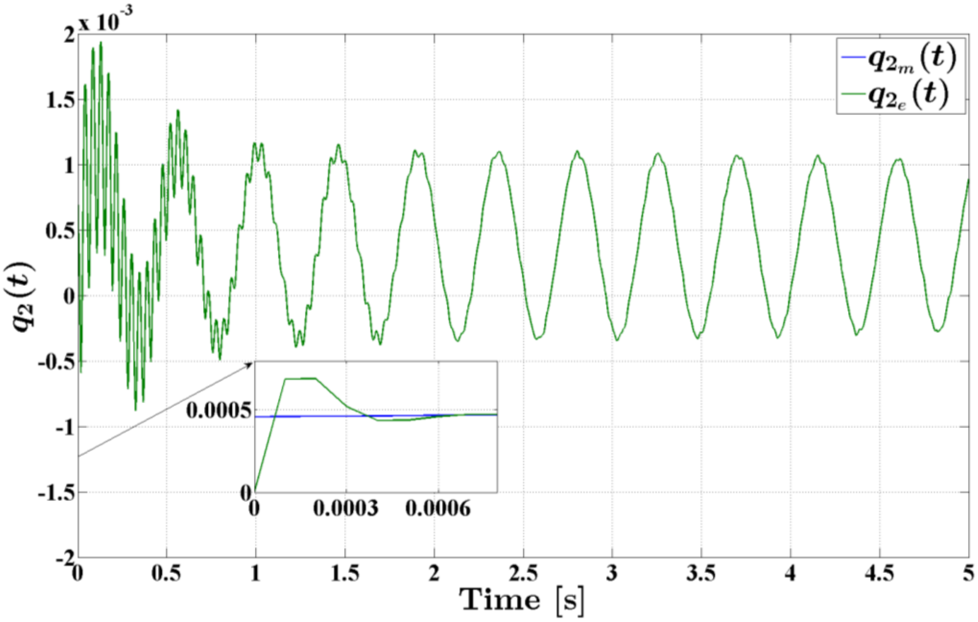

Fig. 3-32. Experimental results for $q_{2_m}(t)$ and $q_{2_e}(t)$ induced by an initial impulsive force

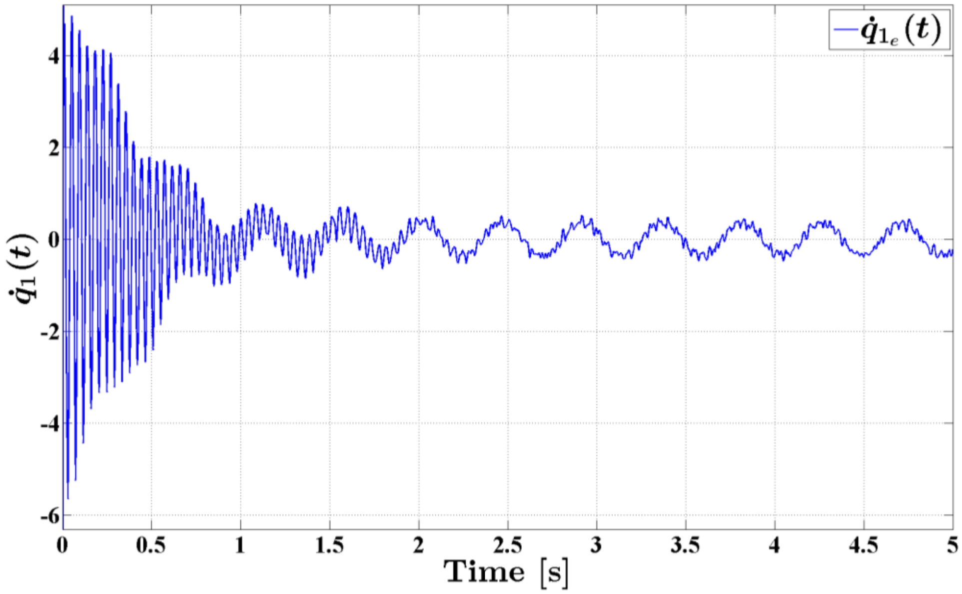

Fig. 3-33. Experimental result for $\dot{q}_{1_e}(t)$ induced by an initial impulsive force

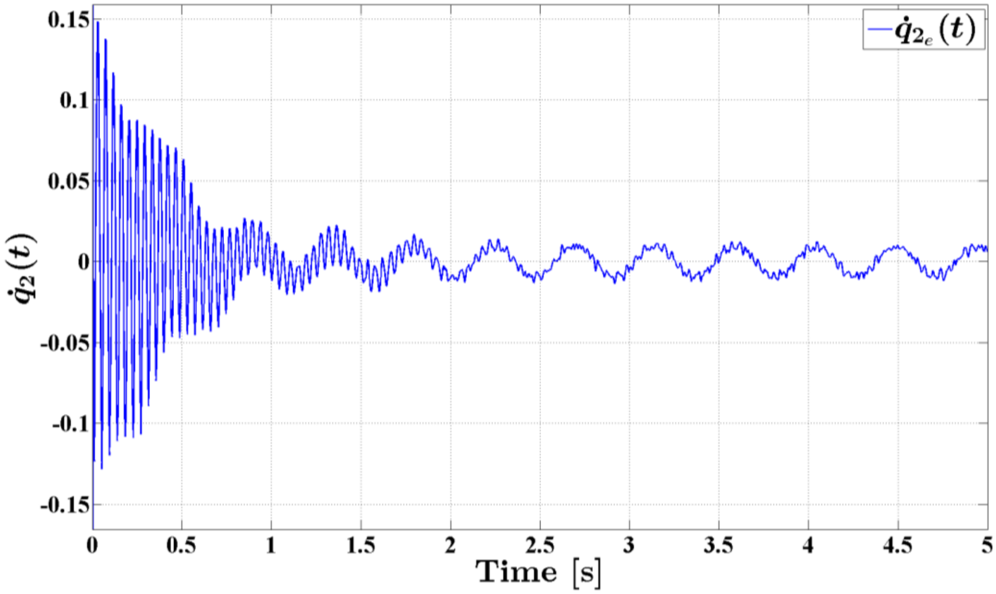

Fig. 3-34. Experimental result for $\dot{q}_{2_e}(t)$ induced by an initial impulsive force

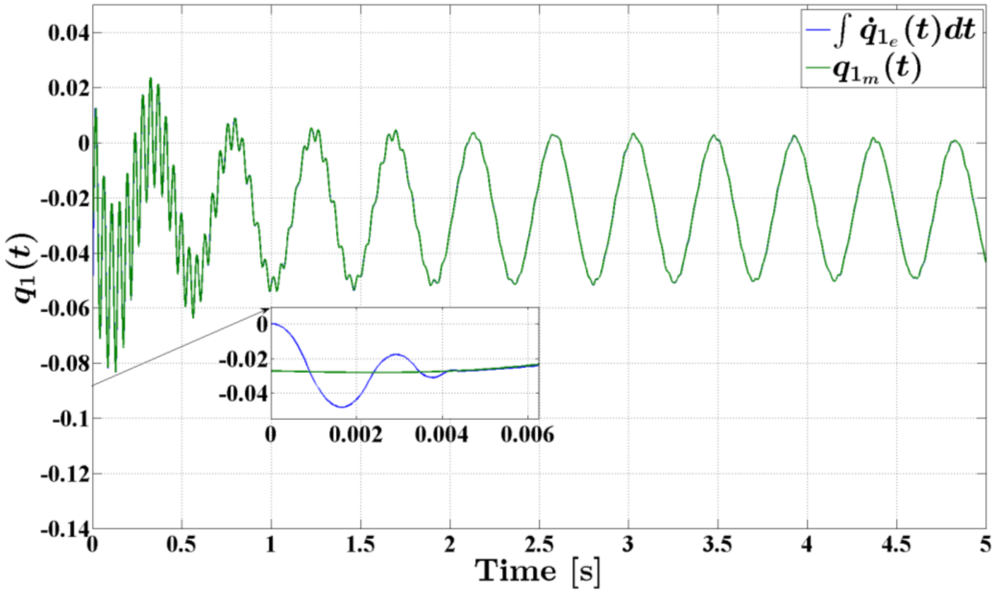

Fig. 3-35. Experimental results comparing $\int \dot{q}_{1_e} dt$ to q_{1_m}

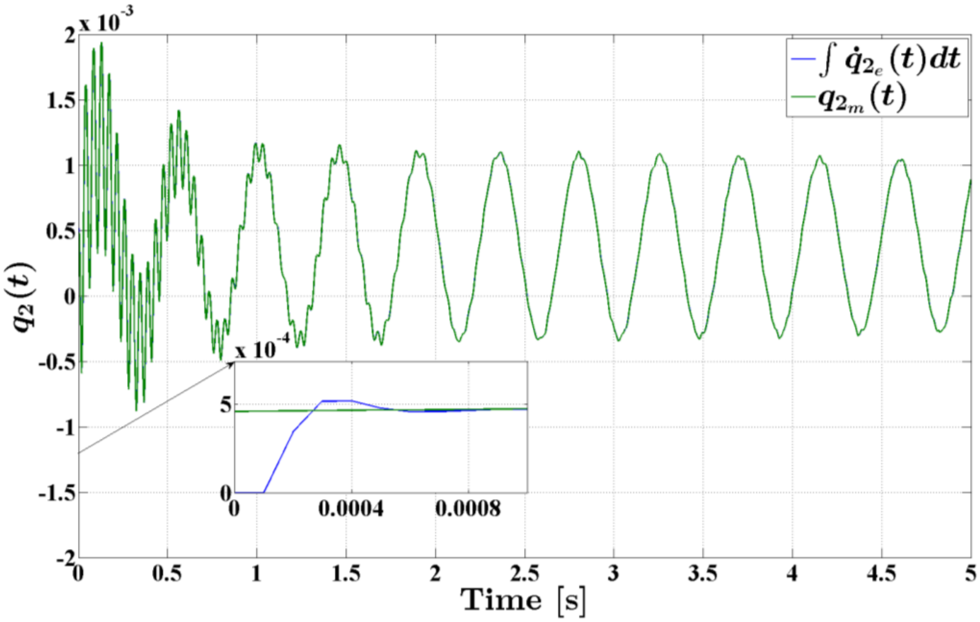

Fig. 3-36. Experimental results comparing $\int \dot{q}_{2_e} dt$ to q_{2_m}

The second experiment was conducted to assess the performance of the self-tuning observer during tracking tasks of the robot. The rigid body SMC, whose parameters are listed in Table 3-5, was used to maneuver the end-effector along the same path prescribed in Fig. 3-13. The initial conditions for the observers were kept the same as in Eq. (3-35). However, the initial conditions of the robot arm were found to be

$$\underset{\sim}{x}^T(0) = \left[9.4^\circ, 0.315, -0.03, 0, 0.004, 0, 0, 0, -0.396, 0, 0.05, 0\right] \qquad (3\text{-}38)$$

The nonzero values for $q_1(0), q_3(0), \dot{q}_1(0)$ and $\dot{q}_3(0)$ reflect the fact that the beam was vibrating at the onset of the tracking maneuver of the end-effector. The good tracking characteristic of the SMC is illustrated in Figs. 3-37 and 3-38, which reveal a rapid convergence of $\theta_1(t)$ and $r(t)$ to their desired values of

$\theta_{1_d}(t)$ and $r_d(t)$. Figures 3-39 to 3-42 include the plots of $q_{1_m}(t)$ and $q_{3_m}(t)$ along with those of the estimated variables $q_{1_e}(t), q_{3_e}(t), \dot{q}_{1_e}(t)$ and $\dot{q}_{3_e}(t)$. These plots validate the robust capabilities of the observer in yielding a rapid convergence rate and providing accurate estimation of the actual generalized coordinates of the flexible motion of the third link in spite of considerable modeling imprecision (see Table 3-2). These figures also demonstrate the fluctuations in the natural frequencies and the sagging of the flexible portion of the third link as the end-effector maneuvers between points A, B, and C. It should be pointed out that the intermittent appearance of high frequency components in the plots of Figs. 3-41 and 3-42 exhibits the contribution of the higher order dynamics of the flexible link when the end-effector is in the vicinity of points B and C where the third link is fully protruded.

The accuracy of $\dot{q}_{1_e}(t)$ and $\dot{q}_{3_e}(t)$ plots in Figs. 3-41 and 3-42 are validated by integrating the results with respect to time and comparing them to $q_{1_m}(t)$ and $q_{3_m}(t)$. Hence confirming that $q_{1_m}(t)$ and $q_{3_m}(t)$ can be reconstructed from the estimated $\dot{q}_{1_e}(t)$ and $\dot{q}_{3_e}(t)$, respectively (see Figs. 3-43 and 3-44).

The plots in Figs. 3-45 to 3-50 represent the variables estimated by the SMO, which are the counterparts of the results shown in Figs. 3-39 to 3-44. These figures prove that the SMO is capable of yielding similar level of accuracy and rate of convergence for the state variables as the STO.

SMC Parameters Used in Experiments	
$\hat{f}_{r_3}^{R},\ \hat{f}_{r_4}^{R}$	$0\ \mathrm{rad.s}^{-2},\ 0\ \mathrm{m.s}^{-2}$
$F_3^{R},\ F_4^{R}$	$5\ \mathrm{rad.s}^{-2},\ 2\ \mathrm{m.s}^{-2}$
$\left(b_{r_1}^{R}\right)_{\min},\ \left(b_{r_2}^{R}\right)_{\min}$	$1, 1$
$\left(b_{r_1}^{R}\right)_{\max},\ \left(b_{r_2}^{R}\right)_{\max}$	$10, 10$
λ_1, λ_2	$100, 5$
ϕ_{C_1}, ϕ_{C_2}	$0.01, 0.001$
η_{C_1}, η_{C_2}	$5, 1$

Table 3-5. Experimental sliding mode controller parameters

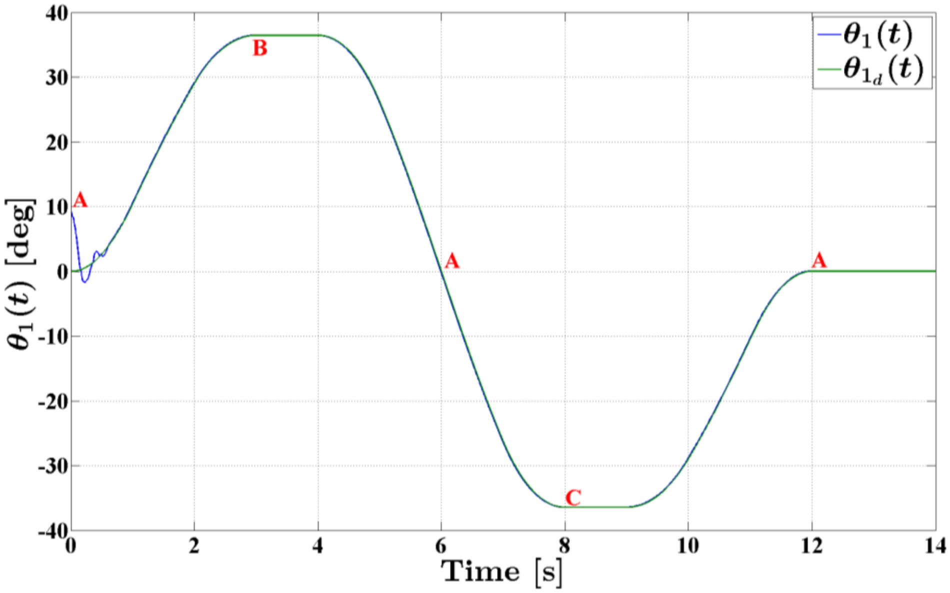

Fig. 3-37. Experimental results for $\theta_{1_d}(t)$ and $\theta_1(t)$ during the tracking maneuver of the arm

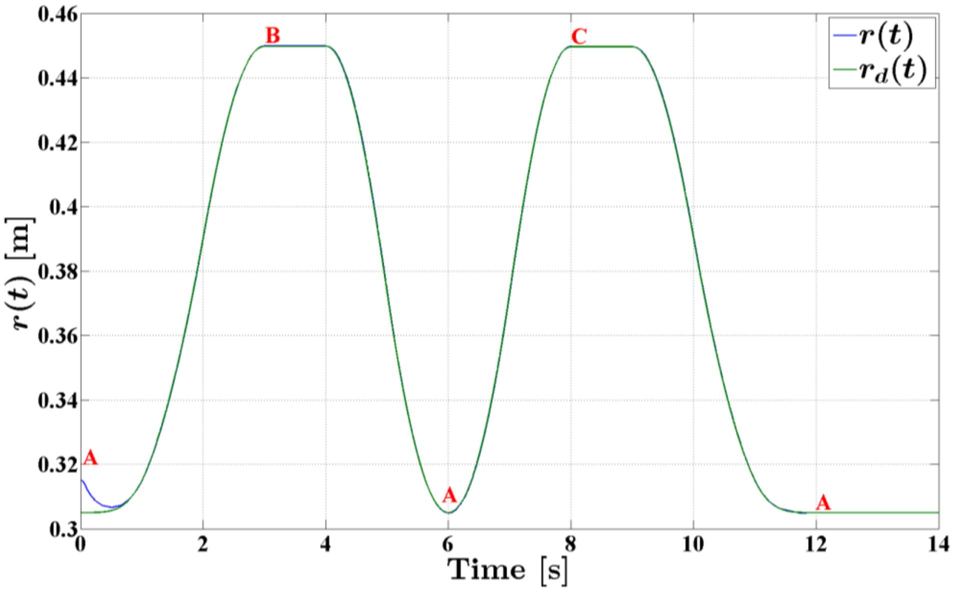

Fig. 3-38. Experimental results for $r_d(t)$ and $r(t)$ during the tracking maneuver of the arm

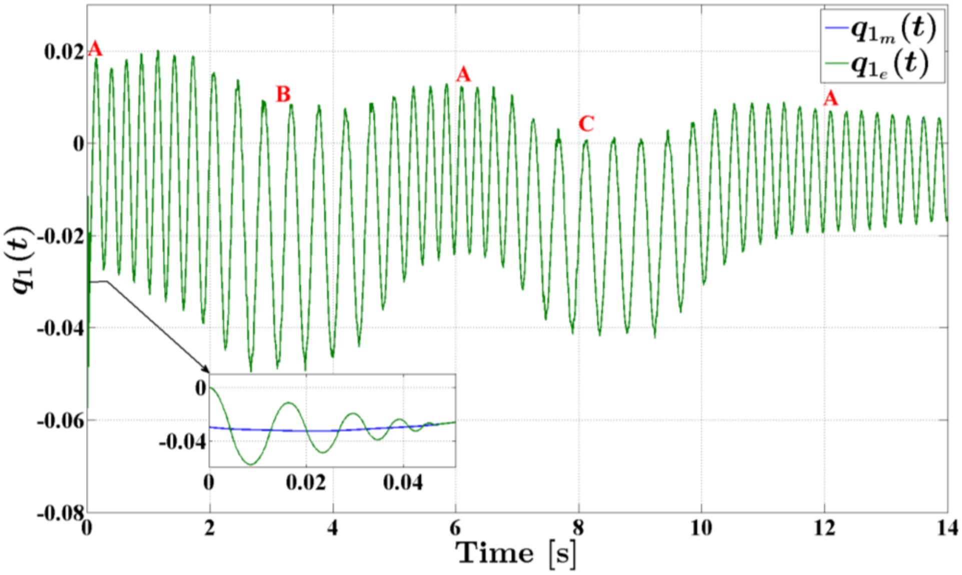

Fig. 3-39. Experimental results for $q_{1_m}(t)$ and $q_{1_e}(t)$ during the tracking maneuver of the arm

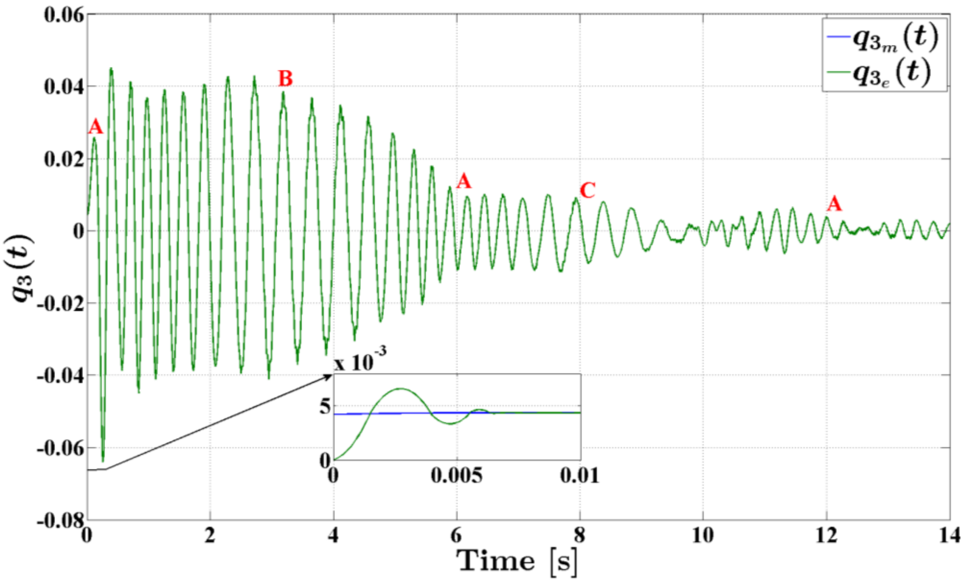

Fig. 3-40. Experimental results for $q_{3_m}(t)$ and $q_{3_e}(t)$ during the tracking maneuver of the arm

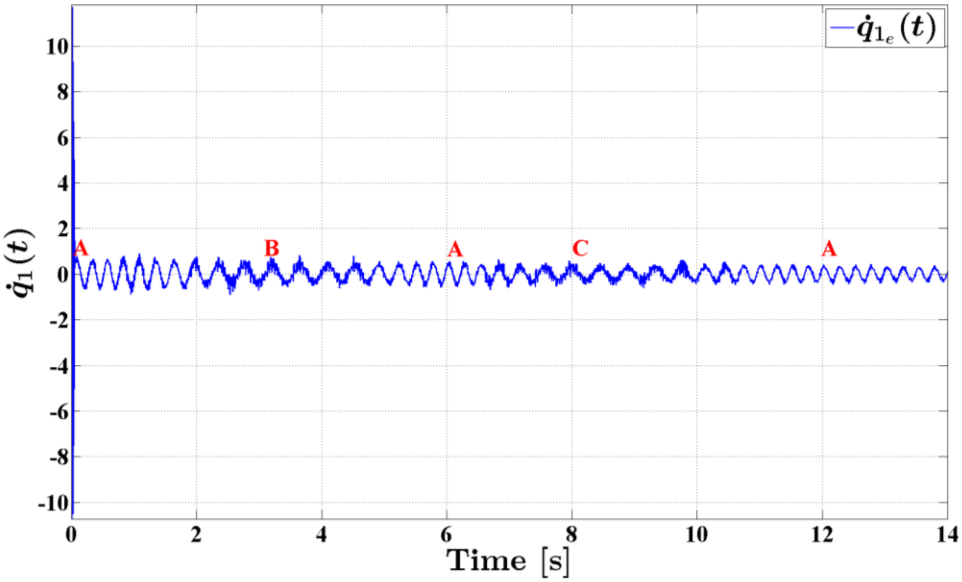

Fig. 3-41. Experimental result for $\dot{q}_{1_e}(t)$ during the tracking maneuver of the arm

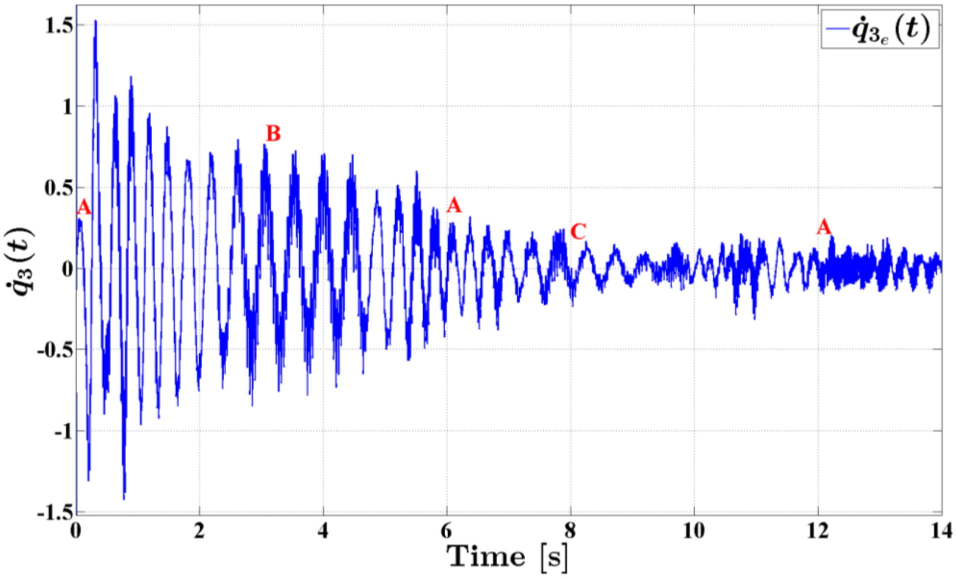

Fig. 3-42. Experimental result for $\dot{q}_{3_e}(t)$ during the tracking maneuver of the arm

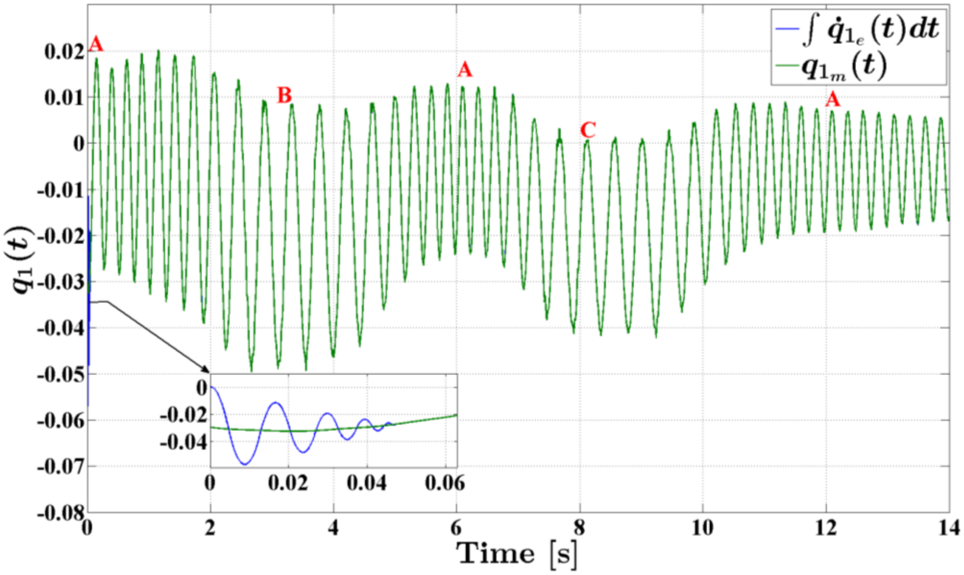

Fig. 3-43. Experimental results comparing $\int \dot{q}_{1_e} dt$ to q_{1_m}

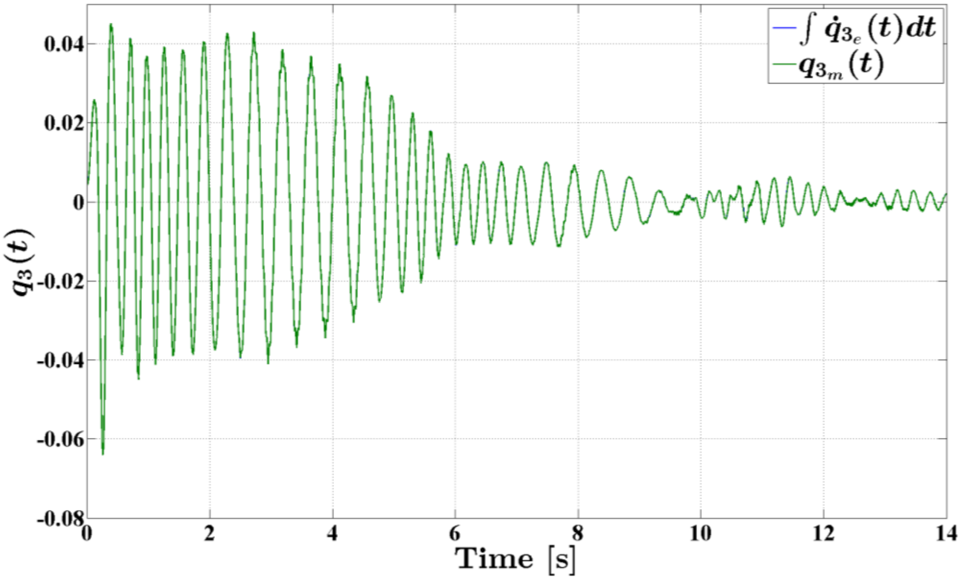

Fig. 3-44. Experimental results comparing $\int \dot{q}_{3_e} dt$ to q_{3_m}

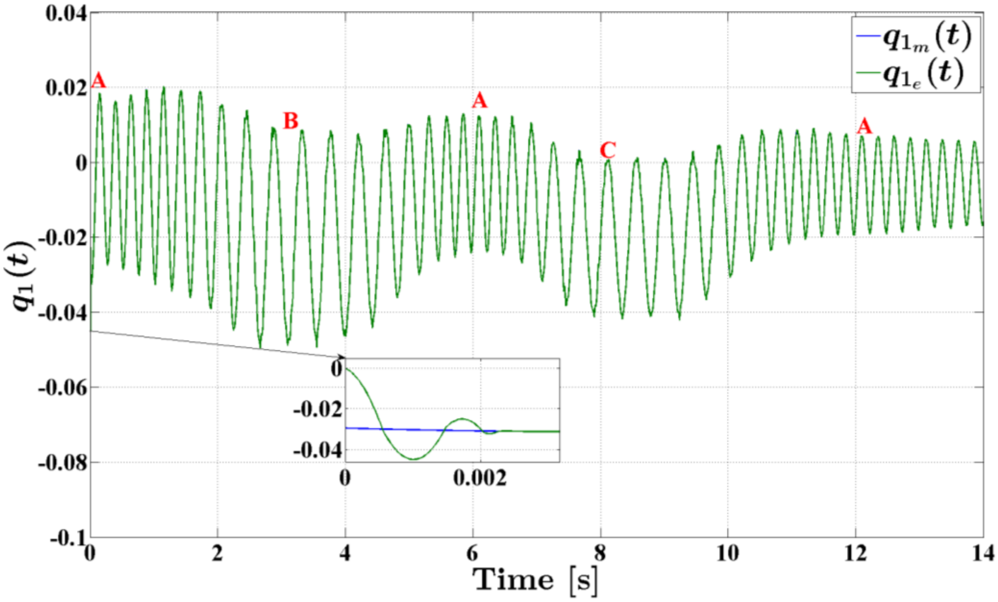

Fig. 3-45. Experimental results for $q_{1_m}(t)$ and $q_{1_e}(t)$ during the tracking maneuver

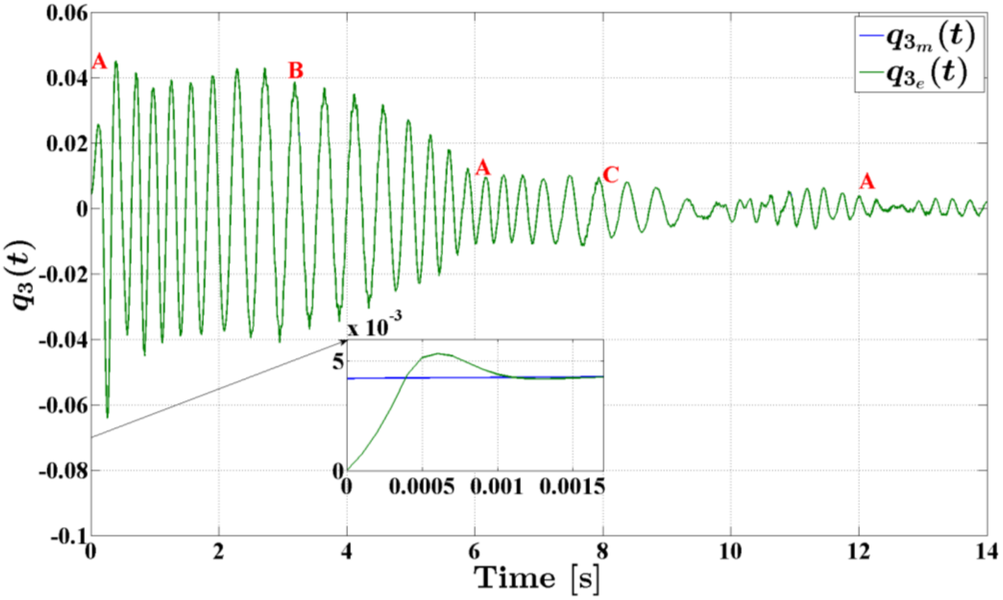

Fig. 3-46. Experimental results for $q_{3_m}(t)$ and $q_{3_e}(t)$ during the tracking maneuver

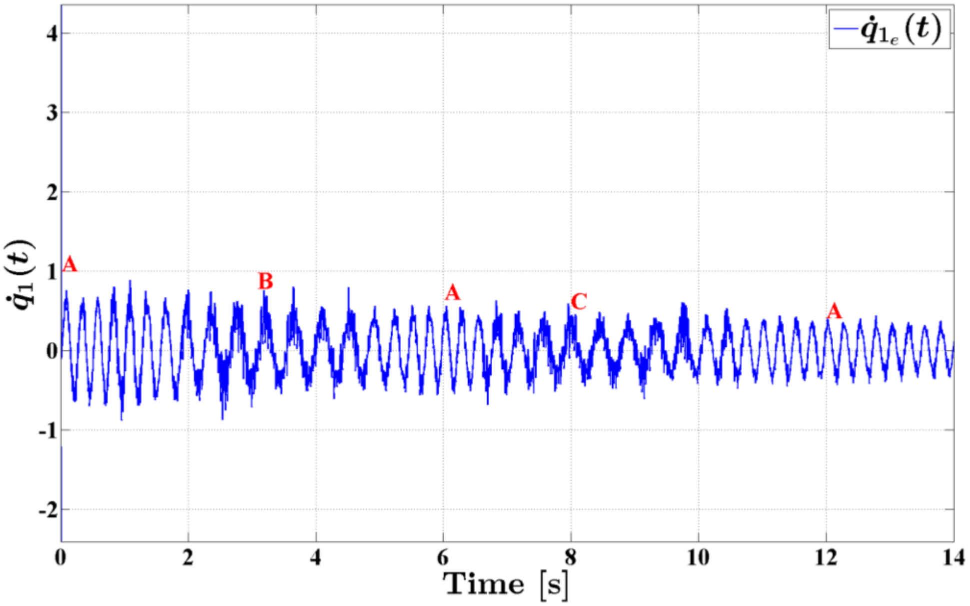

Fig. 3-47. Experimental result for $\dot{q}_{1_e}(t)$ during the tracking maneuver

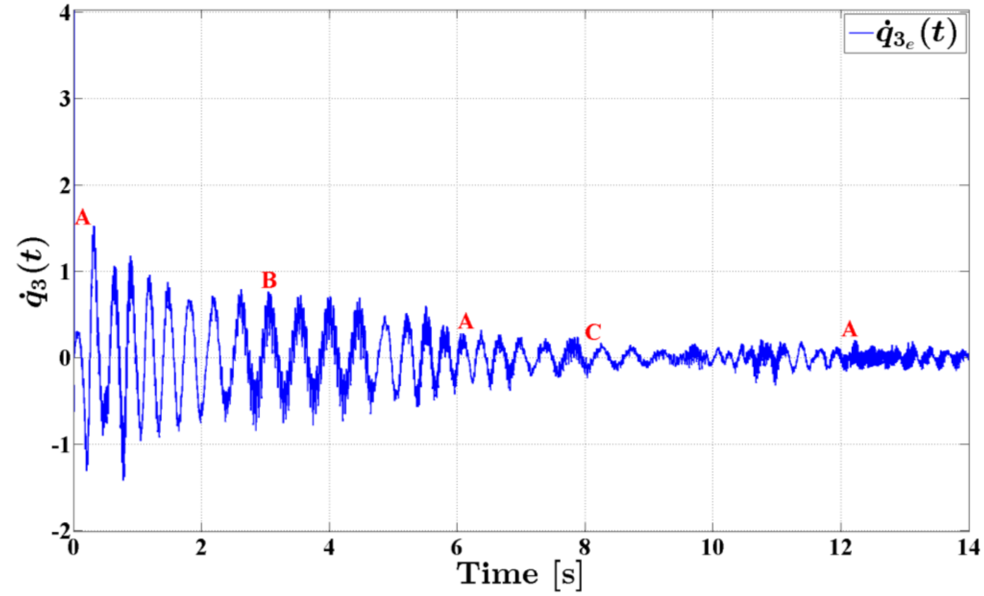

Fig. 3-48. Experimental result for $\dot{q}_{3_e}(t)$ during the tracking maneuver

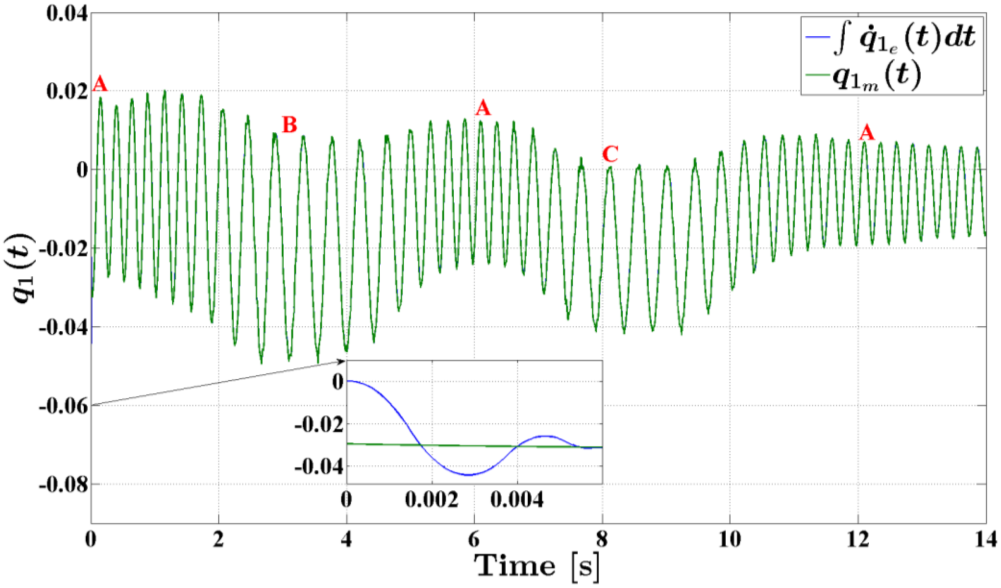

Fig. 3-49. Experimental results comparing $\int \dot{q}_{1_e}\,dt$ to q_{1_m}

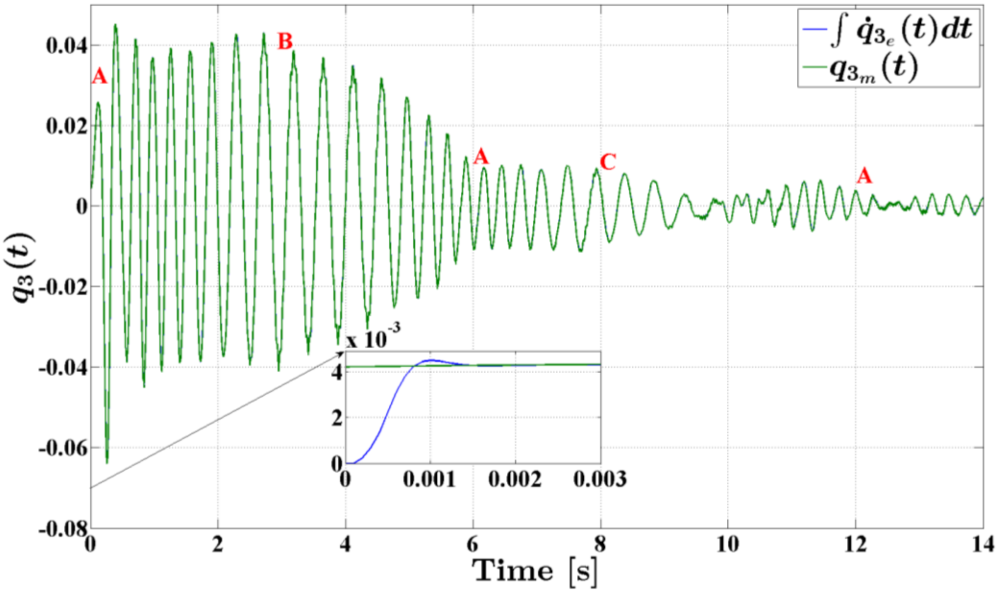

Fig. 3-50. Experimental results comparing $\int \dot{q}_{3_e} dt$ to q_{3_m}

3.8 Summary

The current Chapter has focused on providing experimental validation for the robust performances of two nonlinear observers. The first one is a self-tuning observer while the second one is a sliding mode observer. Both observers exhibited same level of accuracy and rate of convergence in estimating the state variables of a structure whose natural frequencies depends on its geometric configuration. The physical system is considered to be a spherical robotic manipulator whose second revolute joint has been deactivated. Only the protruding portion of the third link from the second link is considered to be flexible. During a given maneuver of the arm, the prismatic joint will usually vary the length of the flexible portion of the third link; thus, inducing significant variations in its natural frequencies. Both observers have been implemented to estimate the generalized coordinates of the flexible motion of the arm under two different types of excitation. In the first one, either initial conditions or an impulsive force was used to excite the first two elastic modes of the in-plane and out-of-plane transverse deformations of the flexible link. While in the second type of excitation, the structural deformations are induced by the rigid body motion of the arm during its tracking maneuver of a straight line in the work envelope of the robot. A basic sliding mode controller has been implemented to control the rigid body degrees of freedom of the robot during the tracking maneuver.

The parameters for both observers have been kept the same during the theoretical and experimental work. The results validate the robust performances of the self-tuning and sliding mode observers by revealing a fast convergence rate and accurate estimation of the actual generalized coordinates of the flexible motion of the third link in the presence of considerable structured and unstructured uncertainties of the system.

These two observers are used in the next Chapter to estimate the state variables of a marine surface vessel. The estimated state variables are then used in the computation of the control signal for the surge speed controller of the vessel.

CHAPTER 4 MARINE VESSEL CONTROLLERS AND OBSERVERS

In order to successfully control a marine vessel during its tracking task, a set of fundamental obstacles need to be overcome. Due to the nature of the system and its unpredictable environmental conditions, the controller should be robust to external disturbances along with structured and unstructured uncertainties. Moreover, the implementation of the controller requires that the state variables be available for the computation of the control signals.

To deal with these challenging issues, a robust control algorithm has been implemented along with nonlinear state observers to accurately estimate the required state variables. The current Chapter covers the formulation of the controller and the observers for under-actuated marine surface vessels undergoing maneuvering and course tracking tasks.

4.1 Control Strategy

To successfully control an under-actuated vessel, the controller is usually integrated with a guidance system. The latter is based on the variable radius line-of-sight (LOS) and acceptance circles around the waypoints. The guidance system will provide the controller with the desired heading angle that is needed to point the ship in the right direction while reducing the cross track error; thus, enabling the controller to compensate for both heading angle and sway motion with one control signal. As a result, the ship tracking problem is now reduced to surge speed and heading angle tracking tasks for which two control variables are readily available, namely, the propeller thrust and the propeller orientation. The remainder of this Section is devoted for the proposed hybrid controller, which encompasses different versions of surge speed and heading controllers along with recovery controllers.

The hybrid control strategy, devised for this problem, consists of five controllers that are being managed by a main supervisory algorithm. Two of these controllers are devoted for tracking and maneuvering operations of the vessel based on feedback signals representing the actual surge speed and heading angle of the boat. Another two controllers provide the user with the option of performing either point-to-point (PTP) or prescribed throttle angle and steering control tasks. The feedback signals for PTP controllers are obtained from optical encoders mounted on their respective servomotors. However, the prescribed throttle angle and steering control tasks are performed based on feedback signals pertaining to the actual surge speed and heading angle of the boat. The fifth controller, referred to herein as a “recovery” controller, is only activated in the case of unforeseen mishaps. Its main function is to drive back the throttle arm to a neutral position; thus, reducing the propeller thrust to zero in a controlled manner. The supervisory algorithm orchestrates the functioning of these controllers to successfully track a desired trajectory while ensuring a safe operation of the marine vessel. Its role entails defining the system’s initial conditions, activating the appropriate controllers, and triggering the recovery controller when needed.

A robust controller, based on the work of Chalhoub and Khaled (2014), has been implemented to control the surge speed and heading angle of the marine vessel based on feedback signals from the GPS and gyro compass systems.

4.1.1 Supervisory Algorithm

As stated earlier, the objective of the supervisory algorithm is to ensure synchronized operation of all system components. At its highest level, the supervisory code provides the user with the capability of invoking the "recovery" controller should any unforeseen emergency situation arises. Furthermore, it allows the user to select PTP controllers, prescribed throttle arm and heading angle controllers, or tracking controllers for either the surge speed or the vessel's heading control tasks; thus, rendering the code as versatile as possible.

Upon enabling the system, a "Stateflow" chart triggering loop takes over the decision-making and synchronization processes. Past this point, the user's input is restricted to the push-button emergency switch that has the capability to abort the boat maneuver. Every process the system may initiate is represented by a state in the Stateflow chart. Once activated, every state would trigger its respective controller or operation. As a safety measure, each of these states routinely monitors for pre-defined events induced by critical operations. Once any of these events occur, a system shutdown flag will be raised and both surge speed and steering maneuvers go into a recovery mode. Safe operation envelopes for both throttle handle and steering wheel angular displacements have been set to $\left[\theta_{\min}^{throttle}, \theta_{\max}^{throttle}\right]$ and $\left[\theta_{\min}^{steering}, \theta_{\max}^{steering}\right]$, respectively. Critical operating conditions are declared whenever one or both of these intervals of angular displacements are breached.

The recovery strategy has been designed to get the boat into a safe state without putting the crew at risk during the process. For instance, instead of suddenly turning off the propeller's thrust, a predefined deceleration profile has been employed in order to minimize the surge of water at the stern and the sudden jerking motion that could throw an unsuspecting crew member off-board. Additionally, the recovery control action for the steering wheel DC servomotor will assign a zero command voltage in order to halt any rotation maneuver and lock the steering wheel in place. The rationale behind this choice of action stems from the fact that the loss of throttle thrust will lead to a loss in steering capability.

At the onset of the fully autonomous mode of operation of the vessel, the Stateflow chart initiates an initialization task before engaging the tracking controllers. Note that a gyro compass is used herein to measure the yaw angle of the boat. The output signal of the sensor represents the yaw angular velocity instead of the angular displacement. Thus, this signal has to be integrated with respect to time to yield the actual yaw angle. In order to avoid the offset error induced by the constant of integration, an algorithm based on the least squares regression line scheme is incorporated into the main code to accurately estimate the initial boat orientation. The Stateflow chart will activate an initial boat orientation module that will drive the boat at a constant cruising speed for few seconds along the initial orientation of the vessel. During this phase of operation, the boat will be controlled by a conventional sliding mode controller (SMC) to track a predefined surge speed profile along a straight line trajectory. The relative X- and Y-coordinates with respect to the boat's initial position will be continuously recorded and then curve fitted by a least squares regression line algorithm to estimate the initial orientation of the boat with respect to an axis pointing along the east direction. It is only when this task is completed that the supervisory algorithm activate the tracking controllers of the fully-autonomous mode of operation.

Several tests have been conducted on the boat in open-water to validate this procedure for determining the initial orientation of the boat. The SMC was used to track a certain profile of the surge speed while forcing the boat to move along the direction of its initial orientation. The total duration of each test was 10 seconds and the relative X- and Y-coordinates with respect to the boat's initial position were recorded and plotted in Fig. 4-1. These data were curve fitted by a least squares regression line algorithm that led to the initial orientation of the boat being at $117.34^{\circ}, -126.57^{\circ}, 142^{\circ}$ with respect to an axis along the east direction (see Fig. 4-1).

4.1.2 Desired State Variables and Vessel's Nominal Model

The objective of the surge speed controller is to make the boat's speed track the desired speed profile specified along the desired trajectory by the path planner. Figure 4-2 illustrates the desired trajectory, which is often constructed by sequentially connecting a set of waypoints. The projection of the boat position onto the highlighted $(i+1)^{th}$ segment defines a local coordinate $\overline{x}_i$ with respect to the i^{th} waypoint (X_i, Y_i) and along the segment connecting the i^{th} and $(i+1)^{th}$ waypoints. The highlighted pathway in Fig. 4-2 shows segments of the desired trajectory that should be tracked. The circles centered at the waypoints are called Circles of Acceptance. Once the vessel enters a circle of acceptance, the guidance system will shift its tracking focus to the subsequent segment along the desired trajectory. For example, the guidance system will switch its focus to the $(i+2)^{th}$ segment as soon as the boat enters the circle of acceptance centered at (X_{i+1}, Y_{i+1}) waypoint. This switch in segment tracking occurs in spite of the fact that the tracking of the $(i+1)^{th}$ segment is not completed; hence, compromising tracking with optimal maneuvering performance.

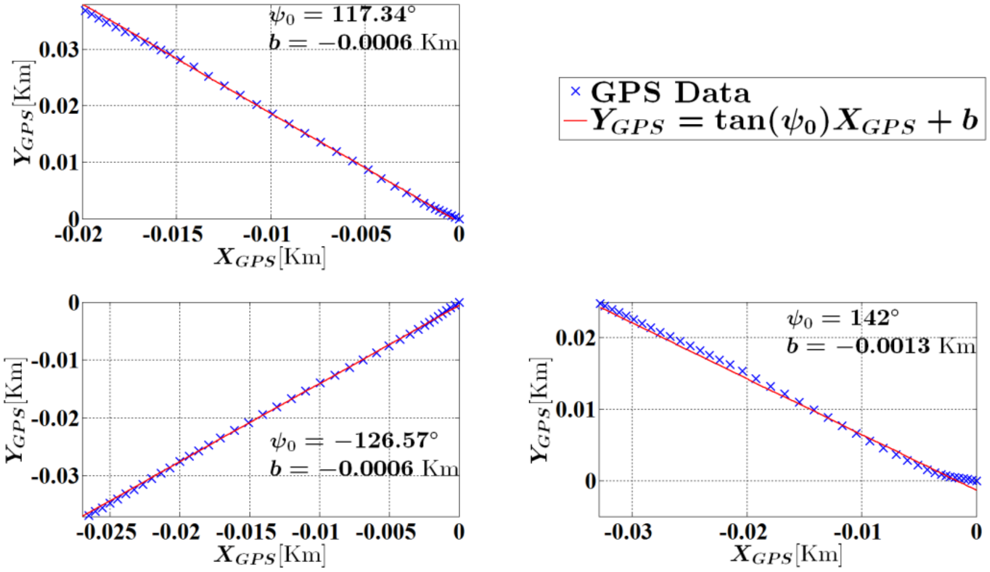

Fig. 4-1. Initial heading orientations based on the least squares method

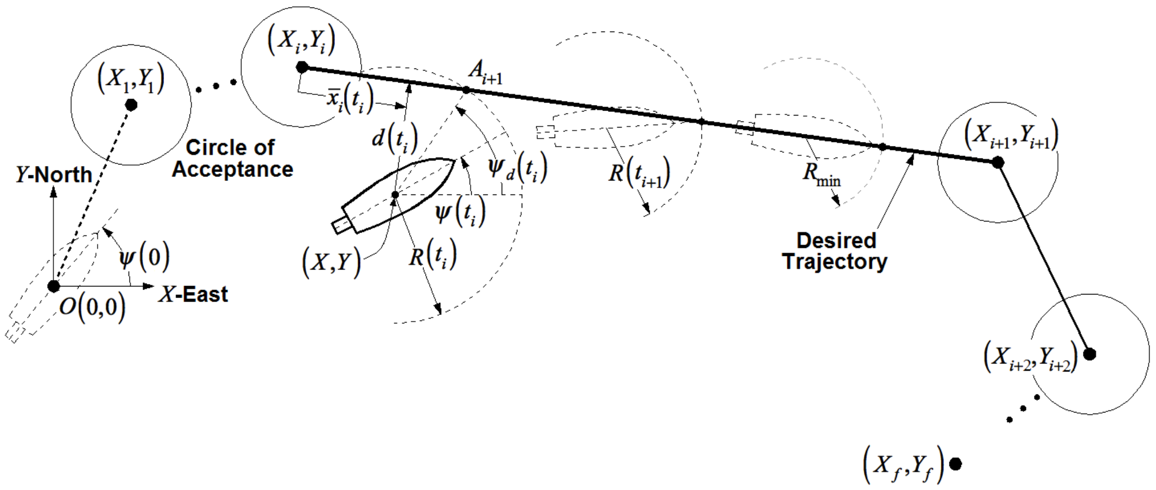

Fig. 4-2. Vessel's location with respect to the desired trajectory

The time derivative of the projected boat location onto the $(i+1)^{th}$ segment, $\dot{\bar{x}}_i$, represents the state variable that is being controlled by the robust surge speed controller. A typical desired surge speed profile for a multi-segment trajectory is shown in Fig. 4-3, which reveals acceleration, cruising, and deceleration phases for each segment of the trajectory. For a safe operation, the boat is required to reduce its speed from a cruising speed, V_{cruise}, to a maneuvering speed, V_{maneu}, around the waypoints.

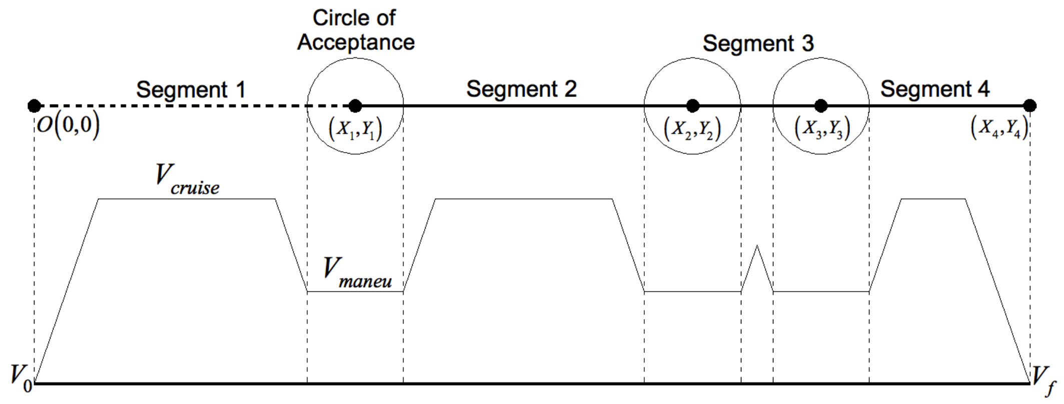

Fig. 4-3. Desired velocity profile, $\dot{\bar{x}}_{i_d}$, for flattened multi-segment trajectory

As for the heading controller, the objective is to force the actual yaw angle of the boat to accurately track the desired heading angle, ψ_d, specified by the guidance system.

The nominal model of the marine surface vessel, based on which all controllers are designed, is expressed as follows

$$\ddot{\bar{x}}_i = \hat{f}_s\left(\dot{\bar{x}}_i\right) + \hat{b}_1\left(\dot{\bar{x}}_i\right)v_{c_s} \tag{4-1}$$

$$\ddot{\psi} = \hat{f}_h\left(\dot{\psi},\psi\right) + \hat{b}_2\left(\dot{\psi},\psi\right)v_{c_h} \tag{4-2}$$

where $\dot{\bar{x}}_i$ and $\ddot{\bar{x}}_i$ denotes the actual surge speed and acceleration of the boat along the $(i+1)^{th}$ segment, respectively. The input signals, v_{c_s} and v_{c_h}, are the control voltage signals specified by the tracking controllers to the DC servomotors responsible for rotating the throttle arm and steering wheel. As a precautionary measure, both v_{c_s} and v_{c_h} have been run through saturation functions that limit them to $\pm 10\mathrm{V}$ in order to protect the $12\mathrm{V}$ servomotors from sudden current surges. The dynamics of the marine vessel are lumped into two terms $f_s\left(\dot{\bar{x}}_i\right)$ and $f_h\left(\dot{\psi},\psi\right)$, which will never be exactly known due to simplifying assumptions and environmental uncertainties. Thus, the controllers have been developed based on the nominal dynamic equations given by Eqs. (4-1) and (4-2). Note that $\hat{f}_s\left(\dot{\bar{x}}_i\right)$ and $\hat{f}_h\left(\dot{\psi},\psi\right)$ are the best available approximation of $f_s\left(\dot{\bar{x}}_i\right)$ and $f_h\left(\dot{\psi},\psi\right)$. Similarly, the input gains, $b_1\left(\dot{\bar{x}}_i\right)$and $b_2\left(\dot{\psi},\psi\right)$, are represented by their nominal values, $\hat{b}_1(\dot{\bar{x}}_i)$ and $\hat{b}_2(\dot{\psi},\psi)$, which are considered to be bounded as follows (Slotine and Li, 1991)

$$\hat{b}_1 = \sqrt{b_{1_{\min}} b_{1_{\max}}} \qquad \hat{b}_2 = \sqrt{b_{2_{\min}} b_{2_{\max}}} \tag{4-3a}$$

$$\beta_1 = \sqrt{\frac{b_{1_{\max}}}{b_{1_{\min}}}} \qquad \beta_2 = \sqrt{\frac{b_{2_{\max}}}{b_{2_{\min}}}} \tag{4-3b}$$

$$\beta_1^{-1} \le b_1^{-1}\hat{b}_1 \le \beta_1 \qquad \beta_2^{-1} \le b_2^{-1}\hat{b}_2 \le \beta_2 \tag{4-3c}$$

where $b_{1_{\max}}$, $b_{1_{\min}}$, $b_{2_{\max}}$, and $b_{2_{\min}}$ are considered to be known. Following the work of Chalhoub and Khaled (2014), three state variables are used in generating the following state vector equation:

$$\dot{\underset{\sim}{x}} = \underset{\sim}{\hat{f}}(\underset{\sim}{x}) + \hat{b}(\underset{\sim}{x})\underset{\sim}{u} \quad \text{where} \quad \underset{\sim}{x} = \begin{pmatrix} x_1 = \psi \\ x_2 = \dot{\bar{x}}_i \\ x_3 = \dot{\psi} \end{pmatrix} \tag{4-4}$$

$$\underset{\sim}{u} = \begin{pmatrix} u_1 = v_{c_s} \\ u_2 = v_{c_h} \end{pmatrix}, \qquad \underset{\sim}{\hat{f}} = \begin{Bmatrix} \hat{f}_1 = \dot{\psi} \\ \hat{f}_2 = \hat{f}_s \\ \hat{f}_3 = \hat{f}_h \end{Bmatrix} \qquad \hat{b} = \begin{bmatrix} 0 & 0 \\ \hat{b}_1 & 0 \\ 0 & \hat{b}_2 \end{bmatrix}$$

The above nominal model has been used in the design of the surge speed and heading controllers.

4.1.3 Surge Speed and Heading Controllers

The surge speed and heading tracking errors are defined as follows

$$\tilde{x}_s = \int_0^t \left(\dot{\bar{x}}_i - \dot{\bar{x}}_{i_d}\right) d\tau \tag{4-5a}$$

$$\tilde{x}_h = \psi - \psi_d \tag{4-5b}$$

where $\dot{\bar{x}}_{i_d}$ and ψ_d are the desired surge speed and heading angles, respectively. The sliding surfaces used in designing the surge speed and heading controllers are selected as follows

$$s_1\left(\dot{\tilde{x}}_s, \tilde{x}_s\right) = \left(\frac{d}{dt} + \lambda_s\right)^2 \int_0^t \tilde{x}_s \, d\tau \tag{4-6a}$$

$$s_2\left(\dot{\tilde{x}}_h, \tilde{x}_h\right) = \left(\frac{d}{dt} + \lambda_h\right) \tilde{x}_h \tag{4-6b}$$

By implementing the sliding mode methodology, the entries of the control vector can be written as

$$u_i = u_{i_{eq}} - \frac{k_i}{\hat{b}_i} \operatorname{sgn}\left(s_i\right) \quad i = 1,\, 2 \tag{4-7}$$

By setting $\dot{s}_i = 0$ for $i = 1 \text{ and } 2$, one would obtain

$$u_{1_{eq}} = \frac{1}{\hat{b}_1}\left[-\hat{f}_s + \ddot{\bar{x}}_{i_d} - 2\lambda_s \dot{\tilde{x}}_s - \lambda_s^2 \tilde{x}_s \right] \tag{4-8a}$$

$$u_{2_{eq}} = \frac{1}{\hat{b}_2}\left[-\hat{f}_h + \ddot{\psi}_d - \lambda_h \dot{\tilde{x}}_h \right] \tag{4-8b}$$

By satisfying the sliding conditions, the $k_i = 0$ gains for $i = 1 \text{ and } 2$ can be expressed as

$$k_1 \geq \beta_1\left(\eta_s + F_s\right) + \left|\beta_1 - 1\right| \left| \hat{f}_2 + 2\lambda_s \dot{\tilde{x}}_s + \lambda_s^2 \tilde{x}_s - \ddot{\bar{x}}_{i_d} \right| \tag{4-9a}$$

$$k_2 \geq \beta_2\left(\eta_h + F_h\right) + \left|\beta_2 - 1\right| \left| \hat{f}_3 + \lambda_h \dot{\tilde{x}}_h - \ddot{\psi}_d \right| \tag{4-9b}$$

where η_s and η_h are control parameters. F_s and F_h represent the upper bounds on the modeling uncertainties as follows

$$F_s \geq \left| f_2 - \hat{f}_2 \right|_{\sup} \tag{4-10a}$$

$$F_h \geq \left| f_3 - \hat{f}_3 \right|_{\sup} \tag{4-10b}$$

In order to alleviate the chattering in the control signals, the i^{th} switching term, $\mathrm{sgn}(s_i)$, in Eq. (4-7) has been substituted by $\mathrm{sat}\left(\frac{s_i}{\Phi_i}\right)$ where Φ_i is the thickness of the boundary layer surrounding the i^{th} sliding surface.

4.1.4 Recovery, PTP, and Alternative Controllers

The supervisory algorithm, presented in Subsection 4.1.1, ensures a controlled shut down of the system in case of unfortunate mishaps or closed-loop malfunctions through a pair of recovery actions. Two safe ranges of angular displacement have been specified for the throttle arm and the steering wheel. When one or both ranges are breached, the supervisory algorithm will enable an emergency flag that will set the system into a recovery mode of operation. As a consequence, the boat speed is gradually brought down to zero by a dedicated throttle arm recovery controller. At the same time, the steering wheel is locked in place by assigning a zero voltage to its DC servomotor.

Another pair of controllers was also introduced to give the user the option of performing either a PTP control or prescribed profiles of the throttle arm and steering angles. These controllers will be very useful during the testing of the surge speed and heading controllers that are used during the autonomous mode of operation of the boat. For instance, the user can engage the LOS-based heading controller while manually controlling the throttle angle. Similarly, the GPS-based surge speed controller can be examined while having a steering regulator maintaining a constant heading direction.

Despite their different strategies and purposes, the above three controllers are designed based on the conventional sliding mode methodology (Slotine and Li, 1991). Their derivations are very similar and their formulations can be described in a generic form. The vector state equation representing the dynamics of either the throttle arm or the steering wheel can be written in the following general form:

$$\dot{\underset{\sim}{x}}_{gen_i} = \underset{\sim}{f}_{gen_i}\left(\underset{\sim}{x}_{gen_i}\right) + b_{gen_i}\left(\underset{\sim}{x}_{gen_i}\right)u_{gen_i} \qquad for \qquad i = 1, 2 \tag{4-11}$$

where $\underset{\sim}{x}_{gen} = \left[\theta_{gen_i} \;\; \dot{\theta}_{gen_i}\right]^T$, $\underset{\sim}{f}_{gen} = [\dot{\theta}_{gen_i} \;\; f_{gen_i}]^T$, and $\underset{\sim}{b}_{gen_i} = \left[0 \quad b_{gen_i}\right]^T$. Note that the subscripts gen_1 and gen_2 refer to throttle arm and steering wheel variables, respectively. For example, $\theta_{gen_1} = \theta_{throttle\_arm}$ is the angular displacement of the throttle arm as measured by the optical encoder that is mounted on the servomotor driving the throttle arm. Similarly, $\theta_{gen_2} = \theta_{steering}$ is the angular displacement of the steering wheel. Moreover, u_{gen_i} represents the control voltage signals v_{c_s} and v_{c_h} for $i = 1 \text{ and } 2$, respectively. The upper bound on modeling uncertainties is determined from $F_{gen_i} \geq \left|f_{gen_i} - \hat{f}_{gen_i}\right|_{\sup}$ where $\hat{f}_{gen_i}$ is the nominal expression that is available for f_{gen_i}. The nominal $\hat{b}_{gen_i}$ term is assumed to satisfy the following constraints:

$$\hat{b}_{gen_i} = \sqrt{b_{gen_{i_{\min}}} b_{gen_{i_{\max}}}} \tag{4-12a}$$

$$\beta_{gen_i} = \sqrt{\frac{b_{gen_{i_{\max}}}}{b_{gen_{i_{\min}}}}} \tag{4-12b}$$

$$\beta_{gen_i}^{-1} \le b_{gen_i}^{-1} \hat{b}_{gen_i} \le \beta_{gen_i} \tag{4-12c}$$

The following sliding surface is used:

$$s_{gen_i}\left(\dot{\tilde{x}}_{gen_i}, \tilde{x}_{gen_i}\right) = \dot{\tilde{x}}_{gen_i} + \lambda_{gen_i} \tilde{x}_{gen_i} \tag{4-13}$$

where

$$\tilde{x}_{gen_i} = \theta_{gen_i} - \theta_{gen_{i_d}} \tag{4-14}$$

Note that $\theta_{gen_{i_d}}$ and $\dot{\theta}_{gen_{i_d}}$ are the desired angular displacement and velocity profiles chosen for either the throttle arm or the steering wheel. For instance, in the recovery controller, $\theta_{throttle\_arm_d}$ and $\dot{\theta}_{throttle\_arm_d}$ are evaluated based on a user-defined velocity profile that will smoothly transition the throttle arm from either $\theta_{throttle\_arm_{\max}}$ or $\theta_{throttle\_arm_{\min}}$ to 0^o.

The control signal is computed from

$$u_{gen_i} = u_{gen_i}^{eq} - \frac{k_{gen_i}}{\hat{b}_{gen_i}} \operatorname{sgn}\left(s_{gen_i}\right) \tag{4-15}$$

By setting $\dot{s}_{gen_i} = 0$, $u_{gen_i}^{eq}$ can be expressed as

$$u^{eq}_{gen_i} = -\frac{1}{\hat{b}_{gen_i}}\left[\hat{f}_{gen_i} + \lambda_{gen_i}\dot{\tilde{x}}_{gen_i}\right] \tag{4-16}$$

The switching gain k_{gen_i} is evaluated based on the following sliding condition:

$$\frac{1}{2}\frac{d\left(s^2_{gen_i}\right)}{dt} \le -\eta_{gen_i}\left|s_{gen_i}\right| \tag{4-17}$$

which yields

$$k_{gen_i} \ge \beta_{gen_i}\left(\eta_{gen_i} + F_{gen_i}\right) + \left|\beta_{gen_i} - 1\right|\left|\hat{f}_{gen_i} + \lambda_{gen_i}\dot{\tilde{x}}_{gen_i}\right| \tag{4-18}$$

Again, to alleviate the adverse effects of the chattering phenomenon, the following control signal is used

$$u_{gen_i} = u^{eq}_{gen_i} - \frac{k_{gen_i}}{\hat{b}_{gen_i}}\operatorname{sat}\left(\frac{s_{gen_i}}{\phi_{gen_i}}\right) \tag{4-19}$$

4.2 Self-Tuning and Sliding Mode Nonlinear Observers

The main structures of both STO and SMO have already been discussed in Sections 3.2 and 3.3, respectively. In the current Section, only the implementation of these observers on a marine application will be discussed.

Both observers have been implemented to estimate the time derivatives of X and Y coordinates of the boat from the GPS data along with the heading angle and its time derivative from the gyro compass data. The vector state equation of the observer is given by

$$\dot{\underset{\sim}{x}}_o = \underset{\sim}{f}_o\left(\underset{\sim}{x}_o, \underset{\sim}{u}\right) \tag{4-20}$$

where $\underset{\sim}{x}_o^T = \left[X, Y, \psi, \dot{X}, \dot{Y}, \dot{\psi} \right]$ and $\underset{\sim}{f}_o^T = \left[\dot{X}, \dot{Y}, \dot{\psi}, f_{o_4}, f_{o_5}, f_{o_6} \right]$. Let the f_{o_i} terms be approximated by their nominal $\hat{f}_{o_i}$ expressions and define the structure of STO to be (Khaled and Chalhoub, 2012)

$$\dot{\hat{x}}_{o_i} = \hat{x}_{o_{i+3}} - K_{o_i} \operatorname{sgn}\left(s_{o_i}\right) \qquad i = 1, \cdots, 3 \tag{4-21a}$$

$$\dot{\hat{x}}_{o_{j+3}} = \hat{f}_{o_{j+3}}\left(\hat{\underset{\sim}{x}}_o, \underset{\sim}{u}\right) + \left[\frac{\sum_{k=1}^{m} w_k^j r_k^j}{\sum_{k=1}^{m} w_k^j} - \gamma_{o_j} s_{o_j}^2 \frac{\sum_{k=1}^{m} \left(w_k^j\right)^2}{\left(\sum_{k=1}^{m} w_k^j\right)^2} \operatorname{sgn}\left(s_{o_j}\right) \right] \qquad j = 1, \cdots, 3 \tag{4-21b}$$

The sliding surfaces are chosen to be:

$$s_{o_i} = \hat{x}_{o_i} - x_{o_{i_m}} = \tilde{x}_{o_i} \qquad i = 1, \cdots, 3 \tag{4-22}$$

Thus, the estimation error equation becomes

$$\dot{\tilde{x}}_{o_i} = \tilde{x}_{o_{i+3}} - K_{o_i} \operatorname{sgn}\left(s_{o_i}\right) \qquad i = 1, \cdots, 3 \tag{4-23a}$$

$$\dot{\tilde{x}}_{o_{j+3}} = \Delta f_{o_{j+3}} + \left[\frac{\sum_{k=1}^{m} w_k^j r_k^j}{\sum_{k=1}^{m} w_k^j} - \gamma_{o_j} s_{o_j}^2 \frac{\sum_{k=1}^{m} \left(w_k^j\right)^2}{\left(\sum_{k=1}^{m} w_k^j\right)^2} \operatorname{sgn}\left(s_{o_j}\right) \right] \qquad j = 1, \cdots, 3 \tag{4-23b}$$

where the $\Delta f_{o_{j+3}}$ terms are substituted by their upper bounds $F_{o_{j+3}} = \left| \hat{f}_{o_{j+3}} - f_{o_{j+3}} \right|_{\sup}$ for $j = 1, \cdots, 3$. By satisfying the sliding conditions, the gains, K_{o_i}, are given by

$$K_{o_i} \geq \eta_{o_i} + \left| \tilde{x}_{o_{i+3}} \right|_{upper\ bound} \qquad i = 1, \cdots, 3 \tag{4-24}$$

Following the procedure outlined in Section 3.2, the γ_{o_j} tuning parameters are required to satisfy the following inequalities:

$$\gamma_{o_j} > \frac{\left(\sum_{k=1}^{m} w_k^j\right)^2}{s_{o_j}^2 \sum_{k=1}^{m} \left(w_k^j\right)^2} \left[F_{o_{j+3}} + \frac{\sum_{k=1}^{m} w_k^j r_k^j \left(t - \Delta t\right)}{\sum_{k=1}^{m} w_k^j} \right] \quad \text{for} \quad j = 1, \cdots, 3 \qquad \text{(4-25)}$$

The structure of the SMO is defined by Eq. (4-21a) along with the following equation:

$$\dot{\hat{x}}_{o_{j+3}} = \hat{f}_{o_{j+3}}\left(\hat{\underset{\sim}{x}}_o, \underset{\sim}{u}\right) - K_{o_{j+3}} \operatorname{sgn}\left(s_{o_j}\right) \qquad j = 1, \cdots, 3 \qquad \text{(4-26)}$$

The sliding surfaces are selected to be the same as those used in the STO design, which are given in Eq. (4-22). Consequently, the error vector equation is given by Eq. (4-23a) along with the following equation:

$$\dot{\tilde{x}}_{o_{j+3}} = \Delta f_{o_{j+3}} - K_{o_{j+3}} \operatorname{sgn}\left(s_{o_j}\right) \qquad j = 1, \cdots, 3 \qquad \text{(4-27)}$$

The SMO gains, K_{o_j} for $j = 1, \cdots, 3$ are given by Eq. (4-24). Following the procedure outlined in Section 3.3, $K_{o_{j+3}}$ for $j = 1, \cdots, 3$ are required to satisfy the following inequalities:

$$K_{o_{j+3}} \geq \frac{F_{o_{j+3}} K_{o_j}}{\left|\tilde{x}_{o_{j+3}}\right|_{desired\_accuracy}} \quad for \quad j = 1, \cdots, 3 \qquad \text{(4-28)}$$

In order to alleviate the chattering problem, in both SMO and STO, the $\operatorname{sgn}\left(s_{o_j}\right)$ terms were substituted by $\operatorname{sat}\left(\frac{s_{o_j}}{\phi_{o_j}}\right)$.

4.3 Experimental Set-Up

The experimental work of the current study has been performed on a 16-ft Tracker boat shown in Fig. 4-4. Both throttle and steering mechanisms to allow for a fully autonomous operation of the boat have been built in-house. The drives in both mechanisms have been chosen to be compact 12 V DC servomotors with planetary gearheads. The angular displacements of the throttle arm and the steering wheel are measured by optical encoders mounted on the motor shaft of their respective drive. The combination of optical encoders and gearheads has allowed the angular displacements of the throttle arm and the steering wheel to be measured with a very high resolution. The controllers, observers, 24-bit up/down counters, ADC and DAC converters are run from the dSPACE1005 module. Figure 4-5 depicts a block diagram of the entire system illustrating the interactions between the various components of the system.

The feedback signals for the controllers and observers are the optical encoders, the gyro compass system (Cloud Cap Technology, Crista IMU), and the Hemisphere V101 Compass Global Positioning System (GPS) receiver (see Fig. 4-5). The GPS data has been converted to Universal Transverse Mercator (UTM) coordinates (Kawase, 2012). The reader is referred to Table 4-1 for the manufacturer, model number, and resolution of the various components that are used in the experimental set-up.

Fig. 4-4. Sixteen feet Tracker boat

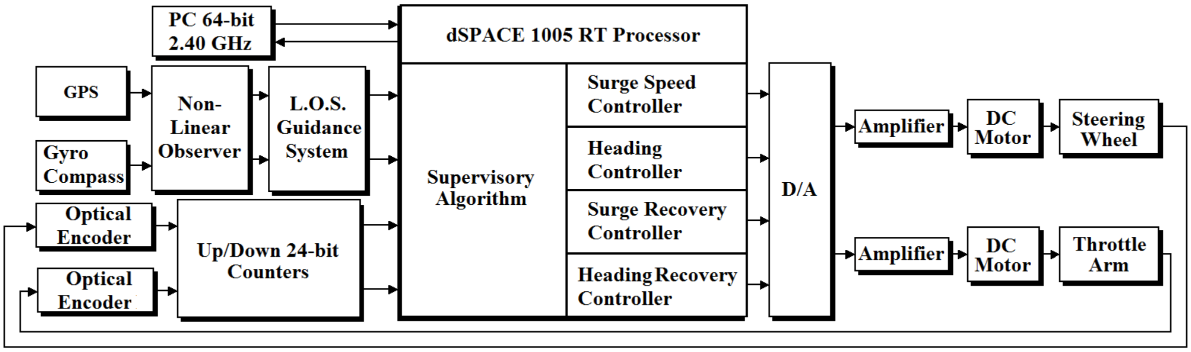

Fig. 4-5. Block diagram of the experimental apparatus

Throttle & Steering Assemblies			
Type	**Maker**	**Model**	**Specs**
DC Servo Motors	Faulhaber	3564 K 012 B	Brushless 12V
Optical Encoders	Faulhaber	HEDS5500C06	100 pulses/rev
Planetary Gearheads	Faulhaber	38/2	Reduction Ratio 415:1
Servo Amplifier	Advanced Motion Controls	B15A8	±10V Analog DC Drive
Resolution	n/a	n/a	0.008675°/pulse

Table 4-1. Experimental set-up specifications

4.4 Performance Assessment of the STO and SMO in Marine Applications

The experimental set-up described in the previous Section has been used in the validation of both STO and SMO. The supervisory algorithm was used to perform prescribed throttle angle and steering control tasks. The SMO was used on-line to estimate the state variables that are needed for the computation of the control signals. Furthermore, the SFO was also used to estimate the state variables during the same experiments in order to ensure that both observers are performing the estimation under the same operating and environmental conditions. The parameters of the STO and SMO are listed in Tables 4-2 and 4-3.

STO Parameters	
$\eta_{o_i} \quad j = 1, \cdots, 3$	0.00001
$\hat{f}_{o_{i+3}} \quad i = 1, \cdots, 3$	0
$\left\| \tilde{x}_{o_{i+3}} \right\|_{upper\ bound} \quad i = 1, \cdots, 3$	0.001
$F_{o_{i+3}} \quad i = 1, \cdots, 3$	0.0001
$\phi_{o_i} \quad i = 1, \cdots, 3$	0.0001

Table 4-2. Self Tuning observer parameters

SMO Parameters	
$\eta_{o_i} \quad j = 1, \cdots, 3$	0.01
$\hat{f}_{o_{i+3}} \quad i = 1, \cdots, 3$	0
$\left\| \tilde{x}_{o_{i+3}} \right\|_{upper\ bound} \quad i = 1, \cdots, 3$	0.1
$\left\| \tilde{x}_{o_{i+3}} \right\|_{desired\_accuracy} \quad i = 1, \cdots, 3$	0.001
$F_{o_{i+3}} \quad i = 1, \cdots, 3$	0.3
$\phi_{o_i} \quad i = 1, \cdots, 3$	0.001

Table 4-3. Sliding mode observer parameters

The estimation results are shown in Figs. 4-6 to 4-11. Figures 4-6 and 4-7 illustrate the measured and estimated X- and Y-coordinates of the boat. Note the high accuracy of the estimated displacements in spite of the fact that all $\hat{f}_{o_{j+3}}$ for $j = 1,\cdots,3$ terms have been set to zero (see Tables 4-2 and 4-3).

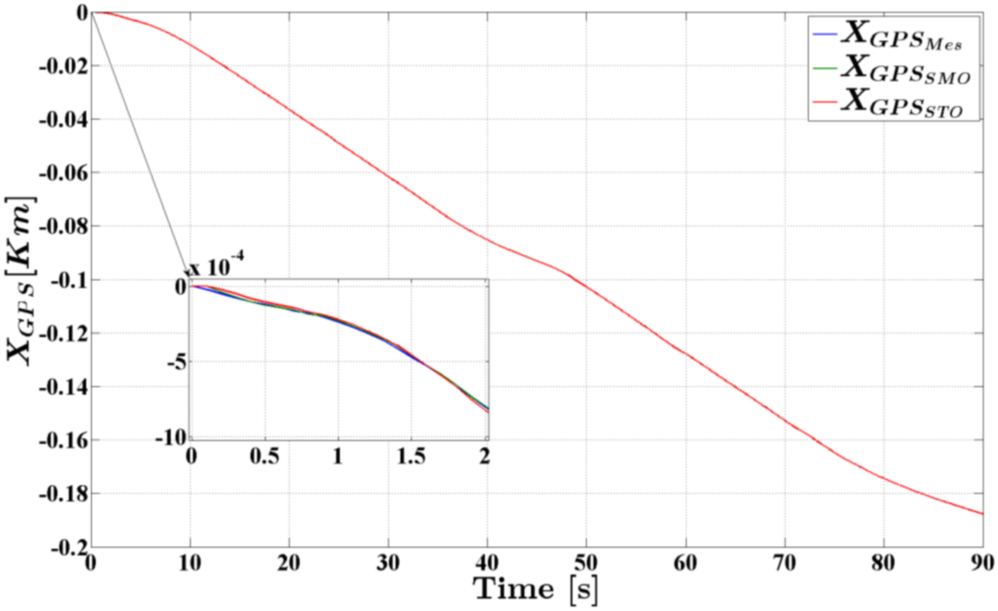

Fig. 4-6. Measured and estimated X-coordinate of the boat position

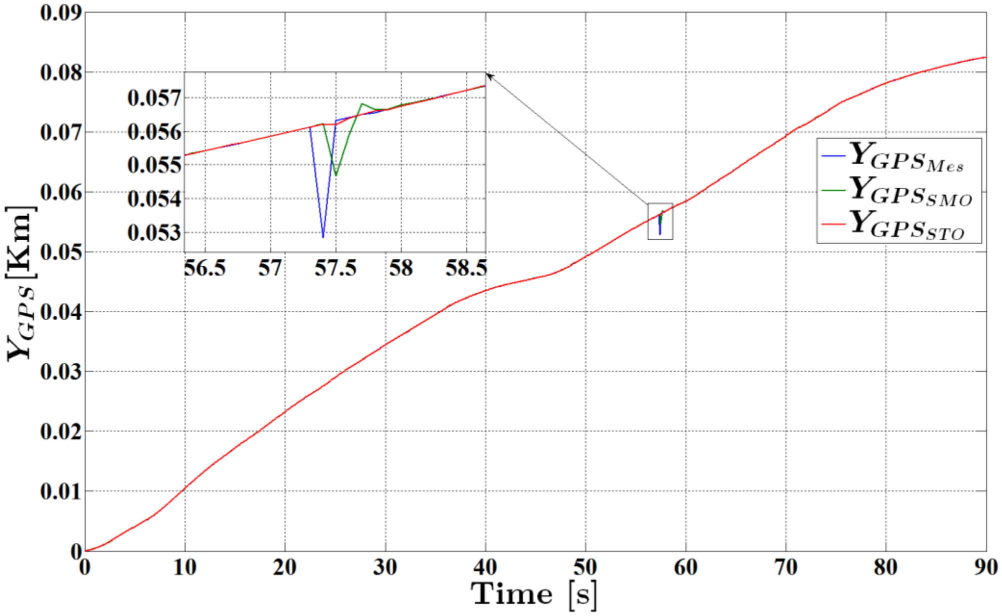

Fig. 4-7. Measured and estimated Y-coordinate of the boat position

Also note that the signal of the gyro compass system represents the time derivative of the yaw angle. Therefore, this signal had to be integrated with respect to time in order to yield the actual yaw angle. Figure 4-8 shows the actual and estimated yaw angle of the boat. The observers have yielded similar high level of accuracy in the estimation of the yaw angle. However, on a closer look, one can realize that the STO estimate is much smoother than that of the SMO. This effect is very clear in the $\dot{X}$ and $\dot{Y}$ estimates in Figs. 4-9, 4-10a, and 4-10b. Fig. 4-9 reveals that the SMO is sensitive to spikes in the original signal that may be induced by noise. On the contrary, the STO is somewhat immune to these spikes. This is because its built-in learning and self-tuning process cannot instantaneously update the observer parameters and needs a certain amount of time to adjust to the abrupt changes in the actual signal. This effect is also greatly shown in Figs. 4-10a and 4-10b, which reveal that the STO was totally immune to the freak spikes in the actual signal. However, the SMO is shown to be susceptible to such spikes, which are reflected in the estimated state variables. Moreover, Fig. 4-11 illustrates a very slight phase lag between the actual and estimated time rate of change of the yaw angle.

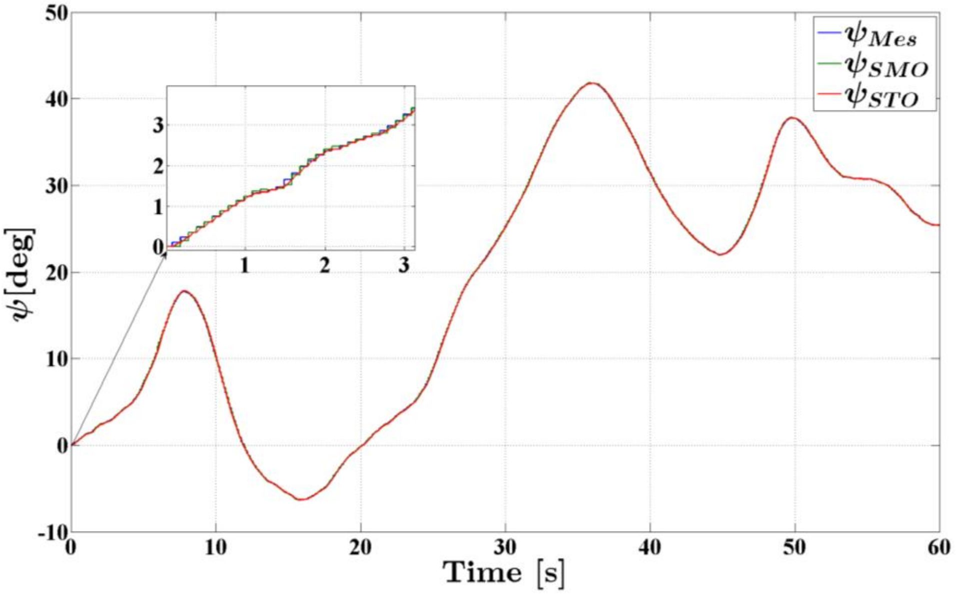

Fig. 4-8. Integrated and estimated yaw angle of the boat position

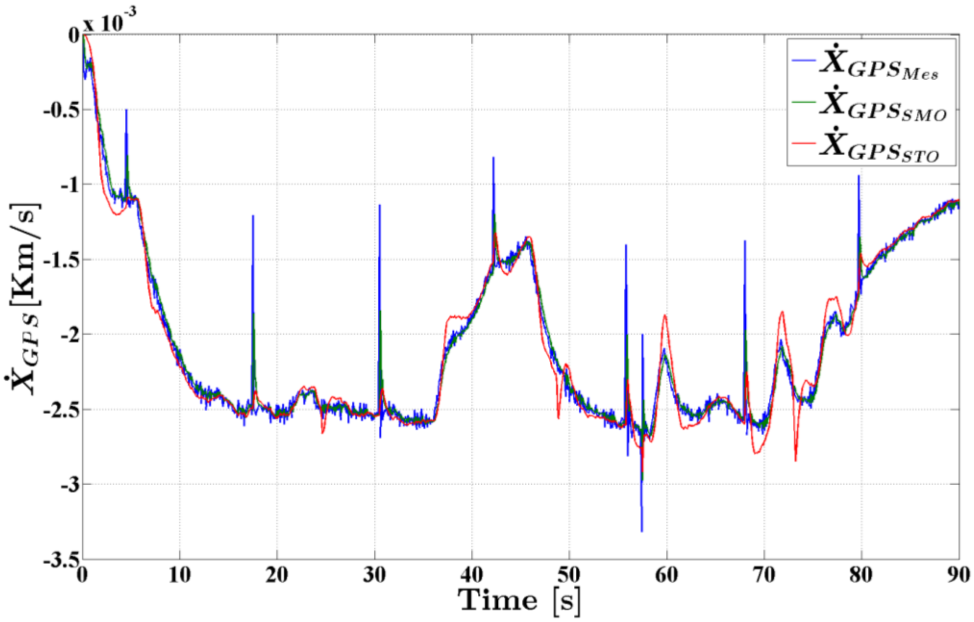

Fig. 4-9. $\dot{X}$ velocity component of the boat

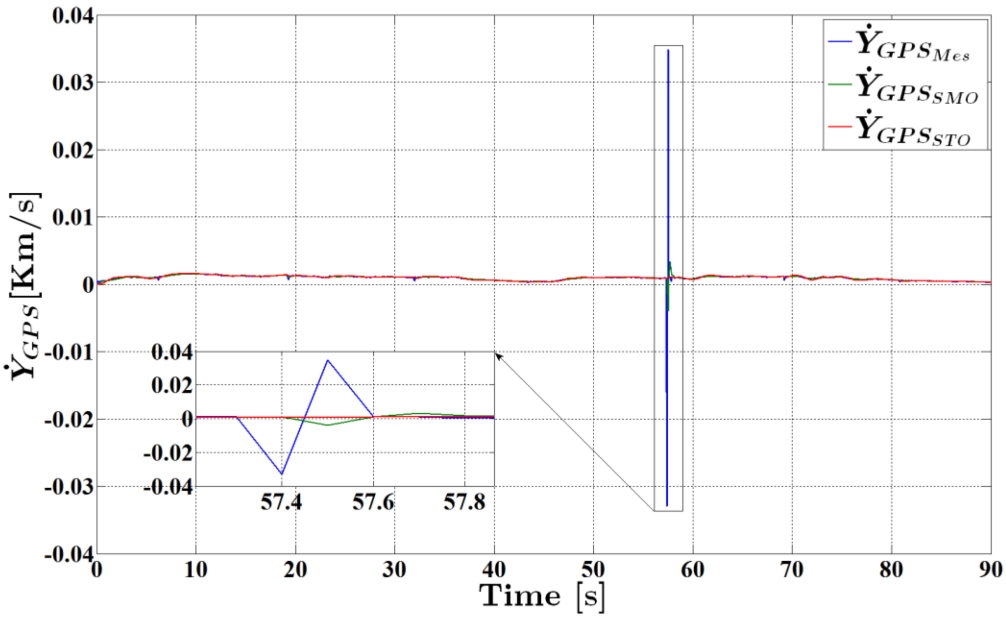

Fig. 4-10a. $\dot{Y}$ velocity component of the boat

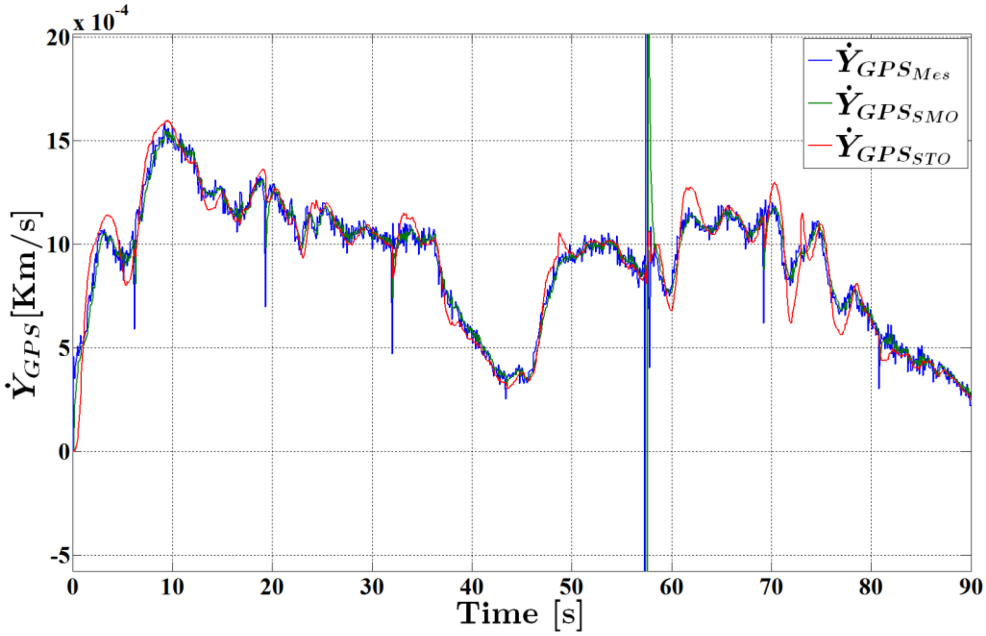

Fig. 4-10b. $\dot{Y}$ velocity component of the boat

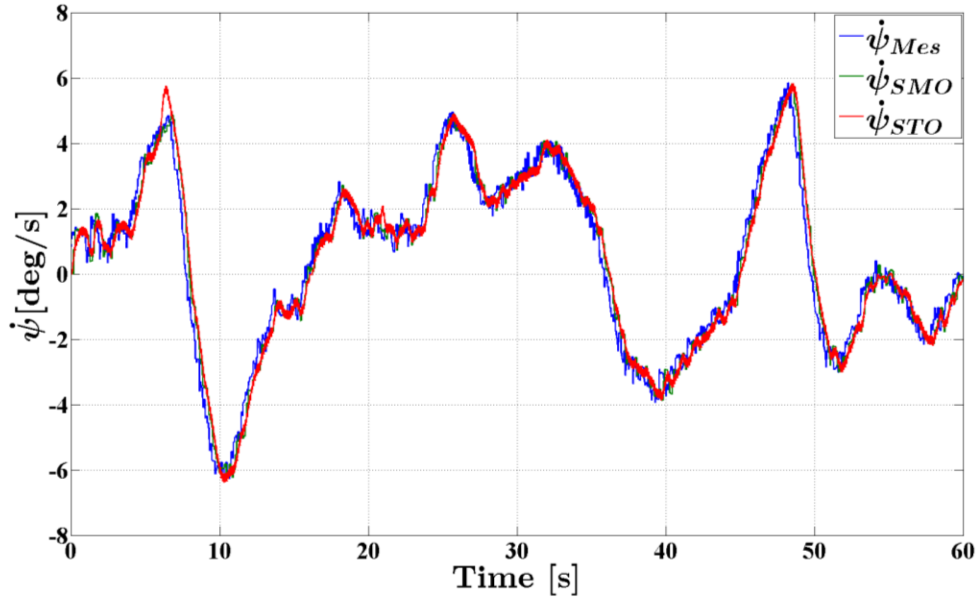

Fig. 4-11. Time rate of change of the yaw angle of the boat

4.5 Summary

The hybrid control strategy used in the fully autonomous operation of the marine surface vessel has been covered in this Chapter. This strategy integrates the controllers with the guidance system in order to empower under-actuated marine vessels to accurately track a desired trajectory. The guidance system will provide the heading controller with the desired yaw angle that is required to point the boat in the right direction while reducing the cross track error; thus, enabling the controller to compensate for both heading angle and sway motion with one control signal. As a result, the ship tracking problem is now reduced to surge speed and heading tasks for which two control variables are readily available.

The hybrid control strategy encompasses five controllers that are managed by a main supervisory algorithm. Two of these controllers are devoted for tracking and maneuvering operations of the vessel based on the boat's actual surge speed and heading angle. Two other controllers provide the user with the option of performing either point-to-point (PTP) or prescribed throttle arm and steering angles. The feedback signals for PTP controllers are obtained from the optical encoders of their respective servomotors while the tracking of prescribed throttle arm and steering angles relies on the boat's actual surge speed and heading angle. The fifth controller is a recovery controller, which is only activated in case of emergencies. The supervisory algorithm synchronizes the functioning of these controllers to successfully track a desired trajectory while ensuring a safe operation of the marine vessel.

The formulations pertaining to the five controllers are presented in great detail in this Chapter. In addition, the derivations of self-tuning and sliding mode observers are also included. These observers have been used herein to provide accurate estimates of the state variables that are needed for the implementation of the controllers.

In assessing the performance of both STO and SMO, the experimental work was conducted on a marine surface vessel operating in open-water. The prescribed throttle arm and steering angle controllers have been implemented herein based on estimated rather than measured state variables. The experimental results have demonstrated the capabilities of both STO and SMO in rapidly converging and accurately estimating the state variables in spite of significant modeling imprecision and external disturbances. However, the results have revealed that the STO estimation is smoother than that of the SMO and significantly less prone to large spikes in the actual signals, which may be induced by measurement noise.

CHAPTER 5 SUMMARY AND CONCLUSIONS

The current work is summarized in this Chapter. In addition, the main conclusions and contributions are highlighted. Furthermore, prospective research topics for advancing the current effort are suggested.

5.1 Objectives

The objectives of the current study are:

- Examine the adverse effects of non-collocated sensors and actuators on the performance of structural controllers.
- Develop remedial actions to make structural controllers immune to the adverse effects of non-collocated sensors and actuators.
- Provide experimental validation for the robust performance of a self-tuning nonlinear observer and a sliding mode observer in accurately estimating the state variables of structures whose natural frequencies are configuration-dependent.
- Use the estimated state variables in the computation of control signals for a marine surface vessel whose dynamics are not known and its operating conditions are constantly varying with considerable environmental disturbances. These tests were conducted on a 16-ft boat operating in open-water.

5.2 Summary of the Work

The adverse effects of non-collocated sensors and actuators on the phase characteristics of flexible structures and the ensuing implications on the performance of structural controllers have been investigated. This effort builds on the work done by Spector and Flashner (1990) and explores remedial schemes, based on the phase angle contour of the system, to enhance the capabilities of structural controllers in order to ensure a desirable and robust performance of the closed-loop system irrespective of the sensor location with respect to the actuator.

Two closed-loop systems have been considered in Chapter 2. The first one consists of a pinned-free flexible beam with the control torque applied at the pinned-end. The second one is a clamped-free deformable beam with the control moment generated by two piezoelectric actuators bonded at the top and bottom surfaces near the clamped-end. The assumed modes method was implemented to approximate the structural deformations of the deformable beams.

Phase angle contours for both systems have been generated as functions of the normalized sensor location and the excitation frequency. They illustrate the loci of the imaginary open-loop zeros along with the resulting minimum and non-minimum phase regions of the systems as the sensors sweep the entire span of the beams.

Two structural controllers have been implemented to actively attenuate the undesired in-plane transverse deformation of the pinned-free beam. The controllers are designed based on the sliding mode methodology and the active damping control strategy. Their formulations have been enhanced in order to reduce their sensitivity to variations in the sensor’s relative location with respect to the actuator. This was done by incorporating the phase angle contour information into the design of the sliding mode controller (SMC). As for the active damping controller, the shapes of the elastic modes were accounted for in the gains of the controller. The simulation results have identified three distinct regions for the sensor’s location whereby the performance of the sliding mode controller can be stable, unstable, or stable with a remedial action. They also revealed that the SMC tends to eliminate the overall in-plane transverse deformation at the sensor location by having the sustained oscillation of the first elastic mode to be equal in magnitude and opposite in sign to that of the second elastic mode. However, the results have shown that the modified active damping controller eliminates the overall in-plane transverse deformation by both active damping and having the elastic modes equal in magnitude and opposite in sign. The dissipative nature of this controller prevents the beam from preserving its strain energy, which causes the unwanted vibrations to decay down to zero with time. In addition, the dependence of the controller gains on the mode shapes has enabled the proposed active damping controller to yield a stable response of the beam irrespective of the sensor location.

Chapter 3 provides the very much needed experimental validation for the performances of the robust nonlinear observers that have recently been appearing in the literature. Two nonlinear observers have been considered. The first one is a self-tuning observer while the second one is a sliding mode observer. The results discussed in Chapter 3 are generated in a controlled laboratory setting on a spherical robotic manipulator where only the protruding portion of the third link from the second link is considered to be flexible. The challenges brought about by a spherical robotic manipulator stem from the prismatic joint, which causes the natural frequencies of the structure to be configuration-dependent.

The STO design is based on both the variable structure systems theory and the self-tuning fuzzy logic scheme (Khaled and Chalhoub, 2014). Its robustness and self-tuning characteristic allow one to use an imprecise model of the system and eliminate the need for the extensive tuning associated with a fixed rule-based expert fuzzy inference system. Chapter 3 also covers the formulation of the sliding mode observer, which is solely based on the variable structure systems theory.

Both observers have been implemented to estimate the generalized coordinates of the flexible motion under two different types of excitation. The first one involves disturbances in the initial conditions or the use of initial impulsive forces. While in the second type of excitation, the structural deformations are induced by the rigid body motion of the arm during its tracking maneuver of a straight line in the work envelope of the robot. A basic sliding mode controller has been implemented to control the rigid body degrees of freedom of the robot during the tracking maneuver.

Same parameters of the observers have been used in generating both theoretical and experimental data. The results confirm the robustness of both observers in accurately estimating the generalized coordinates of the flexible motion of the third link in spite of significant structured and unstructured uncertainties. Moreover, the performances of STO and SMO have been found to be comparable in terms of rapid convergence and accuracy of the estimated state variables.

Chapter 4 focuses on the estimation of state variables in an uncontrolled environment, the reliance on estimated rather than measured state variables for the computation of the control signals, and the development of a supervisory control algorithm for an under-actuated marine surface vessel.

The experimental results discussed in Chapter 4 are generated on a 16-ft boat operating in open-water. The dynamics of the boat are assumed to be completely unknown and the environmental disturbances are considered to be random in nature and magnitude. Therefore, the controllers and observers used in this Chapter are formulated by totally ignoring the system's dynamics.

The objective of the supervisory control algorithm is to ensure synchronized operation of all system components. At its highest level, the supervisory code provides the user with the capability of invoking the "recovery" controller should any unforeseen emergency situation arises. Furthermore, it allows the user to select PTP controllers, prescribed throttle arm and heading angle controllers, or tracking controllers for either the surge speed or the vessel's heading control tasks; thus, rendering the code as versatile as possible. The supervisory control algorithm has been employed in this work to perform prescribed throttle arm and steering angle control tasks based on feedback signals from GPS and gyro compass systems. However, the transducers do not provide all the state variables needed for the computation of the control signals. Therefore, both STO and SMO were relied on to estimate the required state variables.

Both the self-tuning and sliding mode observers have been reformulated to make them applicable for maritime applications. The observers have been implemented to estimate the time derivatives of X and Y coordinates of the boat from the GPS data along with the heading angle and its time derivative from the gyro compass data.

The experimental validation of the observers have been conducted by relying on the SMO to provide on-line estimates of the state variables that are required by the supervisory algorithm to perform prescribed throttle angle and steering control tasks. During the same tests, the SFO was also used to estimate the required state variables in order to ensure that both observers are operating under exact same operating and environmental conditions.

The experimental results have demonstrated the capabilities of both STO and SMO in rapidly converging and accurately estimating the state variables in spite of ignoring the system’s dynamics and in the presence of unpredictable environmental disturbances. However, the results have revealed that the STO estimation is smoother than that of the SMO and significantly less prone to large spikes in the actual signals, which may be induced by measurement noise.

5.3 Main Contributions of the Current Work

The main contributions of the current study are:

- Phase angle contours have been generated for pinned-free and clamped-free beams as functions of the normalized sensor location and the excitation frequency. These contours reveal the nodal lines and identify minimum and non-minimum phase regions pertaining to each system. They also illustrate the changes in the pole-zero patterns of the systems as the sensor location is varied along the entire span of the beam.
- An in depth analysis has been provided to demonstrate the differences and vulnerability of the SMC and the active damping controller in attenuating the undesired vibrations of a pinned-free beam.
- Remedial actions have been proposed and proven successful, in simulation studies, to enable both SMC and the active damping controller in yielding stable response of the pinned-free beam irrespective of the sensor location with respect to the actuator.
- Although many theoretical studies have been reported in the literature regarding novel designs of nonlinear robust observers, experimental validation of these observers have been significantly lagging the theoretical development. The current study addresses this problem by providing experimental validation of a self-tuning observer and a sliding mode observer

(Khaled and Chalhoub, 2014) on a very challenging system whose natural frequencies are configuration-dependent. The capability of the observers in yielding accurate estimation of the required state variables has been experimentally validated in the presence of considerable structured and unstructured uncertainties.

- A new scheme has been introduced to extract information pertaining to many elastic modes of a flexible structure from the signal of a single transducer.
- Experimental validation of STO and SMO in a completely uncontrolled environment on a marine vessel operating in open-water. This was made possible through the development of a supervisory control algorithm that encompasses a guidance system, two types of nonlinear observers along with different control schemes to perform PTP tasks, prescribed throttle arm and steering tasks, surge speed and heading tracking tasks, or recovery maneuvers.
- Use of the supervisory control algorithm to perform prescribed throttle arm and steering control tasks based on estimated state variables that have been determined by STO and SMO from GPS and gyro compass feedback signals. The experimental results have demonstrated that both STO and SMO are capable of yielding accurate estimates of the state variables in spite of ignoring the system's dynamics and in the presence of unpredictable environmental disturbances.

5.4 Future Research Topics

The main steps need to be experimentally validated:

- Use the supervisory control algorithm to perform a desired trajectory tracking task, which would involve coupling the guidance system with the tracking controllers and observers.
- Development of a scheme to prevent the tracking controller from compensating for heading errors induced by waves or sea currents
- Development of a path planning algorithm to avoid static and/or dynamic obstacles for marine vessels.

APPENDIX A

PINNED-FREE BEAM FORMULATION

The A_{PF} and B_{PF} matrices of Eq. (2-8), corresponding to the special case of $n = 2$, can be expressed as

$$A_{PF} = \begin{bmatrix} 0 & 0 & 1 & 0 \\ 0 & 0 & 0 & 1 \\ a_{PF_{31}} & a_{PF_{32}} & a_{PF_{33}} & a_{PF_{34}} \\ a_{PF_{41}} & a_{PF_{42}} & a_{PF_{43}} & a_{PF_{44}} \end{bmatrix} \quad \text{and} \quad B_{PF} = \begin{bmatrix} 0 \\ 0 \\ \dfrac{-5.4}{\rho A L^2} \\ \dfrac{10.01}{\rho A L^2} \end{bmatrix}$$

where

$$a_{PF_{31}} = -\frac{237.721EI}{\rho AL^4} \qquad a_{PF_{32}} = -\frac{0.00143EI}{\rho AL^4}$$

$$a_{PF_{33}} = -\frac{c_1}{\rho AL} \qquad a_{PF_{34}} = -\frac{4.28886\times10^{-7}c_2}{\rho AL}$$

$$a_{PF_{41}} = -\frac{0.000461EI}{\rho AL^4} \qquad a_{PF_{42}} = -\frac{2496.48EI}{\rho AL^4}$$

$$a_{PF_{43}} = -\frac{4.28886\times10^{-7}c_1}{\rho AL} \qquad a_{PF_{44}} = -\frac{c_2}{\rho AL}$$

The coefficients of the transfer function in Eq. (2-10) are defined as

$$\bar{a}_1\left(x^*\right) = AL^6\rho\left[-5.4\,\Phi_{PF_1}\left(x^*\right) + 10.01\,\Phi_{PF_2}\left(x^*\right)\right]$$

$$\bar{a}_2\left(x^*\right) = L^5\left[-5.4\,c_2\Phi_{PF_1}\left(x^*\right) + 10.01c_1\Phi_{PF_2}\left(x^*\right)\right]$$

$$\bar{a}_3\left(x^*\right) = EIL^2\left[-13482\,\Phi_{PF_1}\left(x^*\right) + 2379.24\,\Phi_{PF_2}\left(x^*\right)\right]$$

$$\overline{b_1} = A^2 L^8 \rho^2$$

$$\overline{b_2} = AL^7 \rho \left[c_1 + c_2 \right]$$

$$\overline{b_3} = 2734.21 AL^4 EI \rho + L^6 c_1 c_2$$

$$\overline{b_4} = EIL^3 \left[2496.49\, c_1 + 237.722\, c_2 \right]$$

$$\overline{b_5} = 593466 E^2 I^2$$

APPENDIX B

CLAMPED-FREE BEAM FORMULATION

The A_{CF} and B_{CF} matrices of Eq. (2-14), corresponding to the special case of $n = 2$, can be expressed as

$$A_{CF} = \begin{bmatrix} 0 & 0 & 1 & 0 \\ 0 & 0 & 0 & 1 \\ a_{CF_{31}} & a_{CF_{32}} & a_{CF_{33}} & a_{CF_{34}} \\ a_{CF_{41}} & a_{CF_{42}} & a_{CF_{43}} & a_{CF_{44}} \end{bmatrix}$$

$$B_{CF} = \begin{bmatrix} 0 \\ 0 \\ \dfrac{d_{31} K_f EI \left[\left(\Phi'_{CF_1}(x_1) - \Phi'_{CF_1}(x_2) \right) - 1.495 \times 10^{-5} \left(\Phi'_{CF_2}(x_1) - \Phi'_{CF_2}(x_2) \right) \right]}{\rho AL\, h_{pe}} \\ \dfrac{d_{31} K_f EI \left[-1.495 \times 10^{-5} \left(\Phi'_{CF_1}(x_1) - \Phi'_{CF_1}(x_2) \right) + \left(\Phi'_{CF_2}(x_1) - \Phi'_{CF_2}(x_2) \right) \right]}{\rho AL\, h_{pe}} \end{bmatrix}$$

where

$$a_{CF_{31}} = -\frac{12.3624 EI}{\rho AL^4} \qquad a_{CF_{32}} = \frac{0.0070735 EI}{\rho AL^4}$$

$$a_{CF_{33}} = -\frac{c_1}{\rho AL} \qquad a_{CF_{34}} = \frac{1.495 \times 10^{-5} c_2}{\rho AL}$$

$$a_{CF_{41}} = \frac{5.3786 \times 10^{-7} EI}{\rho AL^4} \qquad a_{CF_{42}} = -\frac{485.519 EI}{\rho AL^4}$$

$$a_{CF_{43}} = \frac{1.495 \times 10^{-5} c_1}{\rho AL} \qquad a_{CF_{44}} = -\frac{c_2}{\rho AL}$$

The coefficients of the transfer function in Eq. (2-16) are defined as

$$\bar{\bar{a}}_1\left(x^*\right)=d_{31}K_f\,\rho AEIL^7\left\{\left[\left(\Phi'_{CF_1}\left(x_1\right)-\Phi'_{CF_1}\left(x_2\right)\right)\right.\right.$$

$$\left.-1.495\times10^{-5}\left(\Phi'_{CF_2}\left(x_1\right)-\Phi'_{CF_2}\left(x_2\right)\right)\right]\Phi_{CF_1}\left(x^*\right)$$

$$+\left[-1.495\times10^{-5}\left(\Phi'_{CF_1}\left(x_1\right)-\Phi'_{CF_1}\left(x_2\right)\right)\right.$$

$$\left.\left.+\left(\Phi'_{CF_2}\left(x_1\right)-\Phi'_{CF_2}\left(x_2\right)\right)\right]\Phi_{CF_2}\left(x^*\right)\right\}$$

$$\bar{\bar{a}}_2\left(x^*\right)=d_{31}K_f\,EIL^6\left\{\left(\Phi'_{CF_1}\left(x_1\right)-\Phi'_{CF_1}\left(x_2\right)\right)c_2\,\Phi_{CF_1}\left(x^*\right)\right.$$

$$\left.+\left(\Phi'_{CF_2}\left(x_1\right)-\Phi'_{CF_2}\left(x_2\right)\right)c_1\,\Phi_{CF_2}\left(x^*\right)\right\}$$

$$\bar{\bar{a}}_3\left(x\right)=d_{31}K_f\,E^2I^2L^3\left\{\left[485.519\left(\Phi'_{CF_1}\left(x_1\right)-\Phi'_{CF_1}\left(x_2\right)\right)\right.\right.$$

$$\left.-1.84262\times10^{-4}\left(\Phi'_{CF_2}\left(x_1\right)-\Phi'_{CF_2}\left(x_2\right)\right)\right]\Phi_{CF_1}\left(x^*\right)$$

$$+\left[-1.84262\times10^{-4}\left(\Phi'_{CF_1}\left(x_1\right)-\Phi'_{CF_1}\left(x_2\right)\right)\right.$$

$$\left.\left.+12.3625\left(\Phi'_{CF_2}\left(x_1\right)-\Phi'_{CF_2}\left(x_2\right)\right)\right]\Phi_{CF_2}\left(x^*\right)\right\}$$

$$\bar{\bar{b}}_1=A^2L^8\rho^2h_{pe}$$

$$\bar{\bar{b}}_2=AL^7\rho\,h_{pe}\left[c_1+c_2\right]$$

$$\bar{\bar{b}}_3=h_{pe}\left(497.881AL^4EI\rho+L^6c_1\,c_2\right)$$

$$\bar{\bar{b}}_4=EIL^3h_{pe}\left[485.519\,c_1+12.3625\,c_2\right]$$

$$\bar{\bar{b}}_5=6002.16E^2I^2h_{pe}$$

REFERENCES

[1] Aamo, O. M. and Fossen, T. I., 1999, “Controlling Line Tension in Thruster Assisted Mooring Systems”, IEEE International Conference on Control Applications (CCA’99), Honolulu, Hawaii, 1104-1109.

[2] Ahmed-Ali, T. and Lamnabhi-Lagarrigue, F., 1999, “Sliding Observer-Controller Design for Uncertain Triangular Nonlinear Systems”, IEEE Transactions on Automatic Control, 44(6), 1244-1249.

[3] Anderson, B.D.O. and Moore, J.B., 1990, Optimal control: linear quadratic methods, Prentice-Hall, Englewood Cliffs, New Jersey.

[4] Aranda, J., De La Cruz, J.M., Diaz, J.M., and Dormido Canto, S., 2002, “QFT Versus Classical Gain Scheduling: Study for a Fast Ferry”, 15th IFAC World Congress.

[5] Balchen, J. G., Jenssen, N. A., Mathisen, E. and Sælid, S., 1980, “A Dynamic Positioning System Based on Kalman Filtering and Optimal Control”, Modeling Identification and Control, 1(3), 135-163.

[6] Banks, S. P., 1981, “A Note on Non-Linear Observers”, International Journal of Control, 34, 185-190.

[7] Baumann, W.T. and Rugh, W.J., 1986, “Feedback Control of Nonlinear Systems by Extended Linearization”, IEEE Transactions on Automatic Control, AC-31(1).

[8] Bazzi, B.A. and Chalhoub, N.G., 2005, "Fuzzy-Sliding Mode Controller for a Flexible Single-Link Robotic Manipulator", Journal of Vibration and Control, 11(2), 295-314.

[9] Benchaib, A. and Rachid, A., 1999, "Real-Time Sliding-Mode Observer and Control of an Induction Motor", IEEE Transactions on Industrial Electronics, 46(1), 128-137.

[10] Berge, S.P., Ohtsu, K., Fossen, T.I., 1998, "Nonlinear Control of Ships Minimizing the Position Tracking Errors", Proceedings of the IFAC Conference on Control Applications in Marine Systems (CAMS'98), Fukuoka, Japan, 141-147.

[11] Besancon, G., 1999, "On Output Transformations for State Linearization Up to Output Injection", IEEE Transactions on Automatic Control, 44, 1975-1981.

[12] Book, W.J., Maizza-Neto, O. and Whitney, D.E., 1975, "Feedback Control of Two Beams, Two Joint Systems With Distributed Flexibility", ASME Journal of Dynamic Systems, Measurement and Control, 97(4), 424-431.

[13] Boyd, S., El Ghaoui, L., Feron, E. and Balakrishnan, V., 1994, "Linear Matrix Inequalities in System and Control Theory", Studies in Applied Mathematics Vol. 15, Philadelphia, PA.

[14] Breivik, M., 2003, "Nonlinear Maneuvering Control of Underactuated Ships", Master's Thesis, Norwegian University of Science and Technology, Norway.

[15] Breivik, M., Strand, J. P. and Fossen, T. I., 2006, “Guided Dynamic Positioning for Marine Surface Vessels”, IFAC Conference on Manoeuvring and Control of Marine Craft (MCMC'06), Lisbon, Portugal, September 20-22.

[16] Cannon, R.H. and Schmitz, E., 1984, “Initial Experiments on the End-Point Control of a Flexible One-Link Robot”, International Journal of Robotics Research, 3(3), 62-75.

[17] Cannon, R.H. Jr. and Rosenthal, D.E., 1984, “Experiments in Control of Flexible Structures with Noncolocated Sensors and Actuators”, Journal of Guidance, Control and Dynamics, 7(5), 546-553.

[18] Canudas De Wit, C. and Slotine, J.J.E., 1991, “Sliding Observers for Robot Manipulators”, Automatica 27(5), 859–864.

[19] Chalhoub, N.G. and Chen, L., 1998, “A Structural Flexibility Transformation Matrix for Modelling Open-Kinematic Chains with Revolute and Prismatic Joints”, Journal of Sound and Vibration, 218(1): 45-63.

[20] Chalhoub, N.G. and Kfoury, G.A., 2005, “Development of a Robust Nonlinear Observer for a Single-Link Flexible Manipulator”, Nonlinear Dynamics, 39(3), 217–233.

[21] Chalhoub, N.G. and Zhang, X., 1993 “Reduction of the End Effector Sensitivity to the Structural Deflections of a Single Flexible Link: Theoretical and Experimental Results”, ASME Journal of Dynamic Systems, Measurement and Control, 115(4), 658-666.

[22] Chalhoub, N.G. and Khaled, N., 2009, “Robust Controller and Observer for Marine Surface Vessels”, 2009 Conference on Grand Challenges in Modeling and Simulation (GCMS’09), July 13-16, 2009, Istanbul, Turkey.

[23] Chalhoub, N.G. and Khaled, N., 2014, “Integrated Controller-Observer System for Marine Surface Vessels”, Journal of Vibration and Control, 20(3), 381-394.

[24] Chalhoub, N.G., Kfoury, G.A. and Bazzi, B.A., 2006, “Design of Robust Controllers and a Nonlinear Observer for the Control of a Single-Link Flexible Robotic Manipulator”, Journal of Sound and Vibration, 291(1-2), 437-461.

[25] Chaoui, H. and Sicard, P., 2012, “Adaptive Fuzzy Logic Control of Permanent Magnet Synchronous Machines with Nonlinear Friction”, IEEE Transactions on Industrial Electronics, 59(2), 1123-1133.

[26] Chen, L. and Chalhoub, N.G., 1997 “Modeling and Control of Transverse and Torsional Vibrations in a Spherical Robotic Manipulator: Theoretical and Experimental Results”, ASME Journal of Dynamic Systems, Measurement and Control, 119(3), 421-430.

[27] Chen, C. T., 1970, Introduction to Linear Systems Theory, Holt, Rinehart and Winston.

[28] Chih-Hsun, C. and Hung-Ching, L., 1994, “A Heuristic Self-tuning Fuzzy Controller”, Fuzzy Sets and Systems, 61(3), 249-264.

[29] Cho, Y. M. and Rajamani, R., 1997, “A Systematic Approach to Adaptive Observer Synthesis for Nonlinear Systems”, IEEE Transactions on Automatic Control, 42(4), 534-537.

[30] Chodavarapu, P.A. and Spong, M.W., 1996, “On Noncollocated Control of a Single Flexible Link”. IEEE International Conference on Robotics and Automation, Minneapolis, Minnesota, April 22-28, 2:1101-1106.

[31] Choi, S.B., Cheong, C.C. and Shin, H.C., 1995, “Sliding Mode Control of Vibration in a Single-Link Flexible Arm with Parameter Variations”, Journal of Sound and Vibration, 179(5), 737-748.

[32] Choi, S. B., Park, D. W., and Jayasuriya, S., 1994, “A Time-Varying Sliding Surface for Fast and Robust Tracking Control of Second-Order Uncertain Systems”, Automatica, 30(5), 899–904.

[33] Choi, S.B. and Kim, J.S., 1997, “A Fuzzy-Sliding Mode Controller for Robust Tracking of Robotic Manipulators”, Mechatronics 7, 199–216.

[34] Cimen, T., Banks, S.P., 2004, “Nonlinear Optimal Tracking Control with Application to Super-Tankers for Autopilot Design”, Automatica, 40(11), 1845-1863.

[35] Crawley, E.F. and De Luis, J., 1987, “Use of Piezoelectric Actuators as Elements of Intelligent Structures”, American Institute of Aeronautics and Astronautics Journal, 25(10), 1373-1385.

[36] Denavit, J. and Hartenberg, R.S., 1955, “A Kinematic Notation for Lower-Pair Mechanisms Based on Matrices”, ASME Journal of Applied Mechanics, 22(2), 215-221.

[37] Derrett, D. R. and Barrass, C. B., 1999, Ship Stability for Masters and Mates, 5th edition, Butterworth-Heinemann, Imprint of Elsevier.

[38] Do, K. D., Jiang, Z. P. and Pan, J., 2005, “Global Partial-State Feedback and Output-Feedback Tracking Controllers for Underactuated Ships”, Systems and Control Letters, 54(10), 1015-1036.

[39] Do, K. D., Pan, J., Jiang, Z. P., 2003, “Robust Adaptive Control of Underactuated Ships on a Linear Course with Comfort”, Ocean Engineering, 30(17), 2201-2225.

[40] Drakunov, S.V., 1983, “Adaptive Quasioptimal Filter with Discontinuous Parameters”, Automation and Remote Control, 44(9), 1167–1175.

[41] Drakunov, S.V. and Utkin, V., 1995, “Sliding Mode Observers: Tutorial”, Proceedings of the 34th IEEE Conference on Decision and Control (CDC), December 13-15, New Orleans, LA, 3376–3378.

[42] Falzarano, J. M. and Lakhotia, C., 2008, “Effect of Icing on Ship Maneuvering Characteristics”, The 27th International Conference on Offshore Mechanics and Arctic Engineering (OMAE2008), June 15–20, Estoril, Portugal, 997-1001.

[43] Fleming, F.M. and Crawley, E.F., 1991, “The Zeroes of Controlled Structures: Sensor/Actuator Attributes and Structural Modeling”,

Proceedings of the 32nd Structures, Structural dynamics, and Materials Conference, Baltimore, Maryland, 1, 1806-1816.

[44] Forbes, J.R. and Damaren, C.J., 2012, "Single-Link Flexible Manipulator Control Accommodating Passivity Violations: Theory and Experiments", IEEE Transactions on Control Systems Technology, 20(3), 652-662.

[45] Fossen, T. I., 2002, "Marine Control Systems: Guidance, Navigation and Control of Ships, Rigs and Underwater Vehicles", Marine Cybernetics, ISBN 82-92356- 00-2.

[46] Fossen, T.I., 1993, "High Performance Ship Autopilot with Wave Filter", Proceedings of the 10th Ship Control System Symposium (SCSS'93), Ottawa, Canada.

[47] Fossen, T.I., 2000, "A Survey on Nonlinear Ship Control: From Theory to Practice", Plenary Talk, Proceedings of the 5th IFAC Conference on Manoeuvring and Control of Marine Craft, Aalborg, Denmark.

[48] Fossen, T.I. and Strand, J.P., 1999a, "A Tutorial on Nonlinear Backstepping: Applications to Ship Control", Modelling, Identification and Control, 20(2), 83-135.

[49] Fossen, T.I. and Strand, J.P., 1999b, "Passive Nonlinear Observer Design for Ships Using Lyapunov Methods: Full-Scale Experiments with a Supply Vessel", Automatica, 35(1), 3-16.

[50] Fossen, T. I., 1999, “Recent Developments in Ship Control Systems Design”, World Superyacht Review, Sterling Publications Limited.

[51] Fossen, T. I., Breivik, M. and Skjetne, R., 2003, “Line-Of-Sight Path Following of Underactuated Marine Craft”, Proceedings of the Sixth IFAC Conference on Maneuvering and Control of Marine Crafts (MCMC 2003), Girona, Spain, 244- 249.

[52] Fossen, T.I., Grovlen, A., 1998, “Nonlinear Output Feedback Control of Dynamically Positioned Ships Using Vectorial Observer Backstepping”, IEEE Transactions on Control Systems Technology, 6(1), 121-128.

[53] Francisco, J., V., Elias, R., Eloy, L., Emiliano, M. and Haro Casado, M., 2008, “Simulations of an Autonomous In-scale Fast-ferry Model,” International Journal of Systems Applications, Engineering and Development, 2(3), 114-121.

[54] Freudenberg, J.S. and Looze, D.P., 1985, “Right Half Plane Poles and Zeros and Design Tradeoffs in Feedback Systems”, IEEE Transactions on Automatic Control, AC-30(6), 555-565.

[55] Friedland, B., 1986, Control System Design: An Introduction to State-Space Methods, McGraw-Hill.

[56] Fuller, C.R., Elliott, S.J. and Nelson, P.A., 1996, Active Control of Vibration. CA: Academic Press.

[57] Gevarter, W.B., 1970, “Basic Relations of Flexible Vehicles”, AIAA Journal, 8(4), 666-672.

[58] Godhavn, J.M., 1996, “Nonlinear Tracking of Underactuated Surface Vessels”, Proceedings of the 35th Conference Decision Control, Kobe, Japan.

[59] Godhavn, J.M., Fossen, T.I., Berge, S.P., 1998, “Nonlinear and Adaptive Backstepping Designs for Tracking Control of Ships”, International Journal on Adaptive Control and Signal Processing (Special Issue on Marine Systems), 12, 649–670.

[60] Gokasan, M., Bogosyan, O. S., Arabyan, A., and Sabanovic, A., 1998, “A Sliding Mode Based Controller for a Flexible Arm with a Load”, Proceedings of the IEEE Industrial Electronics Society Conference (IECON 98), Aachen, Germany, 2, 1083–1087.

[61] Ha, Q.P., Rye, D.C. and Durrant-Whyte, H.F., 1999, “Fuzzy Moving Sliding Mode Control with Application to Robotic Manipulators”, Automatica, 35, 607–616.

[62] Healey, A.J. and Lienard, D., 1993, “Multivariable Sliding-Mode Control for Autonomous Diving and Steering of Unmanned Underwater Vehicles”, IEEE Journal of Oceanic Engineering, 18(3), 327-339.

[63] Healey, A.J., Marco, D.B., 1992, “Slow Speed Flight Control of Autonomous Underwater Vehicles: Experimental Results with the NPS AUV II”, Proceedings of the 2nd International Offshore and Polar Engineering Conference (ISOPE), San Francisco, California, 523-532.

[64] Hung, J.Y., Gao, W., Hung, J.C., 1993, “Variable Structure Control: A Survey”, IEEE Transactions on Industrial Electronics, 40(1), 2-22.

[65] International Maritime Organization (IMO), 2007, Revised IMO Intact Stability Code, www.imo.org.

[66] Jiang, L. and Wu, Q. H., 2002, “Nonlinear Adaptive Control Via Sliding-Mode State and Perturbation Observer”, IEEE Proceedings Control Theory Applications, 149(4), 269-277.

[67] Jiang, Z. P., 2002, “Global Tracking Control of Underactuated Ships by Lyapunov’s Direct Method”, Automatica, 38, 301–309.

[68] Jiang, Z. P. and Nijmeijer, H., 1999, “A Recursive Technique for Tracking Control of Non-holonomic Systems in Chained Form”, IEEE Transactions on Automatic Control, 4(2), 265-279.

[69] Jie, J., Li, Y. and Zheng, L., 2007, “Self-Adjusting Fuzzy Logic Control for Vehicle Lateral Control," Fourth International Conference on Fuzzy Systems and Knowledge Discovery, 2, 614-618.

[70] Jwo, D. J. and Cho, T. S., 2007, “A Practical Note on Evaluating Kalman Filter Performance Optimality and Degradation”, Applied Mathematics and Computation, 193(2), 482-505.

[71] Kachroo, P. and Tomizuka, M., 1996, “Chattering Reduction and Error Convergence in the Sliding-Mode Control of a Class of Nonlinear Systems,” IEEE Transactions on Automatic Control, 41(7), 1063-1068.

[72] Kailath, T., 1980, Linear Systems, Prentice-Hall.

[73] Kallstrom, C. G., Astrom, K. J., Thorell, N. E., Eriksson, J. and Sten, L., 1979, “Adaptive Autopilots for Tankers”, Automatica, 15(3), 241-254.

[74] Kao, M. and Moskwa, J.J., 1995, “Nonlinear Diesel Engine Control and Cylinder Pressure Observation”, Journal of Dynamic Systems, Measurement and Control, 117, 183-192.

[75] Kawase, K., 2012, “Concise Derivation of Extensive Coordinate Conversion Formulae in the Gauss-Krueger Projection,” Geospatial Information Authority of Japan Bulletin, 60, 1-6.

[76] Kfoury, G.A. and Chalhoub, N.G., 2011, “Design of a Robust Nonlinear Observer for Constrained Systems”, Journal of Vibration and Control, 17(5), 651-666.

[77] Kfoury, G.A., Chalhoub, N.G., Henein, N.A. and Bryzik, W., 2006, “Enhancement of the Accuracy of the (P-W) Method Through the Implementation of a Nonlinear Robust Observer”, Journal of Sound and Vibration, 291(3–5), 1080–1103.

[78] Khaled, N. and Chalhoub, N.G., 2010, “Self Tuning Fuzzy Sliding Controller for the Ship Heading Problem”, Proceedings of the 2010 ASME Dynamic Systems and Control Conference (DSCC 2010), September 13-15, Cambridge, Massachusetts.

[79] Khaled, N. and Chalhoub, N.G., 2012, “A Robust Self-Tuning Fuzzy Sliding Mode Observer”, Proceedings of the ASME 2012 5th Dynamic Systems and Control Conference, and the 2012 11th Motion & Vibration

Conference (DSCC/MOVIC), October 17-19, Fort Lauderdale, Florida, 2, 591-596.

[80] Khaled, N. and Chalhoub, N.G., 2014, “A Self-Tuning Robust Observer for Marine Surface Vessels”, Submitted for possible publication in *Nonlinear Dynamics*.

[81] Khaled, N. and Chalhoub, N.G., 2009, “A Dynamic Model and a Robust Controller for a Fully Actuated Marine Surface Vessel”, Proceedings of the Vibro-Impact Dynamics of Ocean Systems, LNACM 44, 135-148.

[82] Khaled, N. and Chalhoub, N.G., 2011, “A Dynamic Model and a Robust Controller for a Fully Actuated Marine Surface Vessel”, Journal of Vibration and Control, 17(6), 801-812.

[83] Khaled, N., and Chalhoub, N.G., 2013, “A Self-Tuning Guidance and Control System for Marine Surface Vessels”, Nonlinear Dynamics, 73(1-2), 897–906.

[84] Khalil, H.K., 1996, Nonlinear Systems, Second Edition, Englewood Cliffs. NJ: Prentice Hall.

[85] Kim, M.H. and Inman, D.J., 2001, “Reduction of Observation Spillover in Vibration Suppression Using a Sliding Mode Observer”, Journal of Vibration and Control, 7(7), 1087-1105.

[86] Kim, M.H. and Inman, D.J., 2004, “Development of a Robust Non-Linear Observer for Dynamic Positioning of Ships”, Proceedings of the Institution

of Mechanical Engineers, Part I: Journal of Systems and Control Engineering, 218(1), 1-12.

[87] Kou, S.R., Elliott, D.L., Tarn, T.J., 1975, “Exponential Observers for Nonlinear Dynamic Systems”, Information and Control, 29, 204-216.

[88] Krener, A. J. and Isidori, A., 1983, “Linearization by Output Injection and Nonlinear Observers”, Systems and Control Letters, 3, 47-52.

[89] Laranjinha, M., Falzarano, J. M. and Guedes Soares, C., 2002, “Analysis of the Dynamical Behavior of an Offshore Supply Vessel with Water on Deck”, Proceedings of the 21st ASME International Conference on Offshore Mechanics and Arctic Engineering, June 23-28, Oslo, Norway, 383-390.

[90] Lauvdal, T., Fossen, T.I., 1998, “Rudder Roll Stabilization of Ships Subject to Input Rate Saturations Using a Gain Scheduled Control Law”, Proceedings of the IFAC Conference on Control Applications in Marine Systems (CAMS'98), October 27-30, Fukuoka, Japan, 121-127.

[91] Layne, J., Passino, K., 1993, “Fuzzy Model Reference Learning Control for Cargo Ship Steering”, IEEE Control Systems, 13(6), 23–34.

[92] Le, M.D., Tran, Q.T., Nguyen, T.N., Gap, V.D., 2004, “Control of Large Ship Motions in Harbor Maneuvers by Applying Sliding Mode Control”, 8th IEEE International Worshop, Avanced Motion Control, 695-700.

[93] Lefeber, A. A. J., Pettersen, K. Y. and Nijmeijer, H., 2003, “Tracking Control of an Underactuated Ship”, IEEE Transactions on Control Systems Technology, 11(1), 52-61.

[94] Lewis, F.L., 1986, Optimal Estimation with an Introduction to Stochastic Control Theory, Wiley-Interscience, New York.

[95] Li, D.Z. and Wang, W., 2011, “An Intelligent Sliding Mode Controller for Vibration Suppression in Flexible Structures”, Journal of Vibration and Control, 17(14), 2187-2198.

[96] Li, Z., Sun, J. and Oh, S., 2009, “Design, Analysis and Experimental Validation of a Robust Nonlinear Path Following Controller for Marine Surface Vessels”, Automatica, 45(7), 1649-1658.

[97] Lian, J. and Wang, M., 2010, “Sliding-Mode Control of Switched Delay Systems with Nonlinear Perturbations: Average Dwell Time Approach”, Nonlinear Dynamics, 62(4), 791-798.

[98] Lin, F., 2007, Robust Control Design: An Optimal Control Approach, John Wiley & Sons, Ltd.

[99] Lindegaard, K.P., 2003, “Acceleration Feedback in Dynamic Positioning”, PhD Thesis, Norwegian University of Science and Technology, Norway.

[100] Lopez, M.J. and Rubio, F.R., 1992, “LQG/LTR Control of Ship Steering Autopilots”, IEEE Proceedings on Intelligent Control, 447- 450.

[101] Loria, A., Fossen, T.I. and Panteley, E., 2000, "A Separation Principle for Dynamic Positioning of Ships: Theoretical and Experimental Results", IEEE Transactions on Control Systems and Technology, 8(2), 332-343.

[102] Luenberger, D.G., 1966, "Observers for Multivariable Systems", IEEE Transactions, Automatic Control, 11, 190–197.

[103] Luenberger, D.G., 1979, Introduction to Dynamic - Systems Theory, Models and Applications, John Wiley and Sons Limited, New York.

[104] Luenberger, D.G., 1964, "Observing the State of a Linear System", IEEE Transactions on Military Electronics, 8(2), 74-80.

[105] Maeda, M. and Murakami, S., 1992, "A Self-tuning Fuzzy Controller," Fuzzy Sets and Systems, 51(1), 29-40.

[106] Mamani, G., Becedas, J. and Feliu, V., 2012, "Sliding Mode Tracking Control of a Very Lightweight Single-Link Flexible Robot Robust to Payload Changes and Motor Friction", Journal of Vibration and Control, 18(8), 1141-1155.

[107] Mastory, C.G. and Chalhoub, N.G., 2014, "Nonlinear Robust Observer for Structures With Configuration-Dependent Natural Frequencies: Experimental and Theoretical Results", Submitted for possible publication in *Journal of Sound and Vibration*.

[108] Meirovitch, L., 1967, Analytical Methods in Vibrations, NY: Macmillan.

[109] Meirovitch, L., 1975, Elements of Vibrations Analysis, NY:McGraw-Hill.

[110] Minghui, W., Yongquan, Y., Yun, Z. and Fei, W., 2008, “Optimization of Fuzzy Control System Based on Extension Method for Ship Course-Changing/Keeping”, IEEE World Congress on Computational Intelligence, 434–438.

[111] Minorsky, N., 1922, “Directional Stability of Automatically Steered Bodies”, Journal of the American Society of Naval Engineers, 342, 280-309.

[112] Misawa, E.A. and Hedrick, J.K., 1989, Nonlinear Observers – A State-Of-The-Art Survey”, Journal of Dynamic Systems, Measurement, and Control, 111(3), 344–352.

[113] Moreira, L., Fossen, T.I. and Guedes Soares, C., 2007, “Path Following Control System for a Tanker Ship Model”, Ocean Engineering, OE-34, 2074–2085.

[114] Morel, Y., 2009, “Applied Nonlinear Control of Unmanned Vehicles with Uncertain Dynamics”, PhD Thesis, Virginia Polytechnic Institute and State University, USA.

[115] Nandam, P.K. and Sen, P.C., 1990, “A Comparative Study of a Luenberger Observer and Adaptive Observer-Based Variable Structure Speed Control System Using a Self-Controlled Synchronous Motor”, IEEE Transactions on Industrial Electronics, 37(2), 127-132.

[116] Ogata, K., 2002, Modern Control Engineering, Fourth Edition, Prentice-Hall.

[117] Park, J.H. and Asada, H., 1990a, “Design and Analysis of Flexible Arms for Minimum-Phase Endpoint Control”, Proceedings of the American Control Conference*,* May 23-25, San Diego, California 1, 1220-1225.

[118] Park, J.H. and Asada, H., 1990b, “Design and Control of Minimum-Phase Flexible Arms with Torque Transmission Mechanisms”, Proceedings of the IEEE International Conference on Robotics and Automation, May 13-18, Cincinnati, Ohio, 3, 1790-1795.

[119] Park, M.H. and Kim, K.S., 1991, “Chattering Reduction in the Position Control of Induction Motor Using the Sliding Mode,” IEEE Transactions on Power Electronics, 6(3), 317-325.

[120] Pettersen, K.Y., Lefeber, E., 2001, “Way-Point Tracking Control of Ships”, Proceedings of the 40th IEEE Conference on Decision and Control*,* 940–945.

[121] Pettersen, K.Y. and Fossen, T.I., 2000, “Underactuated Dynamic Positioning of a Ship – Experimental Results”, IEEE Transactions on Control systems technology, 8(5), 856-863.

[122] Pettersen, K.Y. and Nijmeijer, H., 2001, “Underactuated Ship Tracking Control: Theory and Experiments”, International Journal of Control, 74(14), 1435-1446.

[123] Pisano, A. and Usai, E., 2011, “Sliding Mode Control: A Survey with Applications in Math,” Mathematics and Computers in Simulation, 81(5), 954-979.

[124] Pivano, L., Johansen, T.A., Smogeli, O.N., Fossen, T.I., 2007, “Nonlinear Thrust Controller for Marine Propellers in Four-Quadrant Operations”, American Control Conference, New York.

[125] Polkinghorne, M. N., Roberts, G. N., Burns, R. S. and Winwood, D., 1995, “The Implementation of Fixed Rule-base Fuzzy Logic to the Control of Small Surface Ships”, Control Engineering Practice, 3(3), 321-328.

[126] Pota, H.R. and Vidyasagar, M., 1991, “Passivity of Flexible Beam Transfer Functions with Modified Outputs”, Proceedings of the 1991 IEEE International Conference on Robotics and Automation, April 9-11, Sacramento, California, 3, 2826-2831.

[127] Preumont, A., 2011, Vibration Control of Active Structures: An Introduction (Vol. 179), Springer.

[128] Procyk, T.J. and Mamdani, E.H., 1979, “A Linguistic Self-Organising Process Controller, Automatica, 15(1), 53–65.

[129] Qian, W.T. and Ma, C.C.H., 1992, “A New Controller Design for a Flexible One-Link Manipulator”, IEEE Transactions on Automatic Control 37(1), 132–137.

[130] Raghavan, S. and Hedrick, J.K., 1994, “Observer Design for a Class of Nonlinear Systems”, International Journal of Control, 59, 515–528.

[131] Rahman, Z.A., Mat Isa, A.A., Ali, H.H. and Anuar, M.A., 2013, “Control of Flexible Beam with Unmodelled Dynamics Using Second-Order Pole

Placement and LQR Techniques", Applied Mechanics and Materials, 393, 675-682.

[132] Rajamani, R. and Hedrick, J.K., 1993, "Adaptive Observer for Active Automotive Suspensions", Proceedings of the 1993 American Control Conference, June 2-4, San Francisco, California, 1, 706-710.

[133] Rundell, A.E., Drakunov, S.V. and DeCarlo, R.A., 1996, "A Sliding Mode Observer and Controller for Stabilization of Rotational Motion of a Vertical Shaft Magnetic Bearing", IEEE Transactions on Control Systems Technology, 4(5), 598–608.

[134] Sandler, M., Wahl, A., Zimmermann, R., Faul, M., Kabatek, U. and Gilles, E.D., 1996, "Autonomous Guidance of Ships on Waterways", Robotics and Autonomous Systems, 18(3), 327-335, ISSN 0921-8890.

[135] Shao, M.Q. and Chen, W.D., 2013, "Active Vibration Control in Cantilever-Like Structure: A Time Delay Compensation Approach", Journal of Vibration And Control, 19(5), 674-685.

[136] Slotine, J.J.E. and Li, W., 1991, Applied Nonlinear Control, Englewood Cliffs, NJ: Prentice Hall.

[137] Slotine, J.J.E., Hedrick, J.K. and Misawa, E.A., 1987, "On Sliding Observers for Nonlinear Systems", Journal of Dynamic Systems, Measurement and Control, 109(3), 245–252.

[138] Slotine, J.J.E. and Sastry, S.S., 1983, “Tracking Control of Non-Linear Systems Using Sliding Surfaces, with Application to Robot Manipulators”, International Journal of Control, 38, 465–492.

[139] Song, G. and Gu, H., 2007, “Active Vibration Suppression of a Smart Flexible Beam Using a Sliding Mode Based Controller”, Journal of Vibration and Control, 13(8), 1095-1107.

[140] Sorensen, A.J., Sagatun, S.I. and Fossen, T.I., 1996, “Design of a Dynamic Positioning System Using Model-based Control”, Control Engineering Practice, 4(3), 359-368, ISSN 0967-0661.

[141] Sorenson, H.W., 1985, Kalman Filtering: Theory and Application, IEEE Press, New York, N.Y.

[142] Spector, V.A. and Flashner, H., 1990, “Modeling and Design Implications of Noncollocated Control in Flexible Systems”, ASME Journal of Dynamic Systems, Measurement and Control, 112(2), 186-193.

[143] Strand, J.P., Ezal, K., Fossen, T.I., Kokotovic, P.V., 1998, “Nonlinear Control of Ships: A Locally Optimal Design”, Preprints of the IFAC NOLCOS'98, Enschede, The Netherlands, 732-738.

[144] Sugeno, M., 1985, Industrial Applications of Fuzzy Control, Elsevier Science Publishing Company.

[145] Sundarapandian, V., 2002, “Local Observer Design for Nonlinear Systems”, Mathematical and Computer Modeling, 35, 25-36.

[146] Sutton, R. and Jess, I., 1991, ”Real-time Application of a Self-organising Autopilot to Warship Yaw Control”, International Conference On Control, London, IEE, 332, 827-832.

[147] Sutton, R. and Towill, D.R., 1987, “A Fuzzy Model of The Helmsman Performing a Course-Keeping Task”, Applied Ergonomics, 18(2), 137-142.

[148] Thau, F.E., 1973, “Observing the State of Non-Linear Dynamic Systems”, International Journal of Control, 17(3), 471-479.

[149] Tönshoff, H.K. and Walter, A., 1994, “Self-tuning Fuzzy Controller for Process Control in Internal Grinding”, Fuzzy Sets and Systems, 63(3), 359-373.

[150] Torsetnes, G., Jouffroy, J. amd Fossen, T.I., 2004, “Nonlinear Dynamic Positioning of Ships with Gain-Scheduled Wave Filtering”, Proceedings of the 43rd IEEE Conference on Decision and Control, December 14-17, Atlantis, Paradise Island, Bahamas, 5, 5340-534.

[151] Tsinias, J., 1989, “Observer Design for Nonlinear Systems”, Systems and Control Letters, 13, 135–142.

[152] Utkin, V.I., 1981, “Principles of Identification Using Sliding Regimes”, Soviet Physics – Doklady, 26(3), 271–272.

[153] Vahedipour, A. and Bobis, J.P., 1992, “Smart Autopilots”, International Conference on Industrial Electronics, Control, Instrumentation and Automation, IECON 92, San Diego, USA.

[154] Vakil, M., Fotouhi, R. and Nikiforuk, P.N., 2011, "Trajectory Tracking for the End-Effector of a Class of Flexible Link Manipulators", Journal of Vibration and Control, 17(1), 55-68.

[155] Van Amerongen, J., and Udink Ten Cate, A.J., 1975, "Model Reference Adaptive Autopilots for Ships", Automatica, 11(5), 441-449.

[156] Van Amerongen, J., 1984, "Adaptive Steering of Ships - a Model Reference Approach", Automatica, 20(1), 3-14.

[157] Velagic, J., Vukic, Z. and Omerdic, E., 2003, "Adaptive Fuzzy Ship Autopilot for Track-keeping", Control Engineering Practice, 11(4), 433-443.

[158] Vukic, Z., Kuljaca, L. and Milinovic, D, 1996, "Predictive Gain Scheduling Autopilot for Ships", Proceedings of the 8th Mediterranean Electro-technical Conference, MELECON '96, 2, 1133-1136.

[159] Wagner, J. and Shoureshi, R., 1988, "Observer Designs for Diagnostics of Nonlinear Processes and Systems", ASME Winter Annual Meeting, November 27-December 2, Chicago, Illinois, 88-WA/DSC-5.

[160] Walcott, B.L. and Zak, S.H., 1986, "Observation of Dynamical Systems in the Presence of Bounded Nonlinearities/Uncertainties", Proceedings of the 25th IEEE Conference on Decision and Control, December 10-12, Athens, Greece, 2, 961–966.

[161] Wang, D. and Vidyasagar, M., 1989, "Transfer Functions for a Single Flexible Link", Proceedings of IEEE International Conference on Robotics and Automation, May 14-19, Scottsdale, Arizona, 1042-1047.

[162] Wang, C.C., Yau, H.T., 2011, “Nonlinear Dynamic Analysis and Sliding Mode Control for a Gyroscope System”, Nonlinear Dynamics, 66(1-2), 53-65.

[163] Williams, T., 1990, “Model Order Effects on the Transmission Zeros of Flexible Space Structures”, Proceedings of the American Control Conference, May 23-25, San Diego, California, 1, 876-877.

[164] Wolovich, W.A., 1987, Robotics: Basic Analysis and design, Holt, Rinehart and Winston, New York.

[165] Xia, X.H. and Gao, W.B., “On Exponential Observers for Nonlinear Systems”, Systems & Control Letters, 11, 319-325.

[166] Yanada, H. and Shimahara, M., 1997, “Sliding Mode Control of an Electrohydraulic Servo Motor Using a Gain Scheduling Type Observer and Controller”, Journal of Systems and Control Engineering, 211(1), 407-416.

[167] Yang, S.M., 1997, “Stability Analysis of Linear Structural Control Systems With Non Collocated Feedback”, Computers & Structures, 62(4), 685-690.

[168] Yang, S.M. and Lee, Y.J., 1994, “Modal Analysis of Stepped Beams With Piezoelectric Materials”, Journal of Sound and Vibration, 176(3), 289-300.

[169] Yang, S.M. and Mote, C.D. Jr., 1991, “Stability of Non-Conservative Linear Discrete Gyroscopic Systems”, Journal of Sound and Vibration, 147(3), 453-464.

[170] Yang, Y., Zhou, C. and Ren, J., 2003, “Model Reference Adaptive Robust Fuzzy Control for Ship Steering Autopilot with Uncertain Nonlinear Systems”, Applied Soft Computing, 3(4), 305-316, ISSN 1568-4946.

[171] Yang, Y., Jiang, B., 2004, “Robust Adaptive Fuzzy Control (RAFC) for Ship Steering with Uncertain Nonlinear Systems”, Proceedings of the 5th World Congress on Intelligent Control and Automation (WCICA 2004), 3, 2514- 2518.

[172] Yaz, E., 1993, “Stabilizing Compensator Design for Uncertain Nonlinear Systems”, Systems and Control Letters, 25, 11–17.

[173] Yeh, Z.M., 1994, “A Performance Approach to Fuzzy Control Design for Nonlinear Systems”, Fuzzy Sets and Systems, 64, 339-352.

[174] Young, D. and Felgar, R.P., 1949, Tables of characteristic functions representing normal modes of vibration of a beam, The University of Texas, Publication 4913.

[175] Young, K.D., Utkin, V.I. and Ozguner, U., 1999, “A Control Engineer’s Guide to Sliding Mode Control”, IEEE Transactions on Control Systems, 7(3), 328-342.

[176] Yu, F., 2009, “A Self-Tuning Fuzzy Logic Design for Perturbed Time-Delay Systems with Nonlinear Input”, Expert Systems with Applications, 36(3), 5304-5309.

[177] Zadeh, L.A., 1997, “Toward a Theory of Fuzzy Information Granulation and its Centrality in Human Reasoning and Fuzzy Logic”, Fuzzy Sets and Systems, 90(2), 111-127.

[178] Zhang, K., Scorletti, G., Ichchou, M.N. and Mieyeville, F., 2013, “Phase and Gain Control Policies for Robust Active Vibration Control of Flexible Structures”, Smart Materials and Structures, 22(7), 075025.

ABSTRACT

NON-LINEAR ROBUST OBSERVERS FOR SYSTEMS WITH NON-COLLOCATED SENSORS AND ACTUATORS

by

CONSTANTINE GEORGES MASTORY

August 2014

Advisor: Prof. Nabil Chalhoub

Major: Mechanical Engineering

Degree: Doctor of Philosophy

Challenges in controlling highly nonlinear systems are not limited to the development of sophisticated control algorithms that are tolerant to significant modeling imprecision and external disturbances. Additional challenges stem from the implementation of the control algorithm such as the availability of the state variables needed for the computation of the control signals, and the adverse effects induced by non-collocated sensors and actuators.

The present work investigates the adverse effects of non-collocated sensors and actuators on the phase characteristics of flexible structures and the ensuing implications on the performance of structural controllers. Two closed-loop systems are considered and their phase angle contours have been generated as functions of the normalized sensor location and the excitation

frequency. These contours were instrumental in the development of remedial actions for rendering structural controllers immune to the detrimental effects of non-collocated sensors and actuators.

Moreover, the current work has focused on providing experimental validation for the robust performances of a self-tuning observer and a sliding mode observer. The observers are designed based on the variable structure systems theory and the self-tuning fuzzy logic scheme. Their robustness and self-tuning characteristics allow one to use an imprecise model of the system and eliminate the need for the extensive tuning associated with a fixed rule-based expert fuzzy inference system. The first phase of the experimental work was conducted in a controlled environment on a flexible spherical robotic manipulator whose natural frequencies are configuration-dependent. Both observers have yielded accurate estimates of the required state variables in spite of significant modeling imprecision.

The observers were also tested under a completely uncontrolled environment, which involves a 16-ft boat operating in open-water under different sea states. Such an experimental work necessitates the development of a supervisory control algorithm to perform PTP tasks, prescribed throttle arm and steering tasks, surge speed and heading tracking tasks, or recovery maneuvers. This system has been implemented herein to perform prescribed throttle arm and steering control tasks based on estimated rather than measured state variables. These experiments served to validate the observers in a completely uncontrolled environment and proved their viability as reliable techniques for providing accurate estimates for the required state variables.

AUTOBIOGRAPHICAL STATEMENT

Constantine Mastory started his college journey in Mechanical Engineering at the University of Balamand, Lebanon in 2004. He completed his undergraduate degree in 2007 with an all terrain vehicle (ATV) design and build project. In 2009, he received a Master’s degree in the subject of composite materials. This same year he permanently moved to Detroit, MI and joined the PhD program at Wayne State University under the advisory of Prof. Nabil Chalhoub.

Over four years, he honed his control engineering skills through the immense exposure to both theoretical and experimental realms. As of March 2014, he received a position at Schaeffler Group as an Advanced Product Development Engineer, working on designing state of the art automotive systems.